Clinical Feasibility of Raman Spectroscopy for Quantitative Blood Glucose Measurement

by

Chae-Ryon Kong

B.S., Johns Hopkins University (2001)
M.S.E., Johns Hopkins University (2003)

Submitted to the Department of Electrical Engineering and Computer Science
in partial fulfillment of the requirements for the degree of

Doctor of Philosophy in Electrical Engineering and Computer Science

at the

MASSACHUSETTS INSTITUTE OF TECHNOLOGY

June 2011

Author .....
Department of Electrical Engineering and Computer Science
May 16, 2011

Certified by..... .....
Ramachandra R. Dasari
Associate Director, G. R. Harrison Spectroscopy Laboratory
Thesis Supervisor

Certified by.....
Rajeev J. Ram
Professor of Electrical Engineering
Associate Director, Research Laboratory of Electronics
Thesis Supervisor

Accepted by..... .
Leslie A. Kolodziejski
Professor of Electrical Engineering
Chair, Department Committee on Graduate Students

Clinical Feasibility of Raman Spectroscopy for Quantitative Blood Glucose Measurement

by

Chae-Ryon Kong

Submitted to the Department of Electrical Engineering and Computer Science
on May 16, 2011, in partial fulfillment of the
requirements for the degree of
Doctor of Philosophy in Electrical Engineering and Computer Science

Abstract

Diabetes mellitus is a leading cause of morbidity and mortality worldwide, and close monitoring of blood glucose levels is crucial for its diagnosis and management. Currently, blood glucose monitoring is done by blood withdrawal or through invasive access to the interstitial fluid. While Raman spectroscopy has been studied as a possible non-invasive optical technique for measuring blood glucose, it still faces several practical difficulties. These include tissue turbidity and autofluorescence, the lag between blood and interstitial fluid glucose concentrations, and the inherently weak intensity of aqueous glucose Raman signatures with respect to those of the interfering tissue.

This thesis investigates the feasibility of using Raman spectroscopy as a non-invasive technique for blood glucose monitoring, and studies different strategies to overcome the barriers to clinical application. In particular, the study proposes a dynamic concentration correction scheme to correct for the calibration errors arising from the lag between glucose concentrations in the bloodstream and the interstitial fluid. In addition, Monte Carlo simulations were employed to study the differences in the distribution of Raman scattered photons along the depth of the tissue between back-scattered and transmission mode Raman spectroscopy. Finally, a portable clinical Raman spectroscopy unit was developed utilizing a non-imaging optical element called a compound hyperbolic concentrator (CHC). The CHC coupled with a matching focusing lens efficiently collects and collimates Raman light from highly scattering tissues, while maintaining much smaller physical dimensions than a compound parabolic concentrator.

Using the clinical instrument, skin Raman spectra were collected from healthy human subjects undergoing oral glucose tolerance tests, while the corresponding reference blood glucose concentrations were measured simultaneously with a conventional finger-stick glucose meter. From these datasets, linear and non-linear multivariate calibration techniques were used to relate the Raman spectral intensities to the glucose

concentrations. The calibrated algorithms were then tested to demonstrate clinical accuracy as required by the Food and Drug Administration and the International Organization for Standardization. Despite the remaining challenges, the promising results obtained in this study provide important insights required in the clinical translation of Raman spectroscopy for non-invasive blood glucose monitoring.

Thesis Supervisor: Ramachandra R. Dasari
Title: Associate Director, G. R. Harrison Spectroscopy Laboratory

Thesis Supervisor: Rajeev J. Ram
Title: Professor of Electrical Engineering
Associate Director, Research Laboratory of Electronics

Acknowledgments

My research at the Spectroscopy Laboratory would not have been possible without the help from many people. First of all, I would like to thank the late Professor Michael Feld, whose vision and pioneering spirit opened up many different possibilities in the field of biomedical optics and spectroscopy. Even until his last few months, he expressed his enthusiasm for this work and challenged us with the most relevant and difficult questions. I am indebted to the Spectroscopy Laboratory associate director and thesis supervisor Dr. Ramachandra Dasari, who has provided invaluable guidance in research, logistics and many other aspects with great patience and care since my first day at the Spectroscopy Laboratory. I am also grateful to Professor Rajeev Ram for agreeing to co-supervise my thesis when I was an orphaned graduate student who has just lost his thesis supervisor. I would also like to thank Professor Erich Ippen and Professor Cardinal Warde for serving on my thesis commitee and providing helpful advice and encouragement.

I thank Dr. Ravi Thadhani, Catherine Ricciardi, Ilene Horvitz and Helene Cyr who generously provided access to the MIT General Clinical Research Center facilities and assistance with human subject experiments. I would also like to thank the current and former members of the Spectroscopy Laboratory for their help during various stages of my research and other responsibilities in the laboratory, ranging from designing an intravascular spectroscopic probe for atherosclerosis detection, investigating the use of Brillouin scattering for biological tissues, developing clinical instruments for donation to clinical investigators, and finally the clinical feasibility study for Raman glucose detection: Obrad Šćepanović, Zoya Volynskaya, Gajendra Singh, Ishan Barman, Luis Galindo, Chung-chieh Yu, Wonshik Choi, Yongjin Sung, Zahid Yaqoob, Niyom Lue, Narahara Chari Dingari, and Jeon-woong Kang. In particular, Luis Galindo played a very important role in the clinical instrument development and Ishan Barman has provided tremendous help in developing and understanding the scientific concepts. Jeon-woong Kang, Narahara Chari Dingari and Yongjin Sung helped with the human subject studies by either recruiting volunteers or participating

in the study as a subject. I would also like to thank Mark Belanger who patiently taught me how to operate the CNC machines at the Edgerton Student Machine Shop and Stephen Fulghum for his assistance and advice on Zemax simulations.

I thank Professor Terry Orlando for helping me deal with difficult times by being a great Graduate Officer at the EECS department as well as a Housemaster at Ashdown House, and Dr. Simon Lejeune for helping me cope with many series of adversities during my life in graduate school.

Finally, I would like to thank my parents, my brother and friends for their love, prayers and support.

This research was supported by National Institutes of Health Laser Biomedical Research Center grant P41-RR02594. Part of the study was also supported by the MIT EECS department teaching assistantship and research assistantship support, as well as the Mogam Science Scholarship Foundation. The clinical study was conducted at the Clinical Research Center (CRC) at the Massachusetts Institute of Technology, supported by Harvard Clinical and Translational Science Center (UL1 RR025758), from the National Center for Research Resources. The content is solely the responsibility of the author and does not necessarily represent the official views of the National Center for Research Resources or the National Institutes of Health.

All clinical study protocols involving human subjects were conducted after receiving approval by the MIT Committee On the Use of Humans and Experimental Subjects (COUHES).

Contents

List of Figures

THIS PAGE INTENTIONALLY LEFT BLANK

List of Tables

THIS PAGE INTENTIONALLY LEFT BLANK

Chapter 1

Introduction

Diabetes mellitus is a debilitating disease characterized by the impaired blood glucose regulation, and it continues to affect increasing number of people worldwide. A close monitoring of blood glucose level is essential for effective diagnosis and management of the disease, but currently this is achieved by frequent blood withdrawal and other invasive methods. This is not only inconvenient for most diabetics, but also presents tremendous difficulties to individuals with needle phobia and Type I diabetic children. Clearly, a non-invasive glucose monitoring technique would significantly improve the patients' quality of life, as well as compliance to glucose monitoring.

Raman spectroscopy has been studied as a promising candidate for non-invasive optical blood glucose measuring technique. During a Raman event, the inelastic scattering causes the incident photon to lose energy by the amount specific to the particular vibrational and rotational modes of the interacting molecule. As such, the resulting Raman spectrum provide exceptional chemical specificity. In addition, since the intensity of Raman spectrum is proportional to the concentration of the interacting molecule, analyzing the aggregate Raman spectrum by multivariate calibration techniques allows for an accurate quantification of the individual chemical components. Many laboratory based, proof-of-principle experiments have been performed to demonstrate the potential of Raman spectroscopy to accurately measure blood glucose concentrations in a non-invasive manner.

However, transdermal glucose measurement by Raman spectroscopy is yet to be

seen in the daily clinical setting due to many remaining practical challenges. For example, the non-invasive nature of transdermal Raman spectra collection precludes direct measurement of blood glucose and this limits the optical tissue sampling volume to the interstitial fluid (ISF) space. While the blood glucose concentration is the clinically relevant parameter, the ISF glucose level as measured by non-invasive Raman spectroscopy is an indirect indicator for blood glucose. This leads to complications in calibration steps during rapid changes in glucose levels, such as after a meal or insulin administration, due to the time lag between the blood and interstitial fluid glucose concentrations during these non-equilibrium states. In addition, spontaneous Raman scattering is an inherently weak phenomenon, and collection of Raman spectra from humans in a clinical setting requires specially designed high-throughput spectroscopic instruments that are also compact enough to be portable. Previous human subject studies for glucose detection have mainly been conducted using a stationary laboratory-based Raman spectroscopy setup.

This thesis aims to demonstrate the clinical feasibility of accurate and non-invasive glucose concentration measurements by Raman spectroscopy on a population of human subjects. For this purpose, a high throughput and portable clinical Raman spectroscopy system is designed and constructed. In addition, potential solutions are provided for the aforementioned challenges.

1.1 Objectives

1.1.1 Address the issue of lag between blood and ISF glucose concentrations

The effect of the lag between blood and ISF glucose concentrations on the spectroscopic calibration and prediction performance had to be characterized. Based on the insight provided by this analysis, a potential solution to the problem needed to be presented.

1.1.2 Design and construct a high-throughput and portable clinical Raman spectroscopy system

This objective required satisfying two seemingly conflicting goals of achieving high throughput while maintaining compactness for practical clinical application. Previous laboratory-based Raman spectroscopy setups had to be studied in order to identify the targets of optimization, while new non-imaging optical elements were to be investigated for their potential to enhance light collection efficiency. In addition, the implications of collecting tissue Raman spectra in the transmission mode had to be investigated.

1.1.3 Demonstrate clinical feasibility through human subject studies

The completed clinical instrument was to be used for collecting Raman spectra from human subjects in a clinical setting. The collected Raman spectroscopy and blood glucose data were to be analyzed to determine the glucose measurement performance and clinical feasibility.

1.2 Major accomplishments

- The problem of the time lag between blood and ISF glucose concentrations was investigated and a viable solution has been developed. The new calibration scheme was termed "dynamic concentration correction" (DCC) which showed significant improvement in spectroscopic calibration and glucose prediction performance during rapid changes in glucose levels.

- A high throughput and portable clinical Raman spectroscopy instrument has been designed and constructed using a compound hyperbolic concentrator (CHC). The distribution of Raman scattering events along the depth of the skin tissue was simulated by Monte Carlo methods for both back-scattered mode and

transmission mode. The simulation studies revealed potential advantages of transmission geometry over back-scattered mode.

- The clinical instrument was used successfully for collecting Raman spectra from human subjects undergoing OGTT. Different calibration and prediction schemes were used on the same data to compare their relative performance. The analysis of the clinical data indicated that when used for the measurement of glucose concentrations on the same skin tissue site under identical measurement conditions, the performance of the Raman spectroscopy instrument was good enough to meet the requirements of the U.S. Food and Drug Administration as well as the International Organization for Standardization. However, the study also revealed potential difficulties arising from the change in measurement site and conditions.

1.3 Thesis outline

1.3.1 Chapter 2 Background and significance

This chapter describes the prevalence and types of diabetes and motivates the need for a non-invasive glucose monitoring technique. It also reviews other minimally invasive and non-invasive glucose monitoring techniques, and introduces NIR Raman spectroscopy as a promising candidate while emphasizing its advantages over other techniques.

1.3.2 Chapter 3 Correcting for the lag between blood and interstitial fluid glucose

This chapter describes the presence of the lag between blood and interstitial fluid glucose concentrations during rapid changes in glucose levels, and how it affects spectroscopic calibration and prediction accuracy, as well as the uncertainty in the predicted glucose concentration. Then DCC was derived and presented as a potential

solution to this problem, and a new expression was derived to describe the prediction uncertainty under DCC implementation.

1.3.3 Chapter 4 Monte Carlo study of transmission mode Raman spectroscopy

In this chapter, a numerical simulation study was designed and performed to gain a better understanding of the differences between Raman spectra collected in back-scattered mode and transmission mode geometries. Particular emphasis was placed on observing the distribution of the Raman scattering events along the depth of the tissue, under the two different collection geometries.

1.3.4 Chapter 5 Development of clinical Raman spectroscopy instrument

This chapter elaborates the design and construction of a portable clinical Raman spectroscopy instrument. In particular, the purpose and the design of the non-imaging optical element, CHC, was described in detail. The clinical instrument shown in this chapter was used in the human subject studies described in Chapter 6.

1.3.5 Chapter 6 Human clinical study

This chapter describes the human subject study conducted at the MIT Clinical Research Center (MIT CRC) using the clinical instrument shown in Chapter 5. The Raman spectra and blood glucose concentration values were used to create calibration models by partial least squares (PLS) regression and support vector regression (SVR). Also, the effect of implementing DCC and removing tissue autofluorescence in the Raman spectra by low order polynomial fitting was observed when performing glucose calibration and prediction analyses.

1.3.6 Chapter 7 Conclusion and future directions

In this chapter, the objectives and major accomplishments were reviewed. Potential future directions are suggested based on the new insights obtained from this study.

Chapter 2

Background and significance

2.1 Diabetes mellitus

Diabetes mellitus represents a leading cause of morbidity and mortality worldwide, affecting nearly 285 million people in 2010, and expected to affect 438 million by 2030 [1]. In 2010 alone, 4 million people died from diabetes worldwide [1]. Diabetes is characterized by an impairment of blood glucose regulation. In Type I diabetes, a pathology in the pancreas causes insufficient production of insulin, which is normally secreted in response to high blood glucose levels in order to promote glucose uptake by the tissues. These patients typically require external administration of insulin for proper blood glucose management. Type II diabetes is caused by the body's reduced sensitivity to insulin, usually arising as a complication of obesity [2]. Finally, gestational diabetes can occur in pregnant women who were not diabetic prior to the pregnancy. While gestational diabetes normally resolves with the end of pregnancy, in some cases it may have adverse effects on the fetus such as macrosomia, in which the baby becomes overweight due to abnormally high blood glucose levels. Prolonged exposure to high levels of blood glucose accompanies many morbid complications such as blindness and a variety of neurovascular diseases. Therefore, it is essential to frequently monitor the blood glucose levels for successful management of the disease. Currently, blood glucose monitoring is achieved by frequent withdrawal of blood or other invasive means. Due to the inconvenience and invasiveness of these

methods, many diabetics fail to comply with glucose monitoring. In particular, at least 10% of the U.S. population is affected by needle phobia that can trigger fainting episodes with needle piercing [3], and needle-phobic individuals who are also diabetic have extreme difficulty in managing their conditions [4]. Therefore, a non-invasive method of measuring blood glucose level would greatly benefit the increasing number of diabetics worldwide.

2.2 Non-invasive and minimally-invasive glucose monitoring techniques

Most electrochemical glucose sensors currently used in the clinic employs the glucose oxidase enzymatic reaction:

$$\beta\text{-D-glucose}+O_2 \rightarrow \text{D-glucono-1,5-lactone} + H_2O_2$$

where gluconic acid and hydrogen peroxide (H_2O_2) are generated. The hydrogen peroxide can then be detected with a platinum electrode. These sensors have been adapted in the form of a needle, which can be implanted subcutaneously for continuous glucose monitoring (e.g., Minimed by Medtronic Inc. and FreeStyle Navigator by Abbott Laboratories). However, these minimally invasive sensors need to be replaced about once a week due to build up of biomaterial residues on the sensor surface, which interferes with glucose measurement. Another commercial continuous glucose monitoring device, the GlucoWatch by Animas, used reverse iontophoresis to extract interstitial fluid from the skin tissue and measured glucose with electrochemical sensors [5]. However, this sensor faced practical problems of frequent disruption in glucose sensing by sweating, and is no longer in production.

Many researchers have looked into optical techniques for non-invasive glucose detection [6]. For example, Esenaliev et al. proposed the use of optical coherence tomography for glucose detection, by observing the variation of tissue optical scattering parameter (μ_s) induced by changes in the glucose concentration [7]. The optical scattering coefficient μ_s and the reduced scattering coefficient μ_s' depend on the mis-

match of the refractive index of the interstitial fluid (1.348 to 1.352 in near infrared [8]) and the cell membranes (1.350 to 1.460 in near infrared [9]). Change in the blood glucose concentration would alter the interstitial fluid glucose concentration, which would subsequently affect the refractive index and the optical scattering parameters. This effect was demonstrated in tissue phantoms [10] as well as *in vivo* using reflectance measurement systems [11].

King et al. suggested that glucose concentration can be measured by observing the changes in light polarization in the aqueous humor of the eye [12]. When a linearly polarized light interacts with a solution containing molecules that have a distinct chirality due to its asymmetric molecular structure, the plane of the linearly polarized light undergoes rotation about the axis of propagation. Since glucose molecules are chiral (the naturally occurring D-glucose being dextrarotatory), the amount of rotation of the linearly polarized light depends on the concentration of glucose present in the tissue. However, this effect is difficult to observe in typical turbid tissues, since the scattering effects dominate over polarization effects. Therefore, King et al. suggested the observation of light polarization change by shining a linearly polarized light to the anterior chamber of aqueous humor of the eye, which is a transparent tissue with little turbidity.

Others have studied changes in the photoacoustic effect induced by different glucose concentrations [13, 14]. The photoacoustic effect measures the optically generated acoustic signal, where a laser pulse fired onto the tissue sample gets absorbed and heats up the illuminated region, which thermally expands to generate an acoustic pressure wave that can be detected with a piezoelectric sensor. Since the viscosity of aqueous glucose solution increases with glucose concentration, the photoacoustic signal would also change due to the changes in tissue glucose concentrations. Measuring and analyzing the changes in the photoacoustic signal from the tissue could lead to the detection of changes in glucose concentrations. An *in vivo* study involving 62 human subjects using a potentially commercializable Aprise^{TM} sensor (Glucon Inc., Boulder, CO) showed promising results [14]. In addition, Wadamori et al. showed that the measurable tissue depth can be controlled by changing the modulation frequency [15],

which can be useful for detecting glucose from tissues with layered structures such as the skin.

Evans et al. [16] investigated the glucose-induced changes in tissue autofluorescence mediated by variations of reduced nicotinamide adenine dinucleotide (NADH) or its phosphorylated derivative, NAD(P)H from glucose metabolism. The production of these coenzymes by the skin fibroblasts and adipocytes is mediated by their glucose metabolism, and their measured autofluorescence intensity and lifetime have been found to be indirect markers for the extracellular glucose concentration [16].

All of these techniques attempt to find glucose sensitivity by observing the glucose-induced optical changes that can be detected non-invasively. However, these techniques often face significant challenges from the fact that the glucose-induced optical changes are not glucose-specific, and can be influenced by other physiological and anatomical variations.

In contrast, vibrational spectroscopy techniques look for glucose-specific molecular vibrational markers in the observed spectrum. For example, infrared absorption spectroscopy is widely used in chemistry to study the vibrational modes of the molecular bonds, such as "stretching", "twisting", and "scissoring" modes. Since different molecules are uniquely identified by their molecular structures, vibrational spectroscopy techniques such as infrared absorption spectroscopy and Raman spectroscopy provide a molecularly specific marker for the target analyte. Infrared absorption spectroscopy was employed in the mid-infrared (MIR) region (2.5 to 25 μm) by Heise et al. to detect glucose from the oral cavity [17], but faced difficulty due to limited tissue penetration depth of MIR light and person-to-person variations in MIR absorption spectra. As near infrared (NIR) light (800 nm to 2.5 μm) offers greater tissue penetration depth and generates relatively low amount of tissue autofluorescence, many researchers have used NIR absorption spectroscopy to investigate non-invasive glucose detection from human subjects. Burmeister et al. and Marbach et al. employed NIR absorption spectroscopy to detect glucose from the oral cavity [18, 19], while other groups targeted the forearm [20, 21] and fingertip [22, 23]. While NIR absorption spectroscopy provides molecularly specific information with high op-

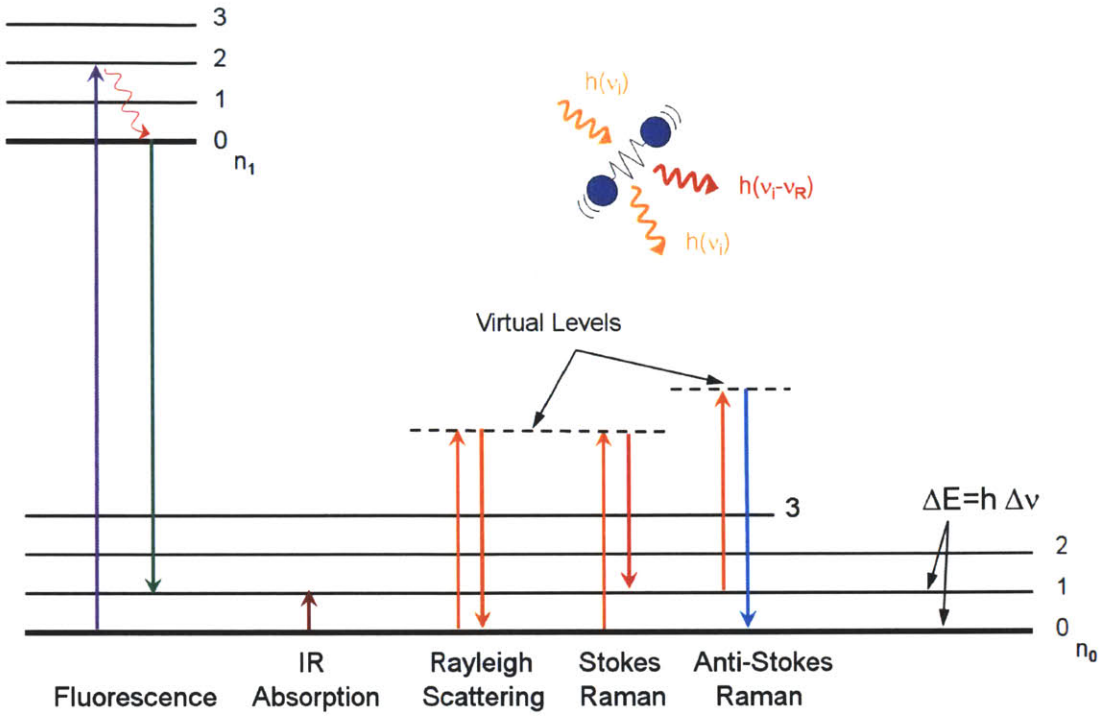

Figure 2-1: Jablonski diagram describing the transition of electronic states for various spectroscopic modalities.

tical intensities, its broad spectral features often limit its specificity. This was the main reason behind the failure of Diasensor by Bico, which was a NIR absorption spectroscopy based glucose monitoring device that was briefly introduced commercially in Europe, only to be abandoned eventually. On the other hand, NIR Raman spectroscopy provides similar molecular vibrational and rotational information while also offering much sharper spectral features and superior molecular specificity than NIR absorption spectroscopy.

2.3 NIR Raman spectroscopy for transdermal glucose detection

Raman spectroscopy can be performed with light at any wavelength, and its spectral intensity increases with the light frequency to the fourth power. Also, ultraviolet

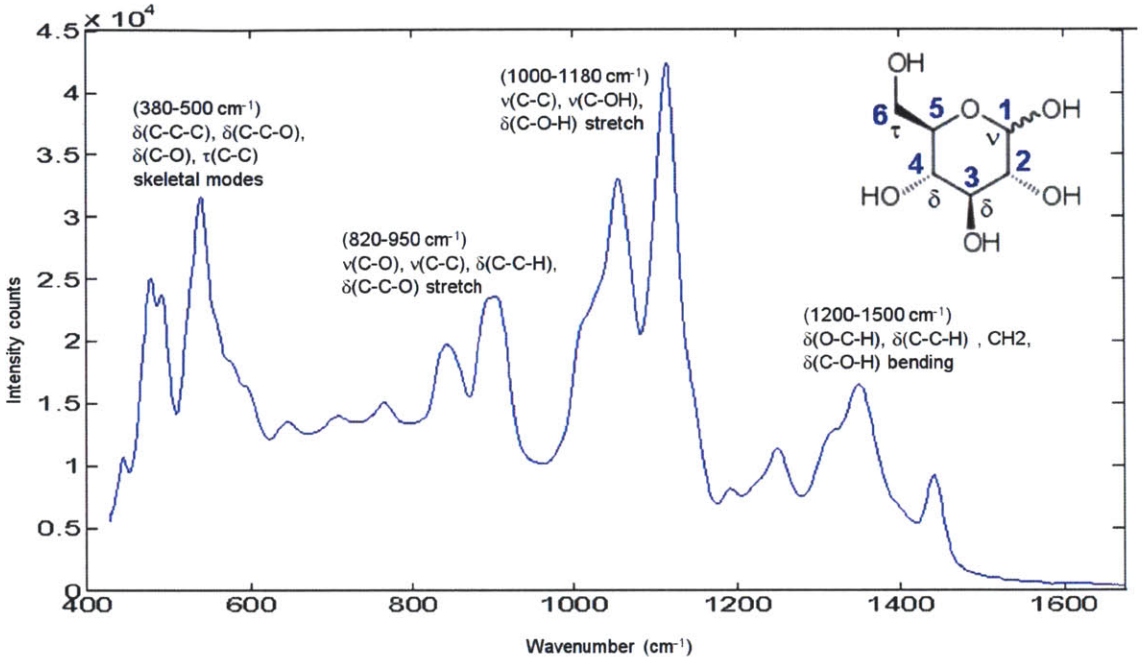

Figure 2-2: Raman spectrum of aqueous D-glucose with the molecular vibrational and rotational modes labeled based on [24].

resonance Raman spectroscopy can provide very high spectral intensities. However, the NIR spontaneous Stokes Raman spectroscopy is often preferred for biological tissue analysis, for similar reasons as in the case of NIR absorption spectroscopy:

- Deeper tissue penetration depth.
- Relatively weaker tissue autofluorescence.
- Less photodamage to the tissue.

Unlike NIR absorption spectroscopy, NIR Raman spectroscopy does not suffer from the adverse effect of NIR light absorption by water. While the large absorption of NIR light can attenuate tissue NIR absorption spectral features, NIR Raman features of water are not strong components of the tissue Raman spectrum. The molecular vibrational and rotational modes of aqueous D-glucose Raman spectrum is shown in Fig. 2-2. Despite its excellent chemical specificity, the disadvantage of NIR Raman spectroscopy is that its optical signal is very weak, as typically less than one out of

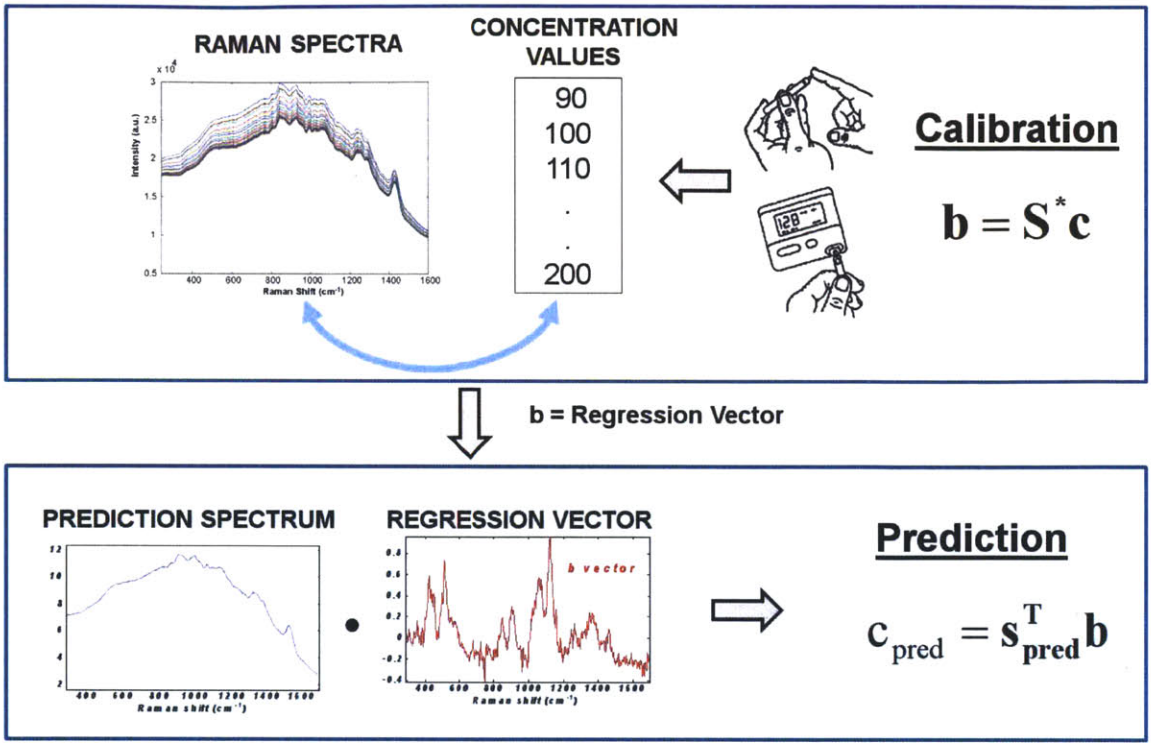

Figure 2-3: Spectral calibration and prediction by partial least squares regression.

a million photons undergo a spontaneous Raman scattering event. To make matters worse for transdermal glucose detection, the Raman cross section of aqueous glucose is very small (5.6×10^{-30} cm^2 molecule^{-1} sr^{-1}, at 514.5 nm [25]). For this reason, recent studies have suggested the use of surface enhanced Raman spectroscopy to amplify the glucose sensitivity [26]. Since surface enhanced Raman spectroscopy alone would amplify all chemical species near the gold or silver substrate, this study increased the glucose sensitivity by functionalizing the silver substrate surface with a layer of molecules of high affinity to glucose molecules (specifically, 1-decanethiol [$HS(CH_2)_9CH_3$] [26]). Since the Raman surface enhancement effect needs close proximity to the silver or gold substrate surface, the increased glucose affinity of the functionalized substrate would allow for a selective enhancement of glucose detection [26].

Early attempts to detect blood glucose concentration by Raman spectroscopy involved a direct analysis of whole blood samples [27, 28]. These studies used partial

least squares (PLS) regression to analyze the blood constituents. Figure 2-3 shows a schematic diagram describing the PLS calibration and prediction procedures. The Raman spectral intensities were related to the corresponding reference blood glucose values by a regression vector called the "**b**" vector during the calibration procedure. Once calibrated, the **b** can be used on a prospective Raman spectrum to extract its corresponding blood glucose concentration. More advanced and sophisticated calibration techniques were developed later on, in order to improve the robustness and glucose specificity of the calibration [29, 30]. These include the Hybrid Linear Analysis (HLA) [29] and Constrained Regularization (CR) [30]. Ideally, if the concentrations for all constituents of the tissue Raman spectra are known, an explicit calibration method such as ordinary least squares can be used to construct a comprehensive and accurate calibration algorithm. However, these explicit calibration methods break down when the tissue constituents are misrepresented due to lack of accurate information about the tissue constituents. On the other hand, implicit calibration methods such as PLS only require the concentration of the analyte of interest, and therefore tend to be more robust. Since the Raman spectrum of a pure glucose solution can be measured separately, HLA attempts to extract the advantages of both explicit and implicit calibration algorithm, by incorporating the information about the glucose Raman spectrum into the implicit calibration [29]. This can be done by subtracting the glucose Raman spectrum (appropriately scaled according to the known glucose concentration of the calibration samples) from the tissue Raman spectra to remove the glucose contribution to the overall tissue Raman spectra:

$$\mathbf{S}_b = \mathbf{S} - k\mathbf{a} \tag{2.1}$$

where **S** is the matrix of Raman spectra obtained from the calibration samples, **a** is the Raman spectrum of unit concentration of glucose, and **k** is the concentration of glucose present in the calibration samples [29]. Then the principal components of $\mathbf{S}_b$ are used to generate a matrix of orthogonal basis spectra **V**. The residual portion of

$\mathbf{a}$ that is orthogonal to $\mathbf{V}$ is calculated as:

$$\mathbf{r} = \mathbf{a} - \mathbf{a}\mathbf{V}^T\mathbf{V} \tag{2.2}$$

which can be used to obtain the HLA regression vector

$$\mathbf{b} = \mathbf{r}/(\mathbf{a} \cdot \mathbf{r}). \tag{2.3}$$

Similarly to HLA, CR performs implicit calibration with explicit constraint specified by the known glucose Raman spectrum, but it attempts to improve robustness by employing Tikhonov regularization [31]. Both HLA and CR showed encouraging results with numerically simulated Raman spectra and tissue phantoms [29, 30].

Eventually, Enejder et al. successfully demonstrated *in vivo* glucose detection by collecting Raman spectra from the forearms of human subjects undergoing an oral glucose tolerance test (OGTT), while Chaiken et al. used tissue modulation on human finger tip to collect the blood Raman spectrum *in vivo*, which was subsequently used to estimate glucose concentration [32]. Here, "tissue modulation" refers to the measurement of two separate Raman spectra from the same tissue site, with and without the application of external physical pressure. Applying physical pressure to the tissue squeezes out the blood and interstitial fluid from the tissue site, while removing such pressure restores blood and interstitial fluid perfusion. By measuring the Raman spectra under these two conditions and subtracting one spectrum from the other, the residual Raman spectrum can (in principle) represent the net signal arising from the blood and interstitial fluid alone [32]. Since glucose is present in the blood and interstitial fluid, this tissue modulation method would, if successful, remove the Raman spectral contributions from the interfering tissue constituents and improve the glucose specificity.

More recently, Shih et al. and Barman et al. proposed to use the diffuse reflectance spectrum to remove the undesirable turbidity-induced Raman spectral intensity variations [33, 34, 35]. In addition, it has been suggested that calibration errors introduced by spurious correlations between tissue autofluorescence photobleaching

and the glucose concentration can be reduced by applying autofluorescence removal techniques [36, 37, 38]. Finally, it has been shown that a non-linear regression technique called support vector regression (SVR) could significantly improve the spectral calibration and glucose prediction performance over conventional linear partial least squares (PLS) technique [39].

However, these promising recent developments still do not cover all remaining issues that need to be resolved before transdermal glucose monitoring by Raman spectroscopy can become a routine clinical practice. The following chapter describes the problem of the lag between blood and interstitial fluid glucose concentrations and presents a potential solution. The later chapters will describe the study of transmission mode Raman spectroscopy, efforts for clinical instrument development, and the human subject studies conducted to verify the clinical feasibility of transdermal glucose monitoring by Raman spectroscopy. Finally, the last chapter will discuss the remaining challenges and suggests potential future directions based on the new insights obtained from this study.

Chapter 3

Correcting for the lag between blood and interstitial fluid glucose

3.1 Introduction

From the thick aorta down to the few micron-thick capillary vessels, the blood circulatory system permeates most parts of the human body. By the constant pumping action of the heart, the blood never ceases to transport nutrients and waste products to and from the living tissues to maintain homeostasis. For this reason, the glucose metabolism of the entire body can be monitored in the clinic by analyzing the blood samples withdrawn from the finger tip. However, blood is contained within the circulatory system, and the exchange of nutrients with the surrounding tissues occurs through the capillary wall by hydrostatic and osmotic pressures, as well as by passive diffusion. This happens in the fluid that fills the space between the capillaries and the surrounding cells, which is called the interstitial fluid (ISF). The exchange of glucose molecules between the blood vessels and the ISF continue until the glucose concentrations in the two compartments reach equilibrium. This equilibrating process takes time (typically on the order of 20 minutes in healthy humans), and the time lag leads to temporary differences between the glucose concentrations in the blood and the ISF, especially during rapid changes in glucose levels such as immediately after a meal ingestion or insulin administration. This leads to challenges in non-invasive

and minimally invasive glucose detection techniques, which typically monitor glucose levels from the ISF. For the case of NIR Raman spectroscopy, the NIR light penetrates the skin about 1 mm. At this depth, the blood capillaries are not very dense, contributing only about 5% of the skin volume, while the ISF constitutes nearly 45% [40, 41]. Therefore, the optical sampling volume mostly comprises of the ISF glucose. Similarly, minimally invasive electrochemical sensors such as Medtronic Minimed Guardian and FreeStyle Navigator from Abbott Diabetes Care are implanted under the skin to monitor the ISF glucose. In both cases, complications arise from the fact that reference glucose measurements for calibration are made from blood glucose. As pointed out by Cengiz and Tamborlane [42], the physiological lag introduces systematic errors during calibration which adversely impact long-term sensor performance, even in the presence of a positive correlation between blood and ISF glucose [43, 44, 45]. Such diagnostic errors may lead to unnecessary insulin administration, which could lead to a dangerous degree of hypoglycemia. While this calibration error could be avoided by performing all measurements under equilibrium conditions, obtaining multiple calibration measurements at different glucose levels would require employing sophisticated and riskier glucose clamp techniques, where the glucose is artificially infused into the bloodstream and the infusion rate is carefully controlled to maintain a steady plasma glucose level [46]. Moreover, even if calibration was done accurately, the lack of knowledge of glucose kinetics in prediction samples would introduce an uncertainty in the concentration estimates.

In order to account for the differences in blood and ISF glucose, Freeland and co-workers developed a model where the ISF and blood glucose were considered to reside in two compartments [47, 48]. By relating the glucose concentrations in the two compartments with a simple mass transfer model across a semipermeable membrane, accurate estimates of blood glucose concentration could be extracted from subcutaneous ISF electrochemical sensor measurements. This chapter introduces a new spectroscopic calibration scheme using dynamic concentration correction (DCC), which is based on a on a similar two-compartment mass transfer model [49][†]. While

[†]The first two authors contributed equally to this cited article, as stated explicitly in its "Ac-

Freeland and co-workers developed the two-compartment mass transfer model to explain the glucose lag observed in implantable electrochemical glucose sensors, currently no analogous models exist for spectroscopic calibration algorithms, which are inherently more complex due to the multivariate nature of the data. By using DCC, blood and ISF glucose concentrations are interconverted at the appropriate stages of spectroscopic calibration and prediction to form an accurate and consistent regression model. The resulting regression model can then be used on a new set of acquired spectral samples to accurately predict the blood glucose concentrations. In addition, an analytical expression is derived to describe the limiting uncertainty arising from the presence of the lag between blood and ISF glucose concentrations.

3.2 Dynamic concentration correction

Conventional spectroscopic calibration methods use linear regression to map the spectral intensities to the glucose concentrations [50], which is represented as a flowchart in Fig. 3-1. During the calibration step, the regression vector $\mathbf{b}$ is obtained by

$$\mathbf{b} = \mathbf{S}_{calib}^{+}\mathbf{c}_{blood} \tag{3.1}$$

where $\mathbf{S}_{calib}$ is the matrix of calibration spectra, $\mathbf{S}_{calib}^{+}$ is the appropriate pseudo-inverse of $\mathbf{S}_{calib}$ as evaluated by the calibration method of choice, and $\mathbf{c}_{blood}$ is the vector of measured reference concentrations of the blood glucose in the calibration samples. Since the optical spectroscopy measurements are predominantly contributed by ISF glucose, the relevant input concentrations to the implicit calibration method should also incorporate the ISF glucose concentrations for consistency. However, blood glucose concentration is the most clinically relevant value and, in a typical clinical setting, blood glucose values are used as reference concentrations since blood sample-based glucose analysis is currently the most reliable and readily available method of measurement. This inconsistency creates calibration errors in the regression vector $\mathbf{b}_{conventional}$, as it is based on both the blood and ISF glucose concentrations which

knowledgments" section.

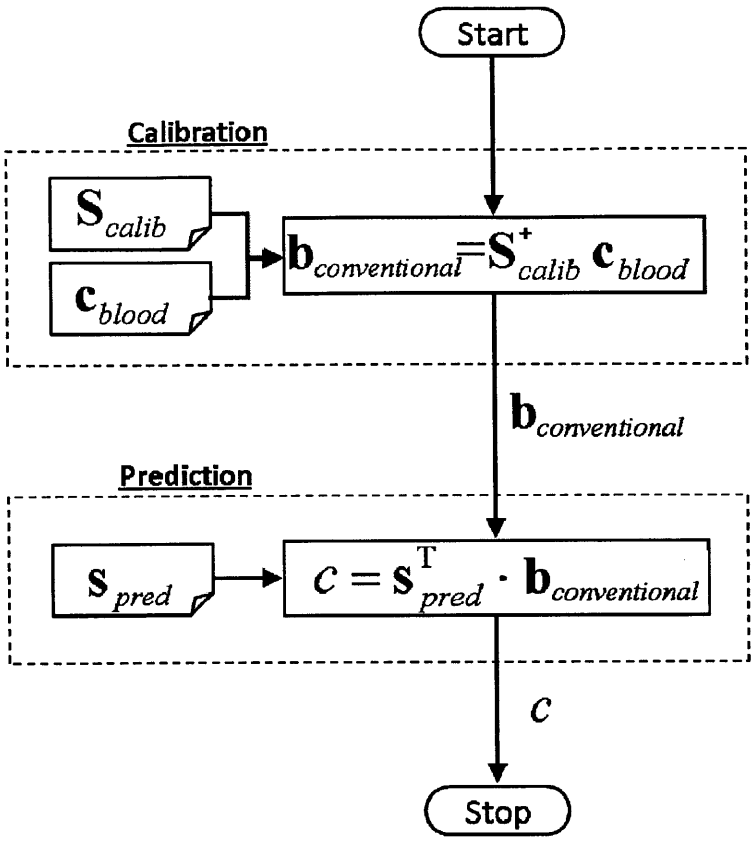

Figure 3-1: Conventional linear regression flowchart. $\mathbf{S}_{calib}$: the matrix of calibration spectra, $\mathbf{S}^{+}_{calib}$: a form of inverse matrix of $\mathbf{S}_{calib}$, $\mathbf{c}_{blood}$: vector of measured reference blood glucose concentrations, $\mathbf{b}_{conventional}$: regression vector obtained by conventional linear regression, $\mathbf{s}_{pred}$: vector of a prediction spectrum, c: predicted glucose concentration.

may be significantly different during rapid changes in glucose levels.

In the prediction step, the predicted glucose concentration c, is obtained by a scalar product of the regression vector $\mathbf{b}_{conventional}$, and the spectrum acquired from the prediction sample $\mathbf{s}_{pred}$ as shown in the following equation:

$$c = \mathbf{s}^{\mathrm{T}}\mathbf{b}_{conventional} \tag{3.2}$$

where superscript T denotes the transpose of the vector. Due to the calibration errors present in the regression vector $\mathbf{b}_{conventional}$, the predicted glucose concentration is reported as the blood glucose concentration c obtained in the above conventional

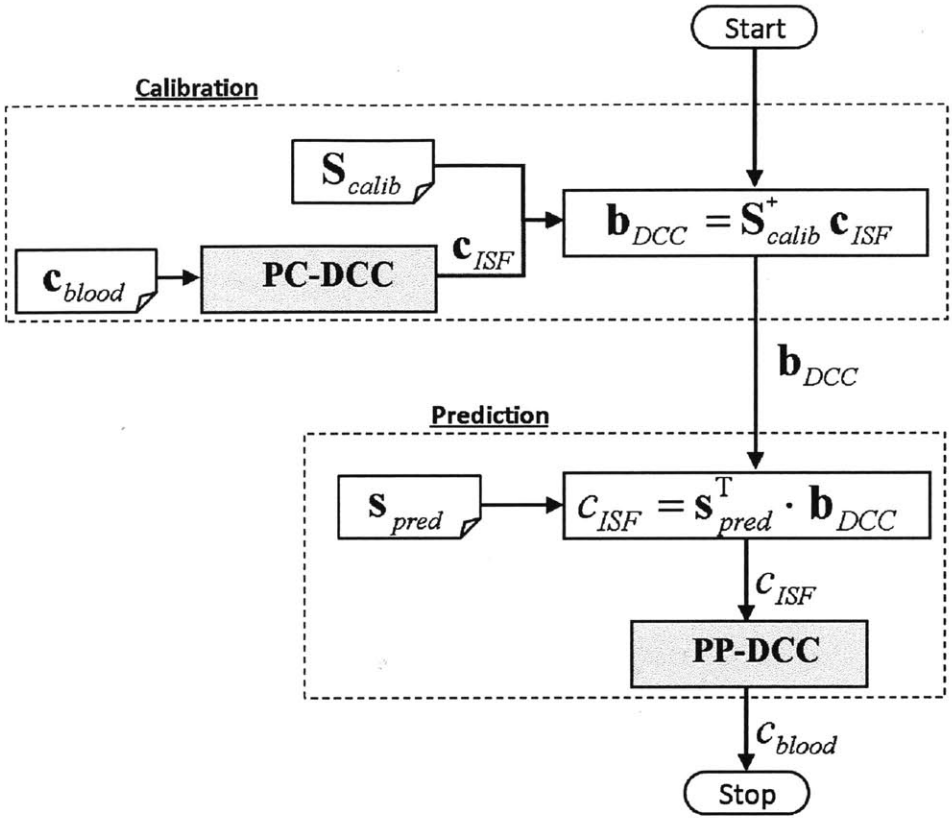

Figure 3-2: DCC-based linear regression flowchart. PC-DCC: Pre-calibration DCC, PP-DCC: Post-prediction DCC, $\mathbf{S}_{calib}$: the matrix of calibration spectra, $\mathbf{S}^{+}_{calib}$: a form of inverse matrix of $\mathbf{S}_{calib}$, $\mathbf{c}_{blood}$: vector of reference blood glucose concentrations, $\mathbf{c}_{ISF}$: vector of ISF glucose concentrations, $\mathbf{b}_{DCC}$: regression vector obtained by DCC, $\mathbf{s}_{pred}$: vector of a prediction spectrum, c_{blood}: predicted blood glucose concentration, c_{ISF}: predicted ISF glucose concentration.

framework is not an accurate representation.

In order to correct for this discrepancy, a new calibration methodology is proposed in which the concentrations are appropriately changed to conform to the spectral measurements. Based on a two compartment mass transfer model, the dynamic concentration correction (DCC) performs transformation of glucose concentrations in two stages:

- Pre-Calibration DCC (PC-DCC)

  Transform the blood glucose concentrations in the calibration data set into their corresponding ISF values before performing calibration of Eq. 3.1. This

ensures that the regression vector **b** is solely based on ISF glucose concentrations.

- Post-Prediction DCC (PP-DCC)

  After calibration, estimate the ISF glucose concentration from a prediction spectrum using Eq. 3.2. Then transform this ISF glucose concentration into the corresponding blood glucose value.

As conceptually described in the flowchart of Fig. 3-2, the purpose of these conversions is to ensure that the core spectroscopic calibration and prediction steps are done in a consistent manner where all glucose concentrations pertains to the ISF glucose concentration. This would reduce the calibration errors arising from the lag between the glucose concentrations in the two compartments. After the calibration and prediction, the ISF glucose concentration can be converted back into the corresponding blood glucose value.

In order to convert between blood and ISF glucose concentrations, a model is developed to describe the glucose transfer across the capillary vessel wall. The blood capillary wall is single endothelial cell thick, and has very small tight junction pores (2~80 nm diameter) through which glucose can be transported by osmotic pressure and passive diffusion across an established concentration gradient [51]. The glucose transfer rate is affected by several variables, such as the rate of blood flow, rate of glucose uptake by the surrounding tissue, and capillary permeability which varies in different anatomical sites. Nevertheless, a simple two-compartment model can be used to describe the macroscopic picture of glucose transfer across the capillary membrane [47, 52, 53]. The change in glucose concentrations within the skin ISF volume, V_{ISF}, can be described as follows:

$$V_{ISF}\frac{\mathrm{d}c_{ISF}}{\mathrm{d}t} = k_M A(c_{BG} - c_{ISF}) - k_U V_{ISF} c_{ISF} \tag{3.3}$$

where c_{ISF} and c_{BG} are the ISF and blood glucose concentrations (mol/cm^3), k_M is the glucose mass transfer coefficient (cm/s), A is the effective mass transfer surface area (cm^2), and k_U is the rate of glucose uptake by the neighboring cells (s^{-1}). Although

k_U is affected by the amount of insulin present in the bloodstream, it can be assumed to be constant due to the observed results that the glucose uptake in subcutaneous skin tissues is largely unaffected by the local insulin concentrations [52, 47]. In fact, the uptake term itself has been observed to be very small for skin tissues, unlike muscle or adipose tissues, therefore it has been ignored ($k_U = 0$) in the analysis [47]. With these assumptions, eq. 3.3 can then be simplified to

$$c_{BG} = c_{ISF} + \alpha \frac{\mathrm{d}c_{ISF}}{\mathrm{d}t} \tag{3.4}$$

where $\alpha (= V_{ISF}/(k_M A))$ is a lumped mass transfer parameter having units of time. The parameter α provides a measure of the lag time arising from the glucose transport and from this point it will be referred to as the characteristic lag time constant. By using eq. 3.4, the blood glucose concentration can be estimated from the spectroscopy-based ISF glucose concentration and the knowledge of the lag time constant and the rate of change in glucose levels. This is done during the post-prediction (PP-DCC) step (Fig. 3-2). In practice, eq. 3.4 needs to be discretized in order to be implemented in digital computers. A first-order estimate of the blood glucose concentration can be obtained by using a finite difference approximation for the derivative term of eq. 3.4:

$$c_{BG}(t) = c_{ISF}(t) + \alpha \frac{c_{ISF}(t) - c_{ISF}(t - \Delta t)}{\Delta t} \tag{3.5}$$

where Δt is the time interval between spectroscopic measurements and ISF glucose concentration estimates. With this discretized expression, the PP-DCC step can be performed in real time using digital computers. It can also be seen that at least two spectroscopic measurements of ISF glucose (at t and at $t - \Delta t$) are required to determine the blood glucose concentration using eq. 3.5. The time interval of measurement, Δt, should be short enough to capture the fastest physiological glucose variations, and it cannot be arbitrarily short as only a limited number of blood withdrawal is allowed during human oral glucose tolerance tests. Based on the fact that it could take as short as 20~30 minutes to reach peak glucose levels from fast-

ing level during oral glucose tolerance tests, Δt was optimized to be 5~10 minutes. Other research laboratories sample blood glucose at similar time intervals ranging from 2.5 to 10 min [54, 52, 20]. To determine the values of the concentrations and their derivatives at intermediate points, spline interpolation can be employed.

In the other portion of the proposed scheme, the pre-calibration DCC (PC-DCC) step, the glucose concentrations are transformed in the opposite direction, from blood glucose to ISF glucose. In order to obtain the expression for PC-DCC, the differential equation of eq. 3.4 can be converted into its integral form:

$$c_{ISF}(t_f) = c_{ISF}(t_i)\exp\left(-\frac{1}{\alpha}(t_f - t_i)\right) + \frac{1}{\alpha}\int_{t_i}^{t_f} c_{BG}\exp\left(-\frac{1}{\alpha}(t_f - t_i)\right)\mathrm{d}t \qquad (3.6)$$

where the definite integral is evaluated from time t_i to time t_f. Similar to the PP-DCC, this integral equation needs to be discretized for practical implementation. This can be achieved by performing integration by parts for the second term of eq. 3.6 and using a numerical integration technique called Simpson's rule to obtain the following equation:

$$c_{ISF}(t_f) = c_{BG}(t_f) + (c_{ISF}(t_i) - c_{BG}(t_i))\exp\left(-\frac{t_f - t_i}{\alpha}\right) - \frac{t_f - t_i}{6}A \qquad (3.7)$$

where

$$A = \dot{c}_{BG}(t_i)\exp\left(-\frac{t_f - t_i}{\alpha}\right) + 4\dot{c}_{BG}\left(\frac{t_i + t_f}{2}\right)\exp\left(-\frac{t_f - t_i}{2\alpha}\right) + \dot{c}_{BG}(t_f) \qquad (3.8)$$

Here, $\dot{c}_{BG}(t)$ refers to the derivative of c_{BG} evaluated at t. A first-order finite difference approximation similar to that employed in eq. 3.5 for the PP-DCC step can be used to approximate $\dot{c}_{BG}(t)$. One complication with this formulation is that the initial ISF glucose value $c_{ISF}(0)$ needs to be determined for the very first time window $[t_i = 0,\ t_f]$. This initial condition can be determined accurately when the ISF glucose and blood glucose concentrations are completely in equilibrium at the beginning of the spectroscopic calibration measurements. Under such conditions, $c_{ISF}(0)$ is determined by steady-state approximation of $c_{BG}(0) = c_{ISF}(0)$ (which

assumes zero glucose uptake by the skin connective tissue as in eq. 3.4). This is typically the case because oral glucose tolerance test (OGTT) protocol requires 8~12 hours of fasting so that the physiological glucose concentration would have stabilized to the fasting (steady-state) level at the beginning of the spectroscopic calibration measurements.

3.3 Formulation of prediction uncertainty arising from physiological lag

The precision of spectroscopy-based calibration models can be quantified by using a prediction error formula derived by Lorber and Kowalski widely known in the chemometrics field, which describes the error propagation for linear multivariate prediction algorithms [55]. This formulation was used previously by Šćepanović et al., to describe the uncertainty in concentration prediction for the limiting case where the noise in the calibration spectra is negligible in comparison to that of the prediction spectra [56]. This is typically the case in most biomedical spectroscopy applications, since CCD or sensor acquisition times can be much longer during calibration than prediction. Under such conditions, when the signal-to-noise ratio (SNR) of the calibration spectra is sufficiently high in comparison to that of the prediction spectra, it can be assumed that a perfectly accurate calibration model can be developed from the calibration spectra. Uncertainty in the predicted concentrations then arises primarily from the spectral overlap between the analyte of interest (glucose) and the other interfering tissue constituents, and the measurement noise in the prediction spectra. Mathematically, this spectroscopic uncertainty for the analyte of interest (glucose) is given by Δc_s [56]:

$$\hat{c} = (\mathbf{s} \pm \Delta\mathbf{s})^T \cdot \mathbf{b} = \mathbf{s}^T \cdot \mathbf{b} \pm \Delta\mathbf{s}^T \cdot \mathbf{b} = c \pm \Delta c_s \tag{3.9}$$

where

$$\Delta c_s = \frac{\sigma}{S_g} \cdot \eta \tag{3.10}$$

Here, $\Delta\mathbf{s}$ represents the noise in the prediction spectrum $\mathbf{s}$, while $\hat{c}$ and c are the estimated and actual analyte concentrations in the prediction sample, respectively. As the modeling noise is ignored in computation of the limiting uncertainty, $\mathbf{b}$ represents the noise-free regression vector for glucose concentration. σ is a measure of the noise magnitude in the prediction spectrum, S_g quantifies the signal strength of glucose spectrum at unit concentration, and η indicates the amount of overlap (non-orthogonality) between glucose spectrum and the other interfering spectral components in the tissue, such as proteins, lipids, and water.

However, in addition to this spectroscopic uncertainty, there is an additional element of prediction uncertainty for transdermal glucose measurements that arises from the physiological lag between blood and ISF glucose levels. Using similar error propagation analysis as presented above, the following subsections describe the formulation of the limiting uncertainty in glucose concentration prediction due to the physiological lag, with and without DCC.

3.3.1 Limiting uncertainty due to physiological lag without DCC

Considering the effect of physiological lag in skin tissues, eq. 3.9 can be rewritten in terms of the estimated ($\hat{c}_{ISF}$) and actual (c_{ISF}) ISF glucose concentrations.

$$\hat{c}_{ISF} = (\mathbf{s} \pm \mathbf{\Delta s})^T \cdot \mathbf{b} = c_{ISF} \pm \Delta c_s \tag{3.11}$$

Given the correct lag time constant for the prediction sample (α_{actual}), the actual blood glucose concentration c_{BG} can be determined from the actual ISF glucose concentration c_{ISF} using eq. 3.4, on the basis of the blood and ISF two-compartment model. The value of the actual ISF glucose concentration from eq. 3.11 can be substituted into eq. 3.4 to give

$$c_{BG} = c_{ISF} + \alpha_{actual}\frac{\mathrm{d}c_{ISF}}{\mathrm{d}t} = \hat{c}_{ISF} + \alpha_{actual}\frac{\mathrm{d}\hat{c}_{ISF}}{\mathrm{d}t} \pm \Delta c_s \tag{3.12}$$

Without DCC, the estimated ISF glucose concentration $\hat{c}_{ISF}$ is reported in the conventional model as the blood glucose concentration $\hat{c}_{BG}$:

$$\hat{c}_{BG} = \hat{c}_{ISF} \tag{3.13}$$

Substituting eq. 3.13 into eq. 3.12 and rearranging, gives

$$\hat{c}_{BG} = c_{BG} - \alpha_{actual}\frac{\mathrm{d}c_{ISF}}{\mathrm{d}t} \pm \Delta c_s \tag{3.14}$$

This implies that, without DCC, the limiting uncertainty in the concentration estimate under the conventional calibration method has two separate contributions:

1. The uncertainty resulting from the measurement noise in the prediction spectrum and the spectral overlap, Δc_s
2. The uncertainty due to the glucose physiological lag, $\Delta c_{conv} = \alpha_{actual}\frac{\mathrm{d}c_{ISF}}{\mathrm{d}t}$

While the first uncertainty was well-characterized by Šćepanović et al. [56], the latter uncertainty is has not been examined before.

Figure 3-3 illustrates the two contributing factors of the prediction uncertainty. In this figure, the simulated blood and ISF glucose data in panel A (which mimics the glucose profiles obtained from an oral glucose tolerance test) are plotted against each other to produce the solid curves in panel B. The uncertainty due to the noise and spectral overlap in the prediction spectrum is marked as Δc_s. It is evident that the physiological lag between the blood and ISF glucose profiles in (A) introduces a hysteresis-like closed loop behavior when blood glucose is plotted against ISF glucose, showing the lack of a one-to-one correspondence between the glucose concentrations in the two compartments. When the glucose levels are increasing, the blood glucose concentrations are greater than the corresponding ISF glucose concentrations (labeled RISE). Similarly, the set of values obtained during the falling phase is represented by the concave downward curve (labeled FALL). Specifically, it is observed that, given an ISF concentration of 148 mg/dL at point P, the actual blood glucose concentration could be either 132 mg/dL (Q) or 158 mg/dL (T). However, conventional methods

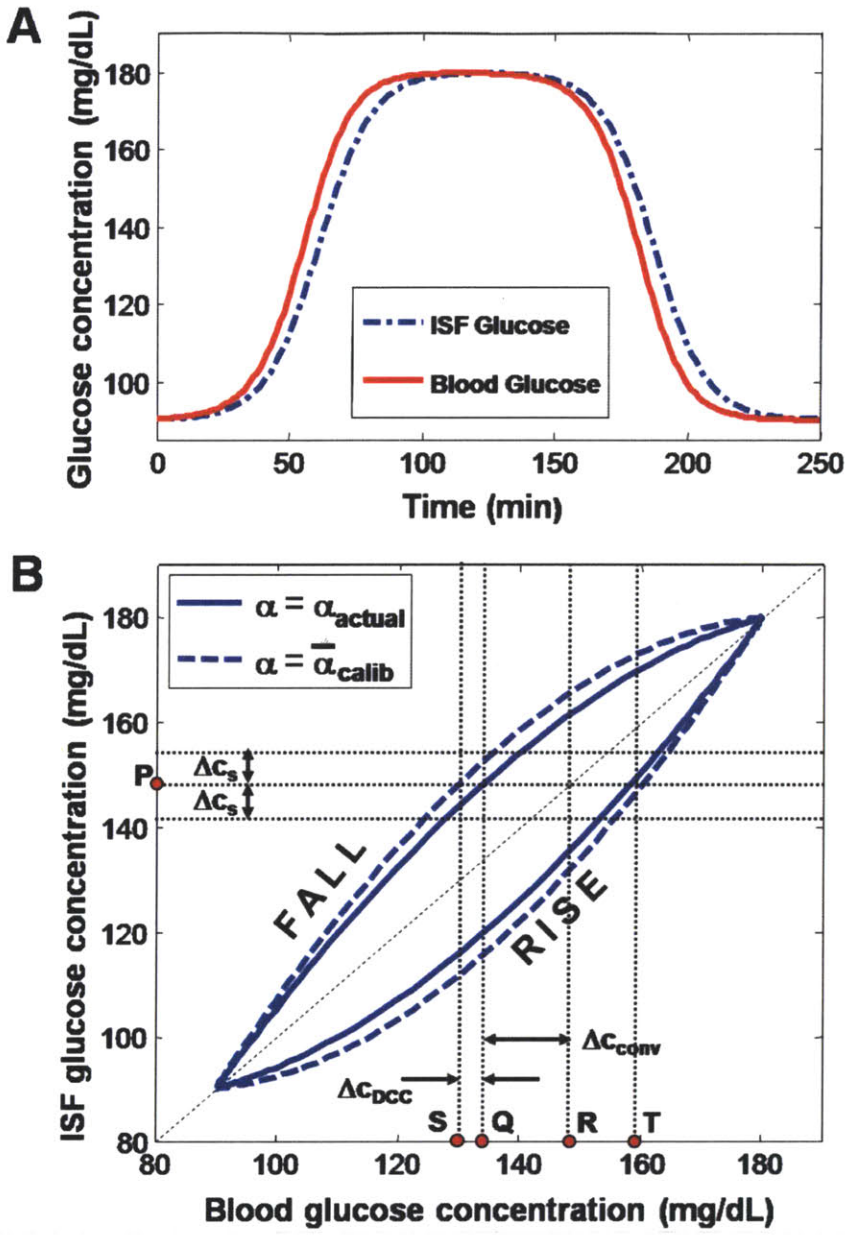

Figure 3-3: Uncertainty in glucose prediction due to physiological lag. (A) Schematic representation of blood and ISF glucose concentration profiles, similar to those obtained during a typical glucose tolerance test. (B) ISF and blood glucose concentrations shown in panel A plotted against each other. The solid curve shows the actual ISF and blood glucose relationship, while the dotted curves represent the deviations from actual values due to noise and spectral overlap. Without the knowledge about the glucose dynamics, it cannot be determined whether the blood glucose concentration lies at point Q or T, for a given ISF glucose concentration at point P. With the knowledge about whether the glucose level is rising or falling, the uncertainty in the estimation of the blood glucose concentrations is significantly reduced.

without the knowledge about the glucose dynamics would predict, for example, 148 mg/dL (R), giving rise to a significant error in prediction Δc_{conv}, as marked by the distance between points Q and R.

3.3.2 Limiting uncertainty due to physiological lag with DCC

Unlike the conventional model, the DCC method explicitly accounts for the physiological glucose dynamics. Specifically, the post-prediction equation (PP-DCC) is used to transform the spectroscopy-based ISF glucose estimate ($\hat{c}_{ISF}$) to a corresponding blood glucose value ($\hat{c}_{BG}$), and this step needs to be considered in evaluating the limiting uncertainty. As the correct lag time constant in the prediction sample is unknown in a real clinical setting, some uncertainty due to the physiological lag is introduced via the PP-DCC step. Similar to the previous subsection, the aggregate average of the lag time constants obtained from the calibration samples is used to approximate the actual lag time constant in the prediction sample. With this approximation, the PP- DCC equation can be rewritten as

$$\hat{c}_{BG} = \hat{c}_{ISF} + \overline{\alpha}_{calib}\frac{\mathrm{d}\hat{c}_{ISF}}{\mathrm{d}t} \tag{3.15}$$

where $\overline{\alpha}_{calib}$ refers to the average value of α computed from the calibration samples. Substituting eq. 3.11 into eq. 3.15 gives

$$\hat{c}_{BG} = c_{ISF} \pm \Delta c_s + \overline{\alpha}_{calib}\frac{\mathrm{d}c_{ISF}}{\mathrm{d}t} \tag{3.16}$$

The deviation of $\overline{\alpha}_{calib}$ from the actual lag time constant in the prediction sample, α_{actual}, can be written as

$$\overline{\alpha}_{calib} = \alpha_{actual} \pm \Delta\alpha \tag{3.17}$$

where $\Delta\alpha$ is the error (uncertainty) in the estimation of the lag time constant. Substituting eq. 3.17 into eq. 3.16 and rewriting the first term of the above equation as c_{BG} gives

$$\hat{c}_{BG} = c_{BG} \pm \Delta\alpha\frac{\mathrm{d}c_{ISF}}{\mathrm{d}t} \pm \Delta c_s \tag{3.18}$$

Equation 3.18 implies that the net uncertainty is a combination of the uncertainties arising from the spectral noise and overlap (Δc_s) and the physiological lag (Δc_{DCC}=$\Delta\alpha\frac{dc_{ISF}}{dt}$), which is analogous to eq. 3.14 for the case without DCC. However, the magnitude of uncertainty introduced due to the physiological lag is much greater for the case without DCC. The lag uncertainty for the conventional calibration model case without DCC is proportional to α_{actual}, while that for the case with DCC is proportional to $\Delta\alpha$. This can be seen in Fig. 3-3B. In this figure, the dashed curves connect the points whose coordinates are given by the blood and ISF glucose concentrations estimated by the model, in contrast to the solid curve that represents actual blood and ISF glucose concentrations. Since the exact value of the lag time constant α is not known, the estimated blood glucose concentrations will differ from the actual blood glucose concentrations by the product of the rate of change in the glucose concentration and the estimation uncertainty of the lag time $\Delta c_{DCC} = \Delta\alpha\frac{dc_{ISF}}{dt}$. The dashed (DCC-estimated) curve is computed using eq. 3.15, whereas the blood and ISF glucose concentrations (solid) curve are related by eq. 3.4. In Fig. 3-3, it can be seen that Δc_{DCC} (the distance between Q and S), is substantially smaller than Δc_{conv} (the distance between Q and R), as long as the lag time constant α used in the DCC model is a reasonable approximation of the actual lag time constant.

3.4 Materials and methods

Numerical simulations and data analysis were performed to study the effect of DCC on glucose measurement performance by the calibration model, and to estimate the lag time constant α in a human population. For the numerical simulations, ISF and blood glucose concentration data sets described by Steil et al.[52] were used to generate tissue Raman spectra for calibration and prediction. The simulations were also used to understand the relationship between the SNR in the spectral data set and performance of the conventional and DCC calibration models. To investigate the lag time distribution in a human population, data sets obtained from previous clinical studies on human volunteers were employed [57]. In addition, the prediction

uncertainty due to the physiological lag was characterized.

3.4.1 Implementation of DCC on simulated Raman spectra

Steil and co-workers monitored blood and ISF glucose concentrations in non-diabetic human subjects during glucose clamping [52]. Glucose clamping is a clinical study procedure developed by Andres and Tobin in which glucose is infused into the human subject at a variable rate (either with or without insulin infusion) in a controlled manner to maintain a constant level of blood glucose levels [46]. Although the glucose clamping technique was originally developed to observe the patient's sensitivity to insulin as well as the capacity to secrete insulin [46], the technique is also useful for artificially "clamping" the blood glucose concentration at the desired level. In the study by Steil et al., after 10-12 hours of overnight fasting, glucose was sequentially clamped at approximately 5, 4.2, and 3.1 mM (1 mM concentration of glucose $\approx$ 18 mg/dL) for 90 min each by insulin and glucose infusion and subsequently allowed to return to normal physiological glucose levels. During this procedure, the ISF glucose was measured by two MiniMed (Medtronic, Inc.) subcutaneous amperometric glucose sensors implanted under the abdominal skin. Blood was withdrawn at regular intervals for blood glucose measurements using a clinical glucose analyzer. From this clinical study, the blood and ISF glucose concentration data obtained from 90 to 380 min after initial insulin and glucose infusion was used in the numerical simulations (Fig. 3-4).

This glucose concentration data set was divided into calibration (spanning from 90 to 220 min) and prediction (from 230 to 380 min) sets, respectively. Using the ISF glucose concentrations, simulated Raman spectra were generated by forming weighted linear combinations of the constituent Raman spectra of glucose, creatinine, and urea, which were measured using a Raman spectroscopy setup designed for transdermal glucose detection [57, 35]. The weight assigned for the Raman spectrum of glucose was varied as determined by the ISF glucose concentrations of the Steil data set, while the weights for the remaining tissue consistent spectra were randomly varied within 2% of a constant value, to mimic the minute changes observed in these constituents

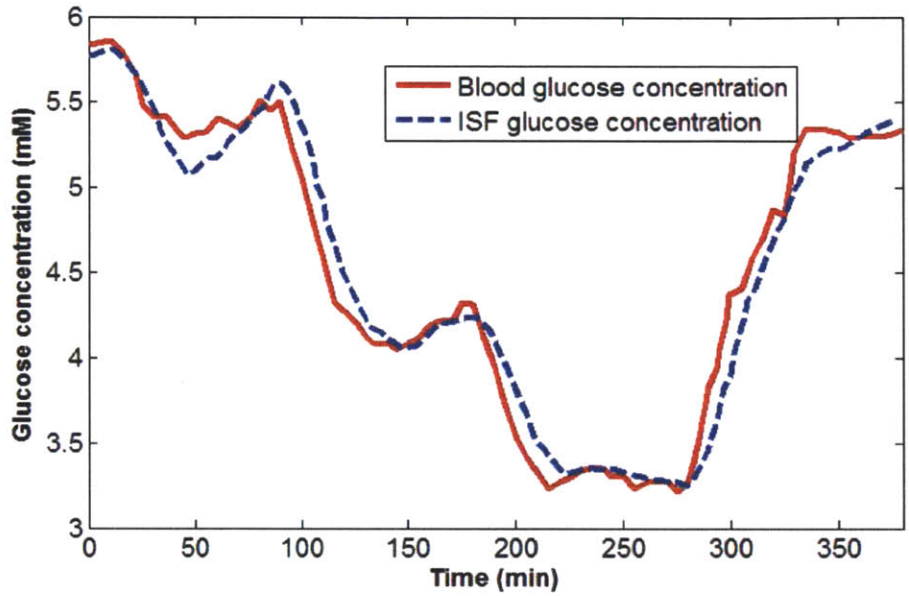

Figure 3-4: Blood and ISF glucose concentration-time profiles measured from a normal human volunteer during insulin-induced hypoglycemia. Glucose was clamped at 5, 4.2, and 3.1 mM and subsequently allowed to return to normoglycemic levels. It is observed that the ISF glucose, measured by subcutaneous amperometric sensors, consistently lags behind blood glucose concentrations during both the rising and falling phases. In contrast, they are equilibrated to nearly identical values during the clamping phases. Reprinted from ref. [52], Copyright 2005, with permission from Springer Science and Business Media: Diabetologia.

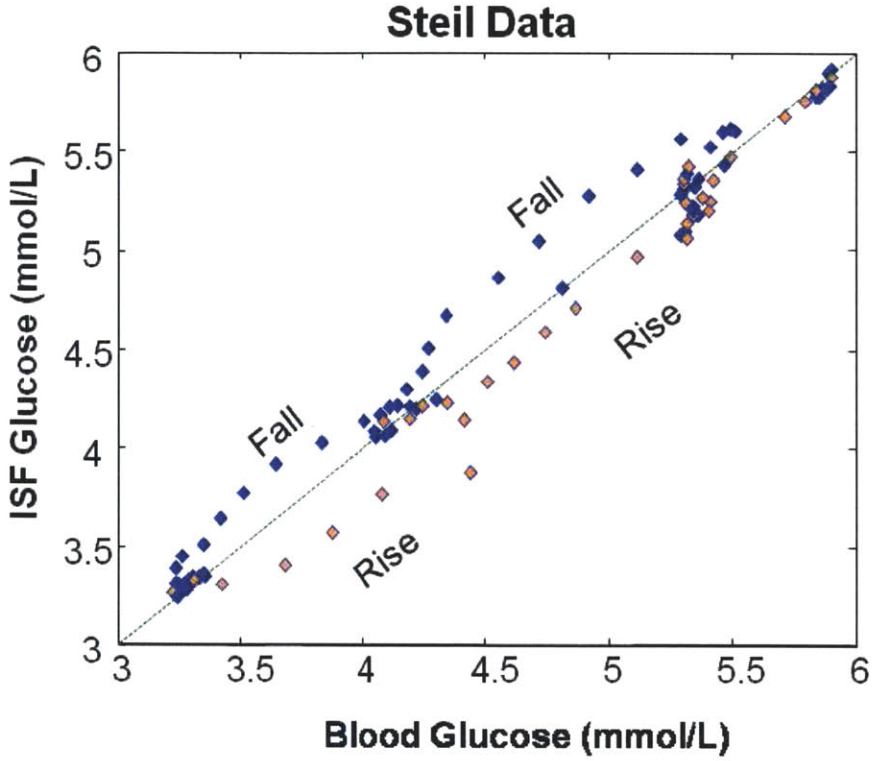

Figure 3-5: The same data as Fig. 3-4, with the ISF glucose concentrations plotted against the corresponding blood glucose concentrations.

during typical glucose tolerance and clamping tests. In addition, to simulate normal experimental conditions, zero-mean Gaussian white noise was added to the mixture spectra at varying levels of SNR (20-40 dB) to study its effect on the prediction performance of the calibration models. In order to optimize the lag time constant α and the number of loading vectors LV for partial least squares (PLS) linear regression, an iterative grid-search was performed for the optimal combination of parameters that produced the smallest calibration error, in the appropriate ranges of α (0 to 20 min) and LV (2 to 10). Using PC-DCC (eq. 3.6), all but one of the reference blood glucose concentrations were converted to the corresponding ISF glucose values to develop a leave-one-out cross-validation calibration model composed purely of ISF glucose concentrations. The developed calibration model was then used to predict the ISF glucose concentration at that point. Subsequently, PP-DCC (eq. 3.4) was used to convert the predicted ISF glucose concentration back into the corresponding

blood glucose value. This process was repeated in a round-robin fashion until all data points were used once as the validation data. The calibration error was calculated by comparing the predicted blood glucose concentrations with the reference values to produce the root-mean-squared error of cross-validation (RMSECV). The resulting optimal values α_{opt} and LV_{opt} that produced the smallest RMSECV were used to calculate the PLS regression vector $\mathbf{b}_{opt}$. On a separate portion of the data set, prospective prediction was performed by taking the scalar product of the prediction spectra with the calibrated $\mathbf{b}_{opt}$ (eq. 3.2), producing the ISF glucose predictions. These ISF glucose values were converted to the blood glucose values using PP-DCC, where α_{opt} was used in place of α in eq. 3.4. Then the root-mean-squared error of prediction (RMSEP) was computed from the predicted blood glucose concentrations and the reference blood glucose values.

The glucose prediction performance of the DCC-based regression model was then compared with that of the conventional PLS regression model, as well as a regression model incorporating a fixed time delay between blood and ISF glucose concentration profiles. In addition, 20 simulations were carried out at different values of SNR in the spectral data set (both calibration and prediction) to observe the effect of spectral noise on the prospective prediction errors.

3.4.2 Implementation of DCC on Raman spectra measured from human subjects

DCC-based calibration and cross-validation was implemented on clinical data sets consisting of blood glucose concentrations and skin tissue Raman spectra obtained from human subjects. The α and LV optimization process described above was used as a method for estimating the value of the lag time constant in a human population. Raman spectra were collected from the forearms of healthy Caucasian and Asian human volunteers undergoing OGTT. The age of the tested human volunteers was in the range of 21-29, with a mean of 24.5. For the excitation source, an 830 nm diode laser (Process Instruments) was used at an average power of 300 mW in a 1

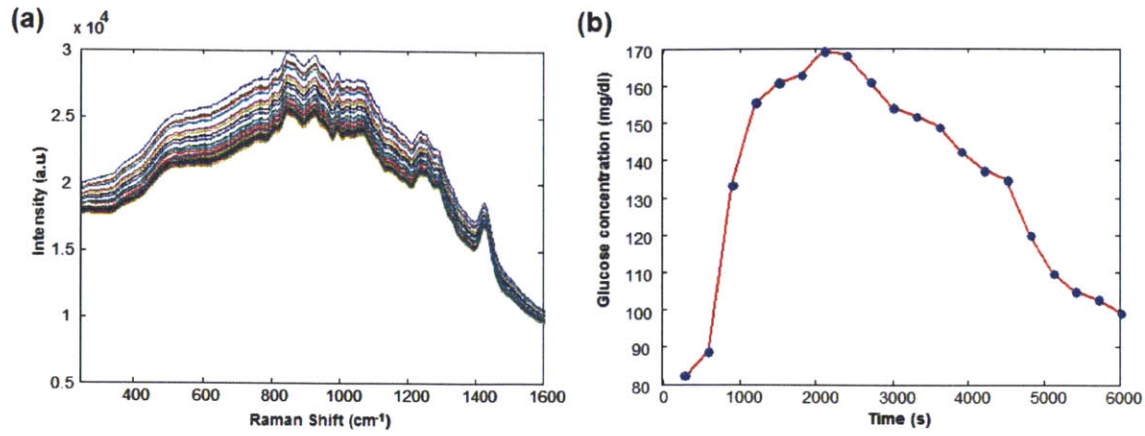

Figure 3-6: Raman spectra and glucose profile during OGTT. (a) Representative Raman spectra acquired from a human volunteer during OGTT. (b) Blood glucose concentration profile measured over the same time.

mm^2 spot. An f/1.8 spectrograph (Kaiser Optical Systems) was coupled to a liquid nitrogen-cooled CCD (1340 $\times$ 1300 pixels, Roper Scientific) for spectral dispersion and acquisition. For each volunteer, OGTT was initiated by the ingestion of a glucose-rich solution, and Raman spectra were collected every 5 minutes over a 2 hour period. At the same time, the reference blood glucose concentrations were measured every 10 minutes from blood samples using a clinical glucose analyzer (HemoCue, Inc.), and spline interpolation was used to correlate the measured blood glucose concentrations with the spectra collected at intermediate time points. (This study protocol was approved by the MIT Committee on the Use of Humans as Experimental Subjects.) Data sets from volunteers exhibiting motion artifacts, inadequate SNR in the acquired spectra, and impaired glucose tolerance characteristics were excluded from further analysis.

A representative set of tissue Raman spectra and the corresponding blood glucose concentration profile acquired from one of the human volunteers are shown in Fig. 3-6. For the selected volunteer data sets, DCC calibration was performed using the same leave-one-out cross-validation routine as described in the previous subsection. Iterative grid search was performed on the measured Raman spectra and reference blood glucose concentrations to determine the optimal value of α and LV for each

individual. In addition, conventional PLS calibration was also performed on the same data sets to compare the cross-validation errors. The mean and standard deviation of α determined from the human subjects were used to approximate α_{actual} and $\Delta\alpha$, respectively. These were the estimates of uncertainty due to physiological lag for the conventional (α_{actual}) and DCC-based ($\Delta\alpha$) calibration methods. Finally, these uncertainty estimates were also compared with the spectroscopic uncertainty, Δc_s.

3.5 Results and discussion

3.5.1 Implementation of DCC on simulated Raman spectra

Numerical simulations were used to compare the prospective prediction capability of the conventional and DCC calibration models. DCC implementation was found to reduce the RMSECV of the simulated data set from 0.15 mM to 0.04 mM, when the measured ISF glucose concentrations were used for computing the cross-validation errors. In comparison, the RMSECV for fixed timed delay PLS processing was computed to be 0.07 mM. These simulation results were obtained for an SNR of 40 dB.

Figure 3-7 shows the measured ISF glucose concentrations plotted together with cross-validated glucose concentrations from the conventional and DCC calibration models. It can be seen here that the ISF glucose concentration profile generated with DCC closely matches the measured ISF glucose concentrations, while that generated without DCC shows significantly larger deviations. The cross-validation routine also optimized the lag time constant for the DCC calibration model and the number of loading vectors for both models. For this data set, the characteristic lag time constant, α_{opt}, was determined to be 6.1 minutes, in agreement with the experimentally observed values of 6-8 minutes [52]. Figure 3-8 shows the results of prospective prediction, in which the measured blood glucose concentration profile is plotted alongside the prediction profiles, with and without DCC. When the calibration models were applied prospectively to the prediction data set, the DCC model showed significantly improved prediction accuracy (RMSEP = 0.14 mM) compared with the conventional

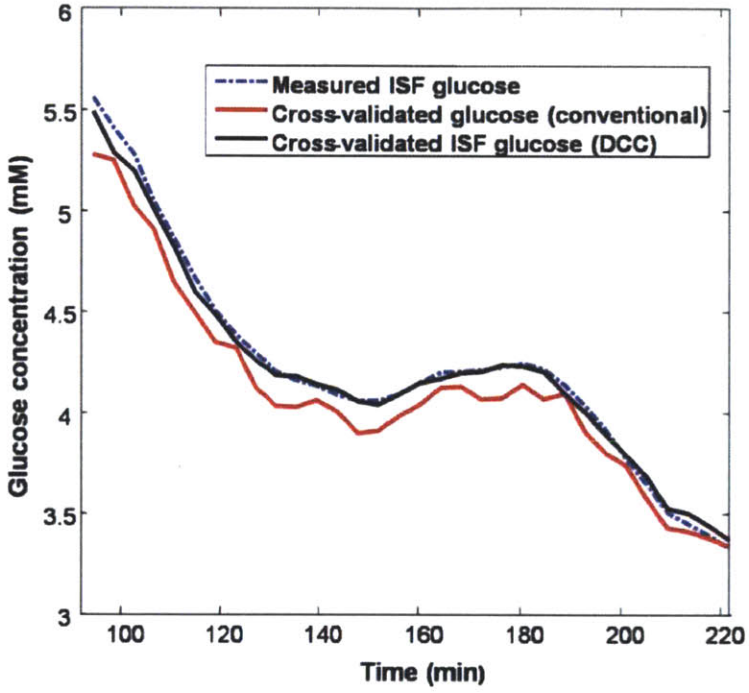

Figure 3-7: Cross-validation results of conventional (red) and DCC (black) calibration methods applied to the simulated data set. The measured ISF glucose concentration values are given by the blue dotted line. In the DCC calibration process, the lag time constant, α_{opt}, was optimized to be 6.1 minutes.

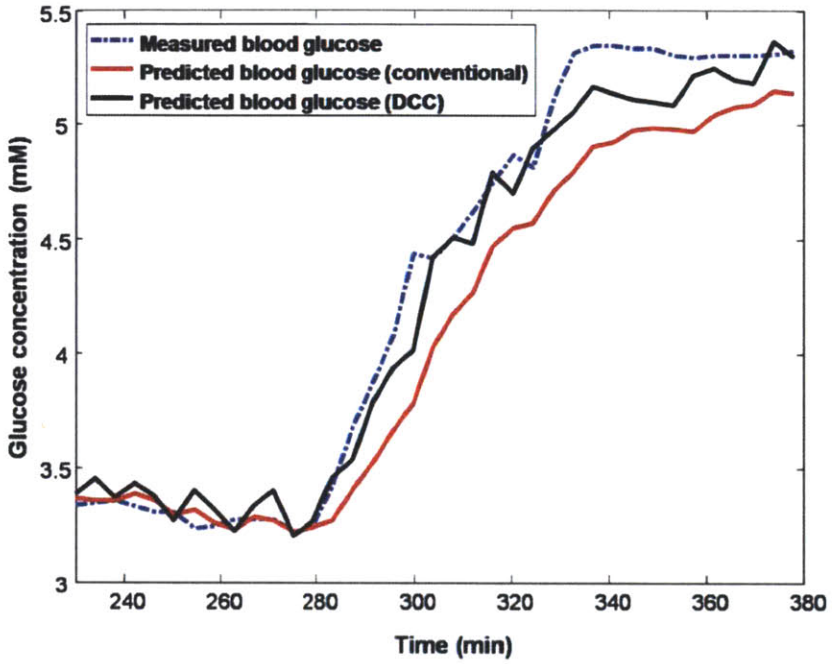

Figure 3-8: Prospective prediction results of conventional (red) and DCC-based (black) calibration methods applied to the simulated data set. The measured blood glucose concentration values are given by the blue dotted line.

PLS scheme (RMSEP = 0.28 mM). In comparison, the simple fixed time delay PLS processing had an RMSEP of 0.26 mM, which is a slight improvement over conventional PLS implementation, but still significantly poorer than the DCC performance. From these results, it can be seen that calibration during non-equilibrium conditions leads to systematic errors, giving rise to much higher prediction errors (Fig. 3-8) than estimated during cross-validation (Fig. 3-7). In the extreme case, during rapidly rising and declining glucose concentrations, the presence of such errors could cause the predicted glucose concentration to have no statistically significant correlation with the actual glucose concentrations.

The accuracy of blood glucose concentration prediction with and without DCC was also compared at varying levels of SNR in the spectral data set. Figure 3-9 shows a plot of the RMSEP of blood glucose prediction with conventional and DCC calibration models as a function of SNR. As expected, an increase in the noise level corresponded to an increase in error values in both conventional and DCC-based cal-

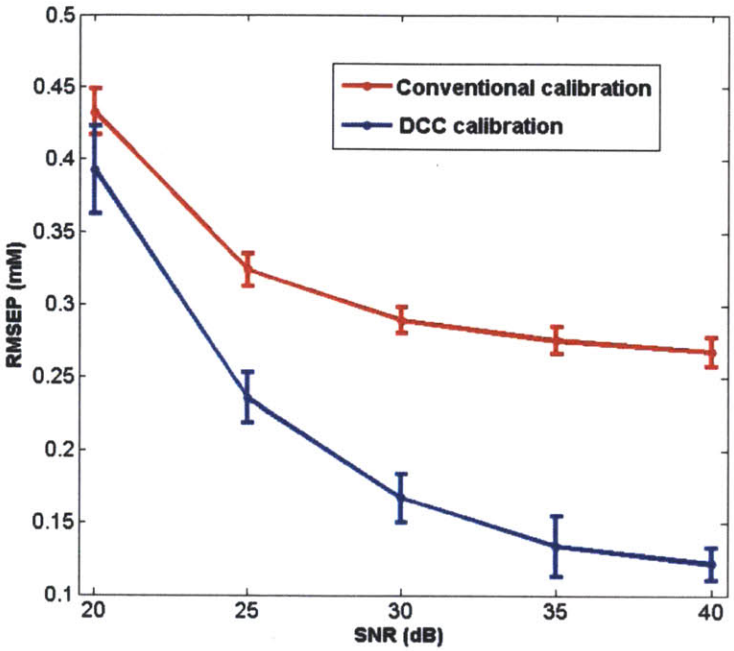

Figure 3-9: RMSEP obtained for conventional (red) and DCC (blue) calibration models, applied to the simulated data set, as a function of increasing SNR. The error bars represent the standard deviation of RMSEP for 20 iterations.

ibrations. However, under all tested values of SNR, the prediction errors of DCC calibration models were consistently smaller compared with those of the conventional PLS models. It was also observed that the mean α_{opt} was essentially noise-insensitive, although the variance from the mean α_{opt} were larger for lower SNR (e.g., the standard deviation in α was computed to be 0.05 and 0.5 minute at 40 and 20 dB, respectively). From these results, it can be seen that when developing a spectroscopic glucose calibration model under non-equilibrium conditions, a time series of multiple glucose measurements are required in order to capture the glucose kinetics. It should also be noted that applying non-linear or enhanced calibration schemes, such as support vector machines [58] or hybrid calibration methods [29, 30], alone would not alleviate inconsistencies in the calibration models as they do not address the lack of one-to-one correspondence between the ISF and blood glucose concentrations (Fig. 3-3). Nevertheless, when used in conjunction with DCC, such calibration schemes may further improve the prediction accuracy.

Table 3.1: Cross-validation results of calibration models applied to the human subject data, with and without DCC.

subject	number of data points	*with DCC*		*without DCC*	change in RMSECV (%)
		α_{opt} (min)	RMSECV (mM)	RMSECV (mM)	
1	25	9.5	0.87	1.07	19.1
2	26	11.5	0.52	0.72	27.6
3	26	10.5	0.70	0.97	28.6
4	30	11.1	1.02	1.08	5.7
5	25	8.4	0.68	0.79	13.4
6	26	8.4	0.64	0.82	22.0
7	25	7.5	0.72	0.51	17.6
8	29	8.1	0.76	0.87	12.4
9	31	8.3	0.96	1.00	3.4
10	27	12	0.50	0.53	5.3

3.5.2 Implementation of DCC on Raman spectra measured from human subjects

In real clinical situations, the number of tissue constituents in the skin Raman spectra are far greater than the simple three constituents (glucose, creatinine, and urea) employed in simulated Raman spectra described in the previous subsection. However, even under such challenging conditions, DCC-based calibration methods performed significantly better than conventional calibration models. Table 3.1 summarizes the results of leave-one-out cross-validation performed on the data set from each human subject, using DCC calibration as well as the conventional PLS routine. Here, it can be observed that application of DCC reduced the RMSECV for the blood glucose concentration estimates by 15.5% on average, with a maximum decrease of 28.6%.

As mentioned previously in the formulation of DCC, it has been assumed that the sampling volume of the skin Raman spectroscopy measurement is a subset of the interstitial fluid space. This assumption was based on the facts that

1. NIR light has a penetration depth of 1 mm in skin tissue.

2. The blood vessels contribute only 5% to the total skin volume [41], with the outermost epidermis being completely avascular.

However, a small fraction of the inelastically scattered (Raman) light still arises from the glucose residing in the blood capillaries. While this results in a slight reduction in the value of the lag time constant, α, the proposed DCC model is sill effective in improving consistency in the calibration model when the spectral contribution of blood glucose is small compared to that of ISF glucose, which applies to most skin Raman spectra. The results also suggest that the value of the lag time constant (when measured from the same anatomical site) is fairly constant for the tested human volunteer population. In Table 3.1, the mean of the lag time constant α, 9.5 minutes, is significantly larger than the standard deviation, 1.6 minute. It should be noted that in this human subject study, the skin Raman spectra were always measured from the ventral forearm to minimize the spectral variations arising from different anatomical sites [57]. The relatively small variation in α indicates that the mean lag time of the calibration set provides a fairly accurate approximation to the lag time in the ventral forearm skin of the general human population.

In addition, these results suggest that the physiological lag time constant in human population can be measured optically [49], using the spectroscopy and analysis methods described in this chapter. Similar lag time of 10 minutes was also observed by NIR absorption spectroscopy study performed by Marbach et al. on human lips [19]. Previous attempts with subcutaneously implantable amperometric sensors have been observed to have significant lag that is inherent in the sensor electrochemistry, which obscures the precision of the physiological lag measurements [54]. In addition to the sensor-specific lag of the subcutaneous amperometric monitors, the difference in lag time constants observed from the numerical simulations using the Steil data set (6.1 minutes) and the clinical studies on human volunteers (9.5 $\pm$ 1.6 minutes) can be attributed to

1. The difference in the composition of glucose (i.e., the proportion of blood and ISF) sampled by the spectroscopic and amperometric sensors.

2. The difference in the anatomical sites (abdominal vs. forearm skin) used for measurements, which may also involve differences in the degree of tissue vascu-

larization.

3. The variations in the population demographics studied in the two studies.

Although changes in blood glucose concentrations typically precede those of the ISF glucose concentrations, some groups have observed that ISF glucose can fall in advance of blood glucose during the time of declining glucose levels [59, 60, 61] while the opposite is true during the rising phase. In such asymmetric situations, a modified DCC model can be implemented by employing two distinct α values (which may even be negative) during the rising and falling phases through a piecewise application of eqs. 3.4 and 3.5.

The mean and standard deviation of α obtained on the human volunteer data set were also employed in determining the physiological lag uncertainties for the DCC and conventional calibration methods. For the conventional calibration method, the uncertainty was calculated as $\alpha_{actual}\frac{\mathrm{d}c_{ISF}}{\mathrm{d}t}$, where the mean α of the human volunteers was used for α_{actual}. During rapid increase in glucose levels, the concentration of glucose in either compartment can change by 2 mg/dL/min (0.11 mM/min) [42]. Using these values, it could be seen that, for the conventional calibration method, the prediction uncertainty due to lag amounted to approximately 1.1 mM. For the DCC model, the uncertainty due to lag could be computed by $\Delta\alpha\frac{\mathrm{d}c_{ISF}}{\mathrm{d}t}$, where $\Delta\alpha$ was approximated by the standard deviation of α obtained from the human volunteer data set. Using this value of $\Delta\alpha$, the lag uncertainty for the DCC calibration method was calculated be 0.18 mM. This corresponds to approximately 6-fold reduction in the lag uncertainty on application of DCC.

As shown previously, eq. 3.10 describes the uncertainty in the spectroscopic glucose concentration measurement arising from the measurement noise in the Raman spectrum and the spectral overlap between glucose and the interfering tissue constituents [56]. Using tissue phantom Raman spectra measured from a laboratory-based setup, this spectroscopic uncertainty, Δc_s, was estimated to be 1.04 mM [35]. Previous studies suggested that this spectroscopic uncertainty would describe the lowest concentration at which glucose could be detected in the tissue [56]. However,

this does not provide the full picture for the case of transdermal glucose detection, as it ignores the uncertainty arising from the lag between blood and ISF glucose concentrations. When conventional calibration methods were used during rapid changes in glucose levels, the uncertainty due to lag (1.06 mM) was estimated to be comparable to the spectroscopic uncertainty (1.04 mM). Therefore, the total uncertainty (2.1 mM) would be nearly twice as large as the previously accepted value (1.04 mM). On the other hand, applying the DCC-based calibration method significantly reduces the uncertainty due to lag, producing a total uncertainty of 1.22 mM, which predominantly arises from the spectroscopic uncertainty.

3.6 Conclusion

The physiological lag between blood and ISF glucose concentrations creates calibration errors in conventional spectroscopic calibration methods. The lack of knowledge of the glucose kinetics also creates additional uncertainty in the estimated glucose concentration, which is comparable in magnitude to the uncertainty arising from noise and non-orthogonality in the spectral data. Based on a first order mass transfer model, the DCC-based calibration method explicitly accounts for the glucose kinetics and removes the inconsistencies in the calibration and prediction steps. It has been demonstrated that implementing DCC significantly improves accuracy and reduces the uncertainty in spectroscopic blood glucose estimation. The resulting improvement in blood glucose estimates would enhance the ability of Raman spectroscopy to detect dangerously low blood glucose levels. In addition, by using the information about the direction and rate of change in glucose concentrations, an impending hypoglycemia could be detected in a timely manner to initiate preventive intervention. Finally, the lag time α optimization process outlined in the DCC calibration procedure was able to estimate the physiological lag time constants from non-diabetic human subjects. Since it is well-known that inadequate glycemic control causes microvascular and macrovascular changes [62], repeating the study on diabetic population may reveal differences in the physiological lag time constants between the two populations.

THIS PAGE INTENTIONALLY LEFT BLANK

Chapter 4

Monte Carlo study of transmission mode Raman spectroscopy

4.1 Introduction

With the introduction of Raman spectroscopy as a a non-invasive method of analyzing bulk biological tissues, it became ever more important to consider the implications of the Raman light excitation and collection geometry. Unlike homogeneous samples such as purified chemical compounds or crystals, many biological tissue targets are heterogeneous, and the Raman light excitation and collection geometry radically affects the shape and size of the optical sampling volume. Depending on the application, a specific portion of the tissue may be targeted by varying the Raman light excitation and collection geometry.

The most commonly used geometry for the collection of tissue Raman spectra is the back-scattered mode geometry, where the Raman excitation light source and the collection optics are on the same side of the tissue to collect the Raman scattered light that returns toward the excitation source. In this configuration, most of the tissue sampling volume is located near the tissue surface, and a significant amount of tissue light scattering is required in order for the Raman scattered light to return back toward the excitation light source. In most biological tissues, the following diffusion

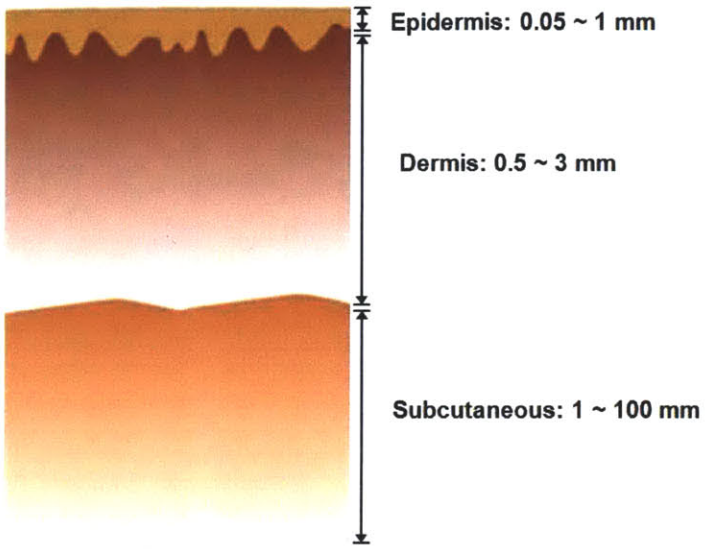

Figure 4-1: The multiple layers of human skin tissue. The outermost layer is the epidermis, which is mainly composed of the keratinocytes, melanocytes and the stratum corneum (dead keratinocytes). There are no blood vessels and very little glucose present in the epidermis. Beneath the epidermis is the dermis, which is mainly composed of fibroblasts, macrophages and adipocytes surrounded by collagen and elastin matrix. It has very few capillary vessels and the cells are mostly bathed in interstitial fluid. Further down below, the subcutaneous tissue is mostly composed of adipocytes and larger blood vessels. The thicknesses of each layer can significantly depending on the anatomical site.

approximation holds

$$\mu_s' \gg \mu_a \tag{4.1}$$

Here, μ_s' is the effective scattering coefficient defined as

$$\mu_s' = (1 - g)\mu_s \tag{4.2}$$

where μ_s is the scattering coefficient and g is the anisotropy factor which takes on the value of 0 for completely isotropic scattering, 1 for perfectly forward directed propagation, and -1 for perfectly backward directed reflection. Although biological tissues typically have g values between 0.7 and 0.9, eq. 4.1 still holds for most turbid tissues. With that approximation, the tissue optical penetration depth ($1/e$ intensity

decay point) can be estimated as [63]

$$\delta = \frac{1}{\sqrt{3\mu_a(\mu_a + \mu_s')}} \tag{4.3}$$

which ranges from 0.5 mm to 4 mm in human tissues for near infrared light [64]. However, this diffusion approximation does not consider the effects of inelastic scattering. It is also not an accurate representation for some tissue types, such as the human skin epidermis, which (unlike the dermis) requires either an exact solution or a numerical simulation [65].

A clever modification to the back-scattered mode geometry was introduced by Matousek et al., where the Raman excitation source and the collection site was separated by a specific distance in order to control the depth from which Raman scattered photons were collected [66]. Termed Spatially Offset Raman Spectroscopy (SORS), this technique uses the fact that the Raman excitation light photons need to travel deeper into the tissue in order for them to emerge at a greater distance away from the site of illumination, which causes a monotonic relationship between the source-detector separation distance and the optically probed tissue depth. By carefully selecting the source and detector separation distance, Raman scattered light collection can be optimized for a specific tissue depth [66]. More recently, Maher and Berger introduced rigorous analytical formulation for optimizing the source-detector distance for the purpose of maximizing the SNR of the desired tissue layer while minimizing that of the interfering tissue layers [67]. This can be tremendously useful for optimizing the Raman excitation and collection geometry for transdermal glucose detection, since the skin, like many other biological tissues, have a layered structure (Fig. 4-1). The outermost skin layer, the epidermis, does not have significant amount of glucose, as it is mainly composed of the stratum corneum (dead skin cell barrier) and keratinocytes which produce the stratum corneum. Beneath the epidermis are the dermis and the subcutaneous tissue, where the cells are bathed in the interstitial fluid that contain glucose. Therefore, for transdermal glucose detection, it would be beneficial to reject the Raman scattered photons arising from the epidermis while accepting those from

the dermis and subcutaneous tissue.

Finally, for thin tissue samples, Raman spectra can be collected in transmission mode. While SORS can be implemented even for thick tissues and offers the ability to reduce the epidermal layer contribution in the collected Raman spectra, it requires a ring-shaped collection geometry in order maximize the collection of Raman scattered light from the same distance away from the illumination site. Since the Raman scattered light needs to travel through the entire thickness of the tissue in order to emerge from the other side, the transmission mode geometry may also provide a similar reduction in the epidermal contribution while preserving or even enhancing the dermal and subcutaneous tissue contribution.[‡] In order to test this hypothesis, a Monte Carlo simulation was performed on a multi-layered skin model representing a thin (1.5 to 5 mm) skin fold (such as the thenar skin fold). Beside elastic scattering, the simulation also incorporated Raman scattering in order to provide a tissue depth profile of Raman scattered photons for both transmission and back-scattered mode. In addition, the tissue thickness, scattering coefficient and the Raman scattering coefficient were varied to observe their effect on the tissue depth profile of Raman scattered photons.

4.2 Estimation of transmitted and back-scattered light power

Before studying the transmission mode Raman spectroscopy in detail, first a simple ray tracing simulation was performed to see how much near infrared (NIR) light power can be transmitted through the thin tissue (Fig. 4-2, Zemax Development Corporation). Using typical skin optical parameters of μ_s=100 cm^{-1}, μ_a=0.3 cm^{-1} and g=0.8 (at 830 nm), three tissue slabs of different thicknesses were each illuminated from one side with a cylindrical beam of light (1 mm diameter). Light detectors were placed both in the front and the back of the tissue in order to measure the power of

[‡]As explained in Chapter 5, transmission mode geometry also offers enhancements in throughput and Rayleigh rejection filter performance.

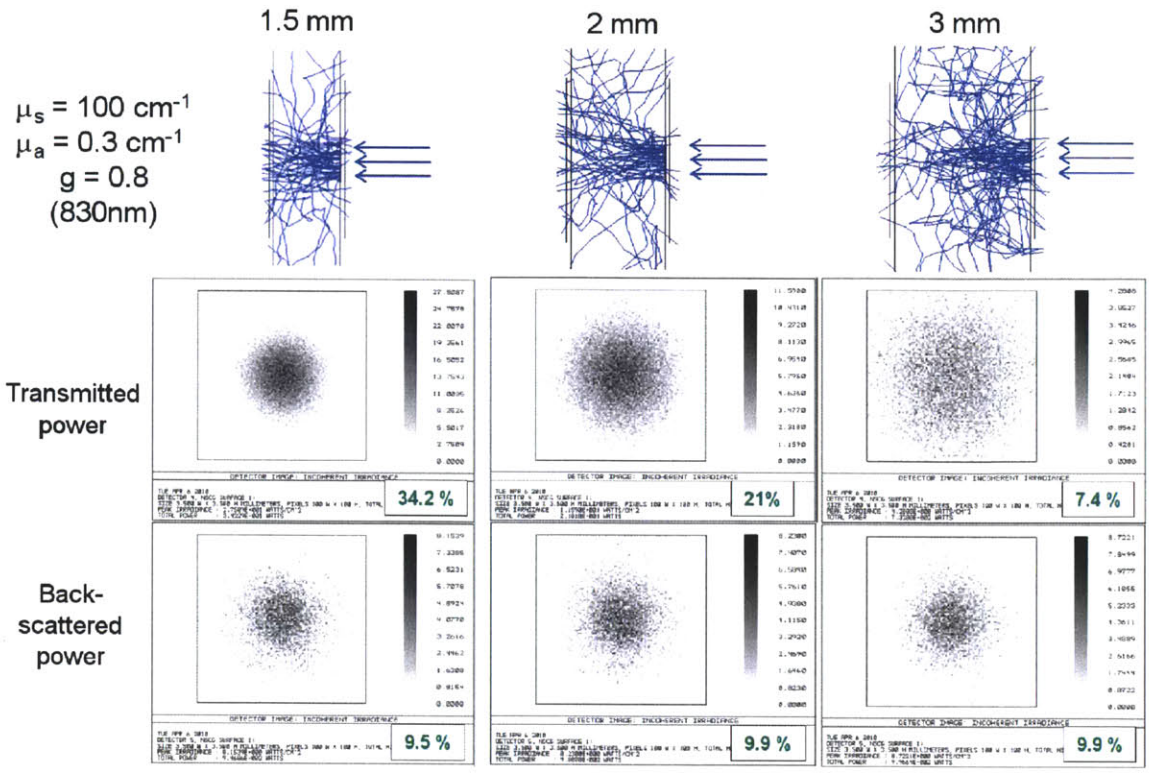

Figure 4-2: Zemax simulations of light transmission and back-scattering in thin skin tissues. Typical skin optical parameters of μ_s=100 cm^{-1}, μ_a=0.3 cm^{-1} and g=0.8 (at 830 nm) were used. A 1 mm-diameter cylindrical beam of laser light (830 nm) was illuminated from the right side of the tissue. A detector was place on the same side as the site of illumination for back-scattered light measurement, while another detector was placed on the other side of the tissue for transmitted power measurement. With the incident light power at 100%, the measured powers are shown as percentages for transmission and back-scattered modes.

near infrared light that was back-scattered from and transmitted through the tissue. As the tissue thickness decreased from 3 mm to 2 mm and 1.5 mm, the transmitted power increased from 7.4% to 21% and 34.2% of the incident light power, respectively (Fig. 4-2). On the other hand, the back-scattered light power changed little at 9.9% for 2 mm and 3 mm tissues, while it decreased to 9.5% for the 1.5 mm tissue. This is because some of the light that would have returned back to the illuminated side in the 2 mm and 3 mm tissues have been transmitted and failed to return in the 1.5 mm tissue. It should be noted that at 3 mm thickness, the transmitted power is still comparable to the back-scattered power, and transmitted power actually exceeds

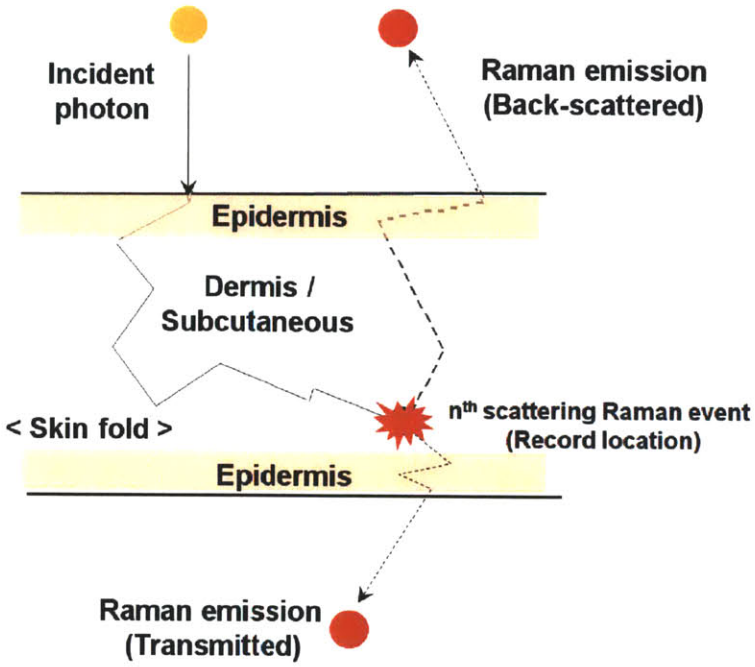

Figure 4-3: Photon migration in skin tissue during a Raman scattering event.

back-scattered power for thicknesses less than 3 mm. (Another research group has successfully performed transmission mode NIR Raman spectroscopy on a 16 mm thick chicken breast tissue to detect calcifications embedded in the middle of the tissue [68, 69].) However, these simulations do not incorporate Raman scattering and therefore do not provide any information about where in the tissues the inelastic scatterings occur. This information could be obtained by performing Monte Carlo simulations described in the next section.

4.3 Monte Carlo simulation of Raman scattering in thin multi-layered skin tissue

The thenar skin fold was chosen to be a candidate for performing transmission Raman spectroscopy for glucose detection, due to its convenient location on the hand, thinness

of the tissue (2~4 mm), and relatively low level of pigmentation.[§] The thenar skin fold can be modeled as a multi-layered tissue structure (Fig. 4-3), which is composed of a thin epidermis on the top and bottom layers, and the dermis/subcutaneous tissue in the middle layer. The well-known multi-layered Monte Carlo simulation ANSI C code developed by Wang et al. [71], was used as a starting point of the model. Since this original code only included absorption and elastic scattering, it was modified to implement Raman scattering. The basic steps of the overall procedure of the Monte Carlo simulation were as follows:

1. Launch Raman excitation photon.

2. In a random manner, with probabilities according to the specified optical parameters, let the photon interact with the tissue by scattering and absorption.

3. For every tissue light scattering, randomly let the photon undergo a Raman scattering with probability as specified by the Raman scattering coefficient.

4. Once a Raman scattering event occurs, record the physical location of the event and continue to track the photon until it exits the tissue or gets absorbed by the tissue.

5. Accumulate two separate records of Raman scattered photons, one for those that were back-scattered toward the illumination source and the other for those that were transmitted through the tissue at the opposite end.

Beside these basic steps, additional routines dealt with the treatment of photon transport near the boundaries among the tissue layers and the air. A more detailed representation of the Monte Carlo simulation procedure is shown in the flow chart of Fig. 4-4. Here, s is the dimensionless step size to be taken by the photon for its next

[§]A previous NIR absorption spectroscopy study had suggested that the tongue would be a better choice over the thenar fold for the noninvasive spectroscopic glucose measurement site [70]. This was based on the fact that the fat tissue in the thenar fold could interfere with the NIR absorption spectroscopy measurement. However, NIR Raman spectroscopy offers superior chemical specificity than NIR absorption spectroscopy, and the tongue tissue is less convenient for implementing transmission geometry.

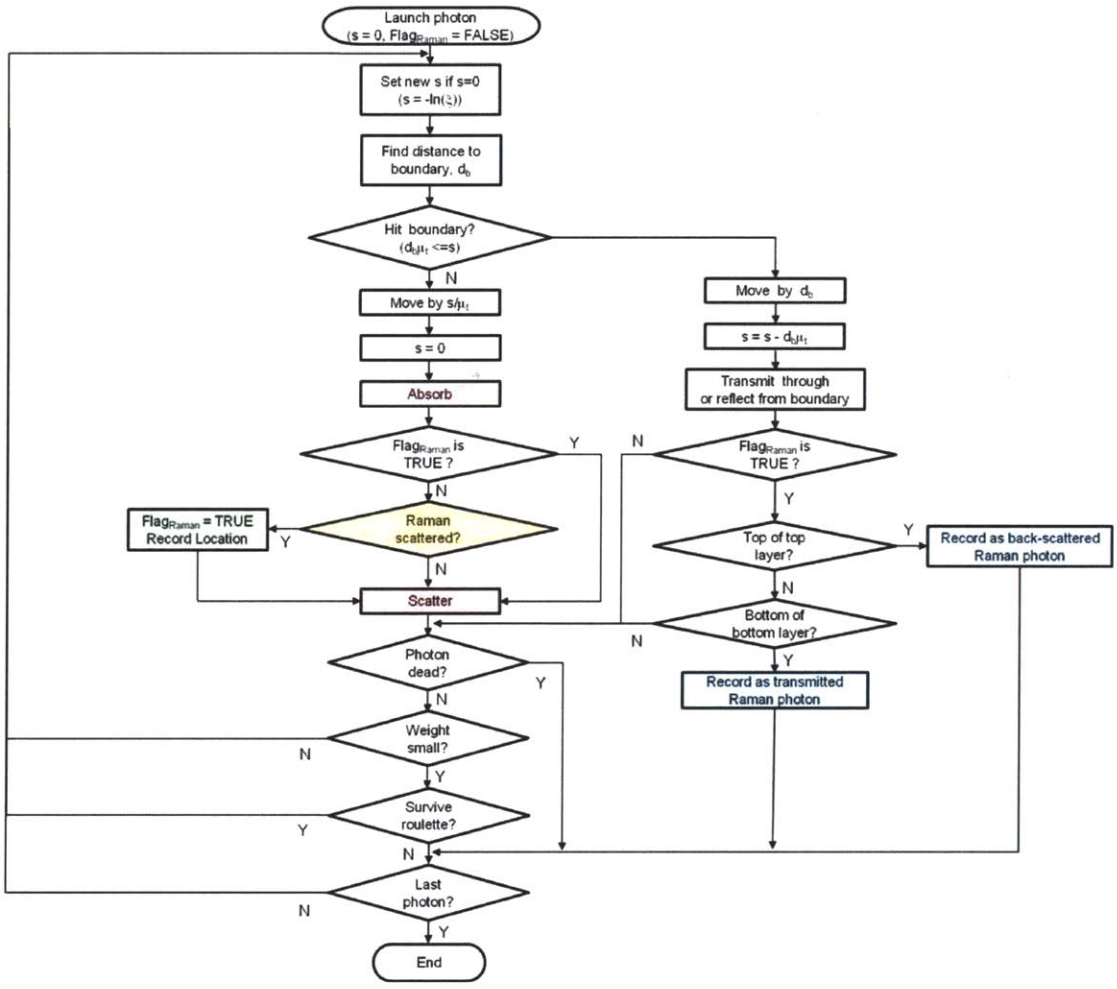

Figure 4-4: Flowchart for Monte Carlo simulation of photon transport and Raman scattering in multi-layered skin tissue.

random movement, which is determined by Beer's law [63]

$$P(s \geq s_1) = \exp(-\mu_t s_1) \tag{4.4}$$

where $\mu_t = \mu_s + \mu_a$.

To accommodate uniform random sampling, the above equation can be represented in terms of a cumulative density function

$$\mathrm{s} = \frac{s_1}{\mu_t} = -\ln \xi \tag{4.5}$$

where ξ was randomly sampled from 0 to 1 in a uniform manner. Similarly, the propagation angle was randomly selected according to the specified anisotropy factor, g, by using the Henyey-Greenstein phase function for bulk tissue scattering. Before the photon hit a boundary delimiting the tissue layer, the distance to the boundary d_b was calculated and subtracted from s so that the remaining step distance could be used for crossing or bouncing away from the boundary.

During this random photon migration, the photon may undergo a Raman scattering event. The probability of such event occurring depended on the value of the Raman scattering coefficient relative to the Rayleigh scattering coefficient : $\frac{\mu_{Raman}}{\mu_{Raman}+\mu_s}$ [72]. Once a Raman scattering event occurred, the boolean flag $\texttt{Flag}_{Raman}$ was set to "TRUE" from the default value of "FALSE" in order to indicate that the photon had undergone a Raman scattering event. At the same time, the location at which this Raman scattering event had occurred was also recorded and the photon was tracked until it met one of the three final fates :

1. Absorbed and "killed" by the tissue.

2. Exit the tissue by back-scattering.

3. Exit the tissue by transmission.

This procedure was repeated in a loop until the specified number of photons to be launched were exhausted. The results of the simulation were two tissue depth profiles

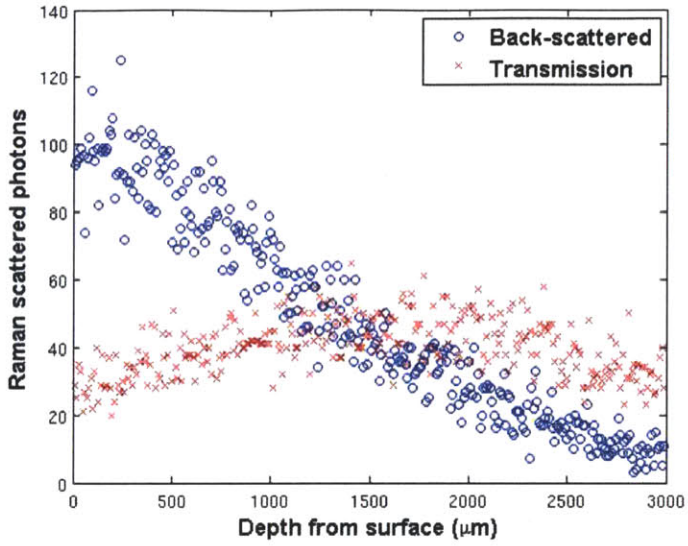

Figure 4-5: Tissue depth profile of the locations of Raman scattering for a typical thenar skin fold of 3 mm thickness, with 0.1 mm-thick epidermal layers on the top and the bottom. The Raman scattered photons collected in back-scattered mode are shown in blue circles while those collected in transmission mode are shown in red x's. ($\mu_{s,epidermis}$=100 cm^{-1}, $\mu_{Raman,epidermis}$=10^{-5} cm^{-1}, $\mu_{a,epidermis}$=0.1 cm^{-1}, $g_{epidermis}$=0.8, $\mu_{s,dermis}$=100 cm^{-1}, $\mu_{Raman,dermis}$=10^{-5} cm^{-1}, $\mu_{a,dermis}$=0.1 cm^{-1}, g_{dermis}=0.8.)

of Raman scattered photons, one collected in back-scattered mode and the other in transmission mode.

4.4 Results and discussion

To simulate a typical human thenar skin fold of 3 mm thickness with 0.1 mm-thick epidermal layers, the following default optical parameters were used: $\mu_{s,epidermis}$=100 cm^{-1}, $\mu_{Raman,epidermis}$=10^{-5} cm^{-1}, $\mu_{a,epidermis}$=0.1 cm^{-1}, $g_{epidermis}$=0.8, $\mu_{s,dermis}$=100 cm^{-1}, $\mu_{Raman,dermis}$=10^{-5} cm^{-1}, $\mu_{a,dermis}$=0.1 cm^{-1}, g_{dermis}=0.8.

Using these default values, Monte Carlo simulation was performed with 2×10^9 photons launched to the tissue illumination site, producing the tissue depth profile of the locations of Raman scattering as shown in Fig. 4-5. In this figure, it can be seen that the Raman scattered photons collected in back-scattered mode form

a very lopsided tissue depth profile, with stronger contributions from the shallower depths. In contrast, the Raman scattered photons collected in transmission mode form a relatively flat and even tissue depth profile, with the strongest contributions coming from the middle of the tissue. This has important implications in transdermal glucose detection, as the epidermal contains little glucose while most of the interstitial fluid glucose is present in the dermal and subcutaneous layers. In the back-scattered mode, having more Raman scattered photons coming from the epidermal layer may cause stronger interfering Raman signatures that could be detrimental to glucose detection. In the following parts of this discussion, simulations were repeated with modified optical and tissue parameters to observe their effects on the tissue Raman depth profiles.

4.4.1 Effect of tissue scattering coefficients

Figure 4-6 shows the effect of the tissue scattering coefficient on the tissue depth profile of the Raman scattered photons. In this figure, the tissues with smaller scattering coefficients had fewer Raman scattered photons, both in the back-scattered and transmission modes. Despite the changes in the scattering coefficients, the general pattern was unchanged: a lopsided back-scattered Raman tissue depth profile with heavier contribution from the outermost layers, and a flat symmetric profile for transmitted Raman photons.

4.4.2 Effect of tissue thickness

In the next set of simulations, the thickness of the skin fold was varied from 3 mm to 4 mm and 5 mm. As shown in Fig. 4-7, increasing the tissue thickness from 3 mm to 4 mm and 5 mm did not change the general qualitative characteristics of the back-scattered and transmitted Raman photon tissue depth profiles. In order to study the results in more detail, Table 4.1 was prepared to show the simulated values of reflectance, transmittance and Raman scattered photons. In this table, the intensity values are in terms of the fraction of the total light delivered to the tissue, which

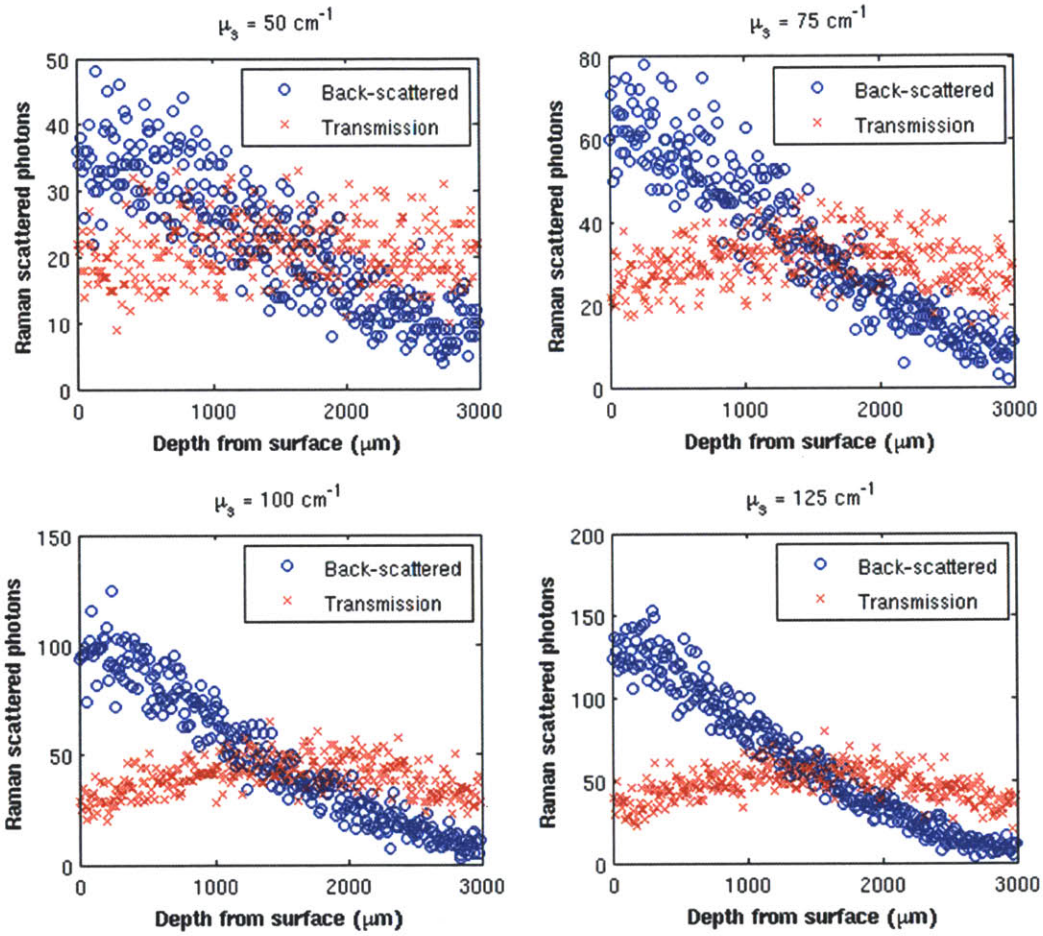

Figure 4-6: Skin tissue fold depth profile of the locations of Raman scattering for different scattering coefficients. The tissue scattering coefficient μ_s was varied from 50 cm^{-1} to 125 cm^{-1}, while μ_{Raman} was assigned a value 10^7 times smaller than the corresponding tissue scattering coefficient.

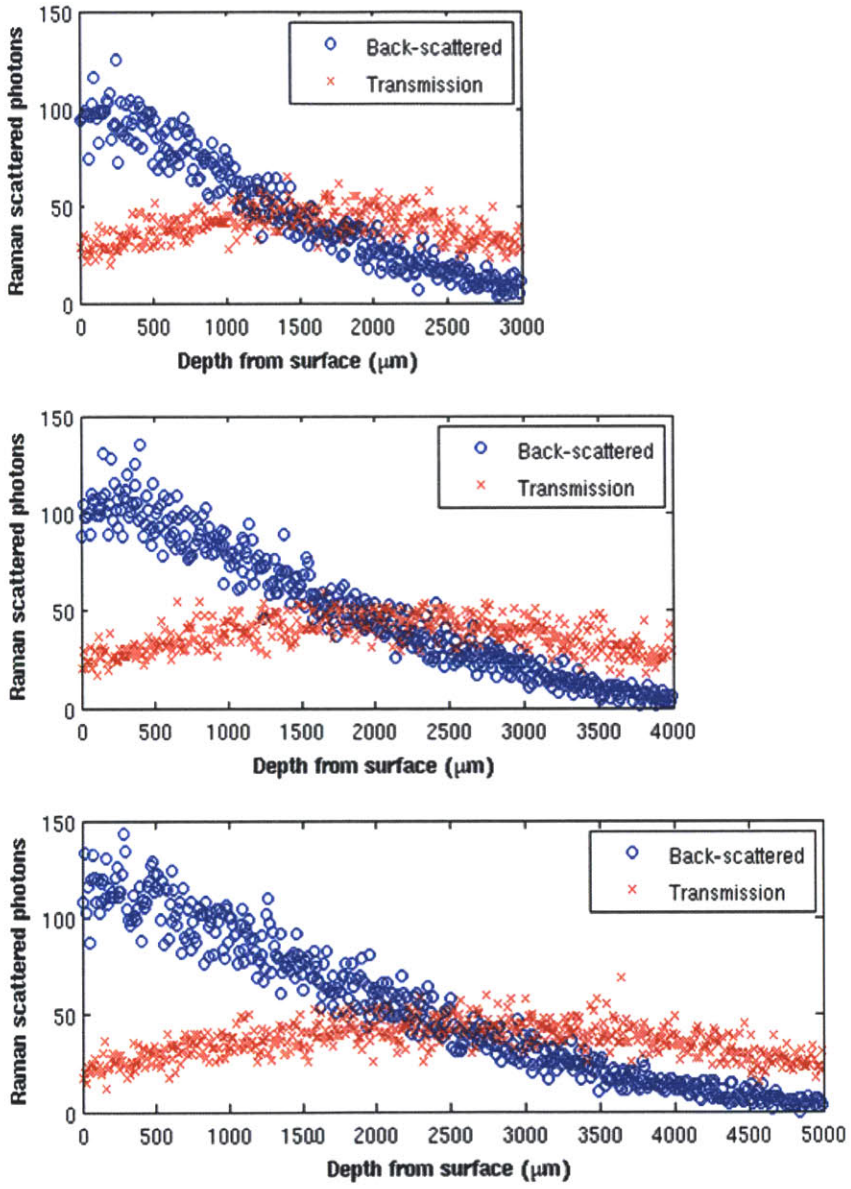

Figure 4-7: Skin tissue fold depth profile of Raman scattering for different tissue thicknesses. With all other parameters kept constant, the tissue thickness was varied from 3 mm to 4 mm and 5 mm.

Table 4.1: Reflectance, transmittance and Raman scattering in tissues with different thicknesses (3 mm, 4 mm and 5 mm).

Thickness (mm)	Specular Reflectance	Diffuse Reflectance	Back-scattered Raman	Raman fraction of Reflectance
3	2.78×10^{-2}	6.17×10^{-1}	7.25×10^{-6}	1.12×10^{-5}
4	2.78×10^{-2}	6.47×10^{-1}	9.97×10^{-6}	1.48×10^{-5}
5	2.78×10^{-2}	6.65×10^{-1}	1.27×10^{-5}	1.84×10^{-5}

Thickness (mm)	Absorbed by tissue	Total Transmittance	Transmitted Raman	Raman fraction of Transmittance
3	1.12×10^{-1}	2.43×10^{-1}	5.98×10^{-6}	2.46×10^{-5}
4	1.42×10^{-1}	1.83×10^{-1}	7.56×10^{-6}	4.13×10^{-5}
5	1.68×10^{-1}	1.40×10^{-1}	9.18×10^{-6}	6.57×10^{-5}

has the value of 1. Therefore, the sum of specular reflectance, diffuse reflectance, total transmittance, and the fraction absorbed by tissue is equal to 1. As expected, varying the tissue thickness did not affect the intensity of specular reflection (Table 4.1). Also, as the tissue thickness increased, the total transmittance decreased while the fraction absorbed by the tissue increased. Interestingly, however, the diffuse reflectance intensity also increased slightly as the tissue thickness increased, due to the fact that less light is lost to transmittance for thicker tissues. As for the Raman scattered photons, both back-scattered and transmitted Raman intensities increased as the tissue thickness increase from 3 to 5 mm, due to the fact that the thicker tissues allowed more opportunities for the photons to undergo Raman scattering. While the back-scattered Raman intensities were similar to the corresponding transmitted Raman intensities (Table 4.1), their relative fraction with respect to the total reflectance and transmittance were different. In Table 4.1, the Raman fraction of reflectance was calculated by dividing the back-scattered Raman intensity by the total reflectance (specular + diffuse). Similarly, the Raman fraction of transmittance was calculated by dividing the transmitted Raman intensity with the total transmittance. When these values were compared, it can be seen that the Raman fraction of transmittance was consistently higher than that of reflectance, and the difference between the two

were greater for thicker tissues. This is due to the fact that:

1. There is no contribution from specular reflectance in the transmitted photons

2. Traveling the entire thickness of the tissue increases the chances of undergoing a Raman scattering event, while the photons collected in back-scattered mode travel through a limited portion of the tissue as defined by the optical sampling volume (hence the higher Raman fraction of transmittance for thicker tissues).

This could be beneficial for Raman spectroscopy instrumentation, since having a greater fraction of Raman scattered photons could provide better rejection of Rayleigh scattered light by the optical filters. However, needless to say, this trend cannot continue indefinitely for much greater thicknesses, since, as the tissue thickness is increased further to become semi-infinite, the back-scattered Raman intensity would remain constant while the transmitted Raman intensity would diminish to zero due to tissue absorption. In order to improve throughput for transmission mode Raman spectroscopy, other researchers have suggested the use of a dielectric filter [73], which forces the light reflected away from the tissue back towards the tissue, in the direction of transmission. A similar concept was tested using a simple ray tracing simulation by placing a reflector on the illuminated side of the tissue, which produced 5% improvement in transmitted Raman scattered light intensity.

4.4.3 Effect of Raman scattering coefficient

Finally, the Raman scattering coefficient μ_{Raman} was varied to observe its effects on the Raman tissue depth profile. In Fig. 4-8, μ_{Raman} was varied from 2×10^{-5} cm^{-1} to 5 cm^{-1} while all other parameters (including $\mu_s = 100$ cm^{-1}) were kept constant. As expected, the number of Raman scattered photons increased with the Raman scattering coefficient. For most values of μ_{Raman}, the Raman tissue depth profile still maintained the qualitative characteristics of having back-scattered Raman photons heavily contributed by the outermost tissues, while the origins of transmitted Raman photons had flatter and more even distribution throughout the tissue depth. However,

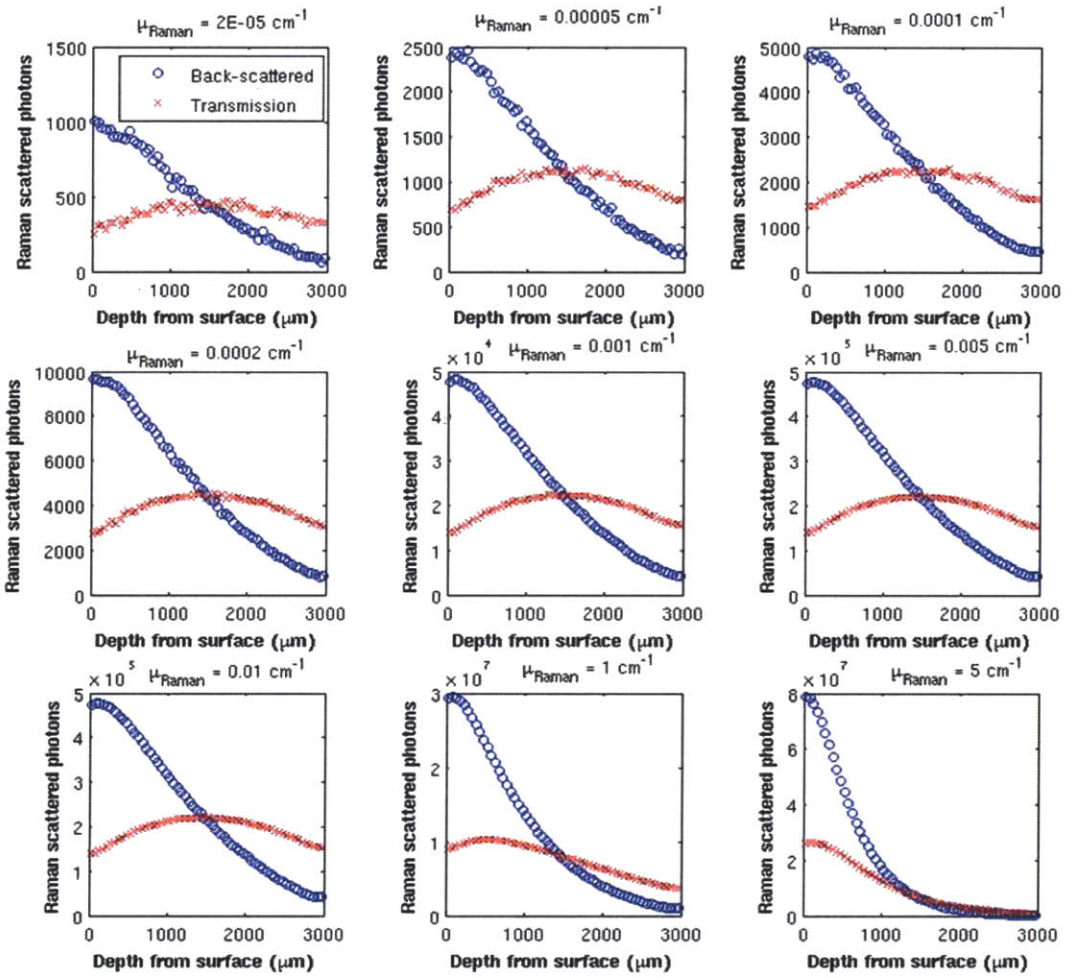

Figure 4-8: Skin tissue fold depth profile of Raman scattering for different Raman scattering coefficients. μ_{Raman} was varied from 2×10^{-5} cm^{-1} to 5 cm^{-1} while all other parameters (including $\mu_s = 100$ cm^{-1}) were kept constant.

this pattern started to break down at μ_{Raman} values higher than 0.01 cm^{-1} (Fig. 4-8). Compared with $\mu_s = 100\ cm^{-1}$, these are unrealistically large values for μ_{Raman}, since spontaneous Raman scattering event typically occurs once every 10^6 $\sim 10^7$ elastic scattering events. (However, the simulation results for these large μ_{Raman} values may be useful for studying other spectroscopic modalities such as fluorescence, which may have much higher probability of excitation than spontaneous Raman scattering.)

4.5 Conclusion

In this chapter, Monte Carlo simulations were employed to study the distribution of Raman scattering events along the depth of a thin skin tissue fold, for both back-scattered mode and transmission mode Raman spectroscopy. The study has shown that Raman scattered photons collected in back-scattered mode have higher contributions from shallower tissue depths, while those collected in transmission mode have a more even and symmetric distribution of contribution along the entire depth of the tissue. This could be beneficial for transdermal glucose detection, since the contribution from the interfering epidermal layer can be reduced. In addition, it has been shown that for the skin tissue fold, the fraction of Raman scattered light is higher in transmission mode than that in back-scattered mode. This could help reduce the amount of Rayleigh scattered light that needs to be removed by the optical filters. In conclusion, collecting Raman spectra in transmission mode for transdermal glucose measurement is not only feasible, but also accompanies several advantages over conventional back-scattered mode collection.

THIS PAGE INTENTIONALLY LEFT BLANK

Chapter 5

Development of clinical Raman spectroscopy instrument

5.1 Introduction

With the exception of a few transparent tissues such as the ocular lens, most bulk biological tissues are highly scattering even in the near infrared (NIR) regime. On the other hand, many optical systems can receive light only at a limited range of angles specified by their effective numerical apertures. This is particularly problematic for designing a suitable Raman spectroscopy-based diagnostic device, as efficient light collection is crucial due to the inherently weak nature of Raman scattered light. For this reason, Raman spectroscopy instruments used for the analysis of bulk biological tissues often require a light collection device that redirects the light scattered at steep angles to be collimated within a limited range of conic half angles with respect to the receiving optical system. This had been previously achieved by the use of a half paraboloidal mirror [57], plano-convex lens [74], sapphire ball lens [75, 76], and a compound parabolic concentrator (CPC) [77, 76]. However, many of these strategies have certain shortcomings. For example, while Raman scattered photons can back-scatter in all directions when the excitation light impinges on the tissue surface (due to the sequence of multiple scattering events in the tissue), the half paraboloidal mirror surrounds only a portion of the illuminated tissue surface and fails to collimate the

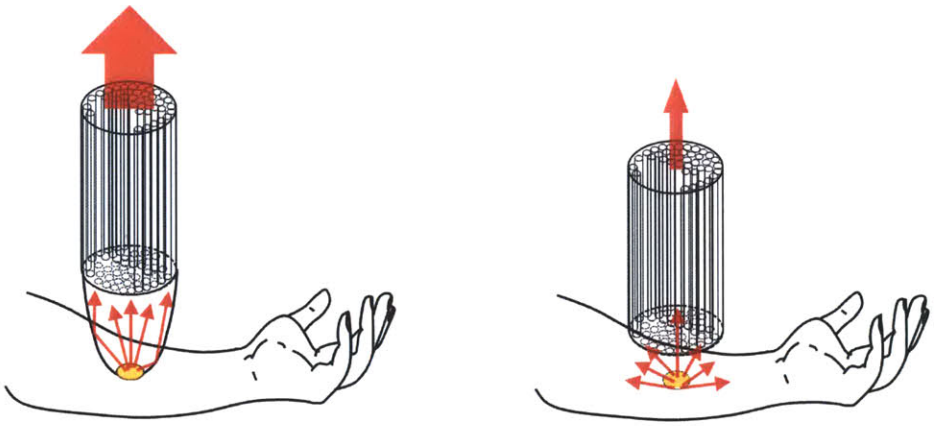

Figure 5-1: Compound parabolic concentrator (CPC) coupled to an optical fiber bundle for enhanced Raman light collection.

light being scattered away from the mirror. The plano-convex collimation lens has a limited acceptance angle defined by its numerical aperture. Finally, the sapphire ball lens itself could create significant Raman signals and confound the intrinsic tissue Raman spectra.

All of these issues mentioned above can be resolved by using a hollow gold-coated CPC. A CPC completely surrounds the illuminated tissue site (360°) to efficiently collect Raman scattered light at all conic half angles (−90° to 90°). In addition, the gold-coated surface efficiently reflects the NIR Raman scattered light without generating Raman signatures of its own. This chapter describes a portable clinical Raman spectroscopy instrument that has been designed to incorporate a CPC-based optical fiber probe. The CPC was designed using ray-tracing simulations and manufactured using computer-controlled machining and electroforming techniques. The performance of the CPC was tested to show a significant enhancement in Raman scattered light collection.

5.2 The compound parabolic concentrator

However, the utility of CPC is limited when a very high degree of light collimation is desired, as its physical dimensions become impractically large for manufacturing or

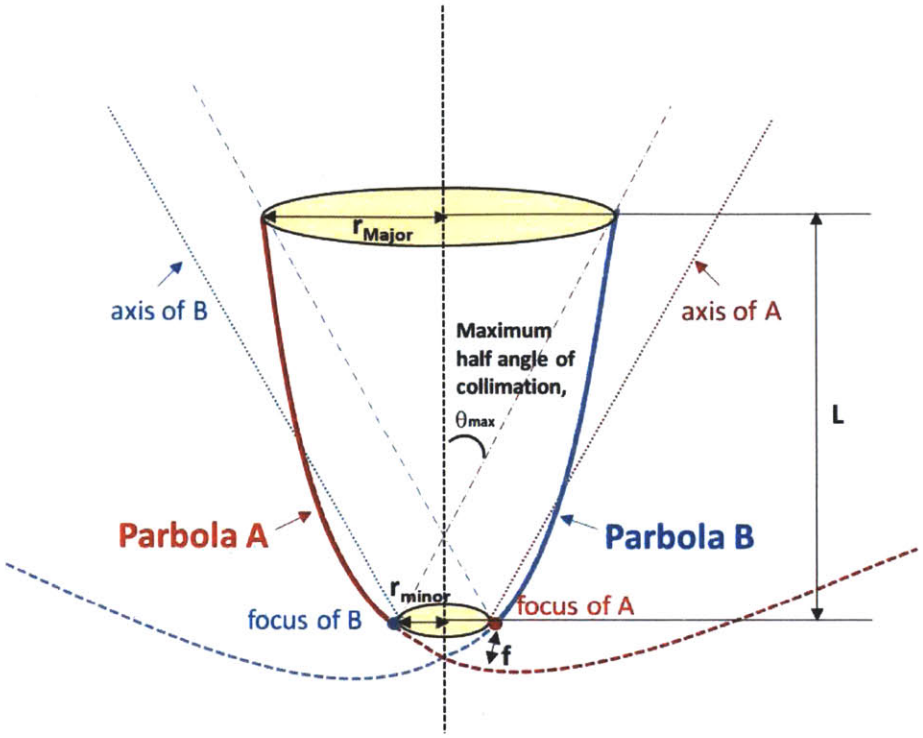

Figure 5-2: Compound parabolic concentrator (CPC).

use. In order to circumvent this problem, the portable clinical Raman spectroscopy instrument was also designed to incorporate a non-imaging optical element called compound hyperbolic concentrator (CHC). Unlike the CPC, the CHC coupled with a matching lens allows the instrument to efficiently collect Raman spectra from highly scattering biological tissues by collimating the Raman scattered light within a very narrow range of half angles, while also maintaining much smaller physical dimensions than a CPC.

5.3 The compound parabolic concentrator

The compound parabolic concentrator (CPC) is a non-imaging optical element formed by the revolution of two tilted and offset parabolae (Fig. 5-2). It has two apertures: a minor aperture defined by the two parabolic foci, and a major aperture at the other end. The smaller aperture can accept light rays at all angles (half angles -90° to 90°),

while the larger aperture can only accept light rays entering at a limited range of angles, as defined by the angle between the parabolic axes (Fig. 5-2). Depending on its application, either CPC aperture can serve as the light input while the other aperture is used as the output. Originally, the CPC was designed to accept sun rays from the major aperture while concentrating the light through the minor aperture for efficient solar energy collection [78]. Conversely, such as in light emitting diode illuminators [79], the minor aperture can be used as the input to collect light scattered at all angles (half angles -90° to 90°), while collimating the light at the output (major) aperture to be within a limited range of angles. It should be noted, however, that when used as a collimator, the CPC does not conserve the étendue. In order to conserve the étendue, the two apertures must satisfy the following

$$S_1\Omega_1 = S_2\Omega_2 \tag{5.1}$$

where S denotes the aperture area and Ω is the solid angle. For circular areas and conic angles ($\Omega = 2\pi\,(1-\cos\theta)$=$4\pi\sin^2\left(\frac{\theta}{2}\right)$), this becomes

$$4\pi r_1^2 \sin^2\left(\frac{\theta_1}{2}\right) = 4\pi r_2^2 \sin^2\left(\frac{\theta_2}{2}\right)) \tag{5.2}$$

which simplifies to

$$\frac{r_2}{r_1} = \frac{\sin\left(\theta_1/2\right)}{\sin\left(\theta_2/2\right)} \tag{5.3}$$

Since a CPC accepts 2π solid angle at the minor aperture, the étendue matching equation becomes

$$\frac{r_{Major}}{r_{minor}} = \frac{\left(1/\sqrt{2}\right)}{\sin\left(\theta_{max}/2\right)} = \frac{0.707}{\sin\left(\theta_{max}/2\right)} \tag{5.4}$$

where θ_{max} is the maximum half angle of collimation. However, for a CPC, the étendue at the major aperture is smaller than that of the minor aperture, due to the following relationship of the CPC apertures

$$\frac{r_{Major}}{r_{minor}} = \frac{1}{\sin\theta_{max}} \leq \frac{0.707}{\sin\left(\theta_{max}/2\right)} \tag{5.5}$$

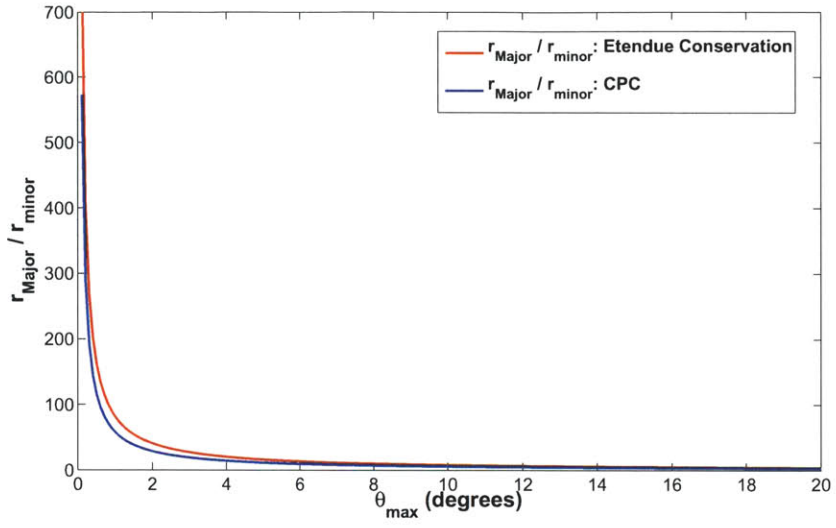

Figure 5-3: $\frac{r_{Major}}{r_{minor}}$ for étendue conservation and CPC.

This can be visualized in Fig. 5-3 and Fig. 5-4, which suggest that the étendue is conserved when the rays enter from the major aperture, while it is not conserved when the rays enter from the minor aperture.

Despite these limitations when used as a collimator, the CPC can still provide a significant enhancement in the collection of Raman light scattered from turbid tissues, by accommodating the limited numerical aperture of the collecting optical system [77]. This is illustrated in Fig. 5-5, which shows the results of ray-tracing simulations (Zemax Development Corporation) comparing different types of reflectors. In each simulation, an isotropically scattering light source (0.8 mm diameter, matched to the size of the reflector aperture) is placed on the left of the reflector while a detector with a limited range of acceptance angles (12.7° or less) is placed on the right. Without any reflector, only 6% of the light was detected, while 74% of the light was detected with a conical reflector. With a paraboloidal reflector, which appears to be similar to CPC, still collected only 75%. However, with a CPC, 97% of the light was detected, demonstrating that the CPC performance cannot be matched by a similarly shaped paraboloid.

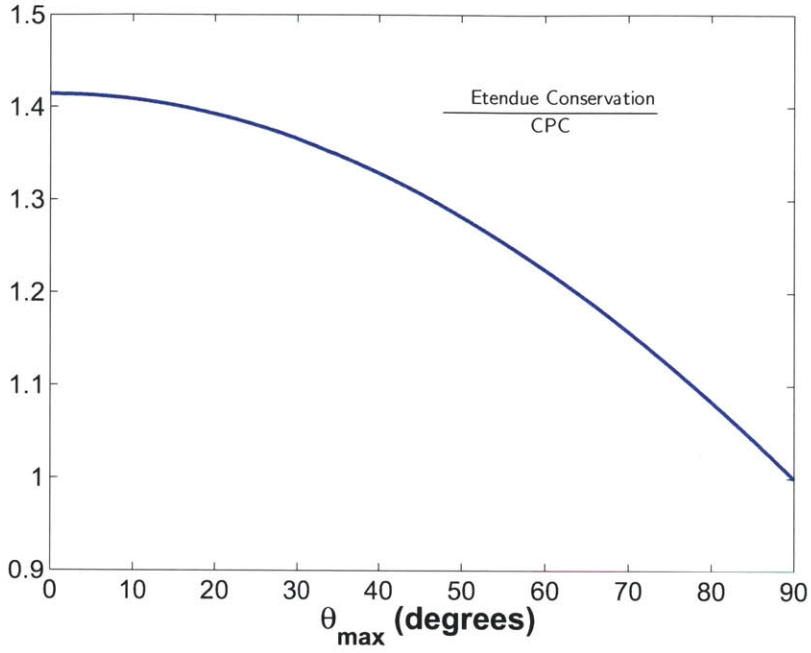

Figure 5-4: Ratio of quantities described in Fig. 5-3.

5.3.1 Designing the CPC

As shown in Fig. 5-2, the main CPC design parameters include the minor aperture radius r_{minor}, the major aperture radius r_{Major}, and the maximum half angle of collimation θ_{max}. From these parameters, the overall dimensions of the CPC are determined. The focal length, f, of the parabolae is defined as [80, 81]:

$$f = \frac{r_{minor}}{1 + \sin\theta_{max}} \tag{5.6}$$

and the overall CPC length, L, is defined as:

$$L = \frac{r_{minor}\,(1 + \sin\theta_{max})}{\tan\theta_{max}\sin\theta_{max}} \tag{5.7}$$

Finally, the major and minor aperture radii are related as follows:

$$r_{Major} = \frac{r_{minor}}{\sin\theta_{max}} \tag{5.8}$$

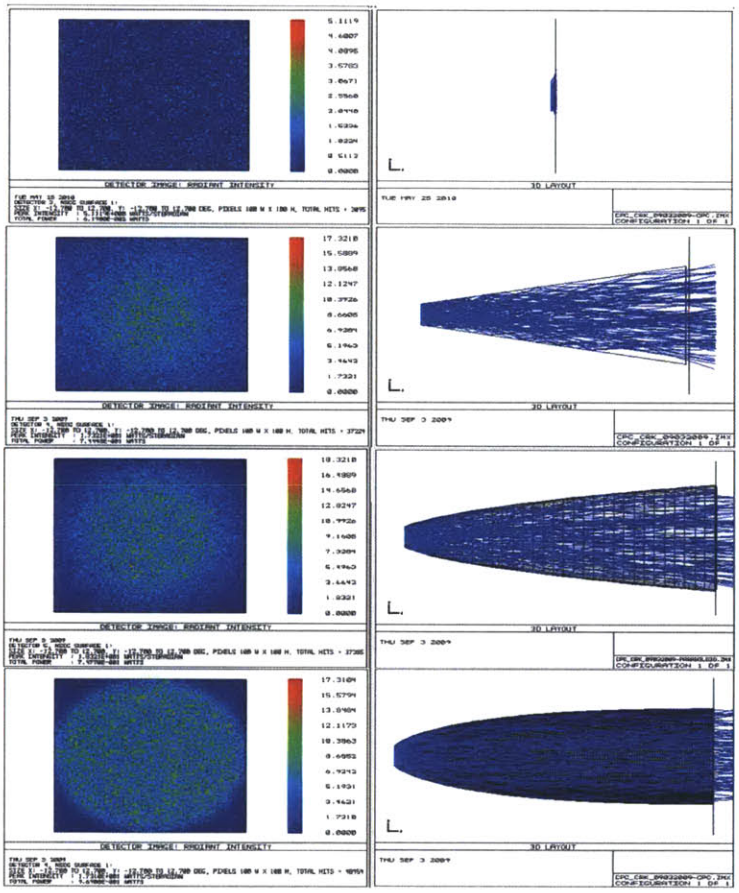

No reflector (r=0.4mm)
Collection Efficiency
12.7 deg : 6%

Cone (r=0.4mm)
Collection Efficiency
12.7 deg : 74%

Paraboloid (r = 0.4 mm)
Collection Efficiency
12.7 deg : 75%

CPC (r = 0.4mm)
Collection Efficiency
12.7 deg : **97%**

Figure 5-5: Comparison of collection performance in different reflectors.

When designing the CPC for tissue Raman spectroscopy, the major aperture radius r_{Major} is typically constrained by the requirements of the receiving optical system. For example, if the CPC is used for enhancing light collection by an optical fiber bundle coupled to a spectrograph and a CCD detector, r_{Major} is limited by the maximum slit height permitted by the spectrograph-CCD system. With this constraint, the remaining two parameters, r_{minor} and θ_{max} can be optimized.

When the Raman excitation light impinges on a single point on the turbid tissue surface (e.g. skin), it undergoes diffuse scattering and spreads throughout the tissue volume. Therefore, in order to maximize throughput, Raman scattered light should be collected from an area much larger than the illuminated spot on the tissue surface. Since the CPC cannot collect the light beyond the limits of its input aperture, a greater input aperture size is desirable to permit as many photons as possible. However, in order to increase r_{minor}, the maximum angle of collimation θ_{max} would also have to be increased, which cannot be done indefinitely as the optical system has a limited numerical aperture. Although θ_{max} could be set equal to the system numerical aperture, it may not be optimal as a larger r_{minor} at the expense of θ_{max} greater than the system numerical aperture could provide an overall gain in throughput. To arrive at the optimal trade-off, a ray-tracing ZEMAX simulation was performed at various combinations of r_{minor} and θ_{max}. In Fig. 5-6, it can be seen that as r_{minor} was increased beyond the value obtained by setting θ_{max} equal to the system numerical aperture (r_{minor}=0.4 mm), the collected light power also increased until it reached a maximum, beyond which θ_{max} became too much greater than the limit of the system numerical aperture and the collected light power started to decrease.

5.4 The compound hyperbolic concentrator

5.4.1 Advantage of CHC over CPC

As mentioned previously, the CPC can be used as a collimator by using its minor aperture as input. Tanaka et al. proposed the use of a hollow gold-coated CPC as a

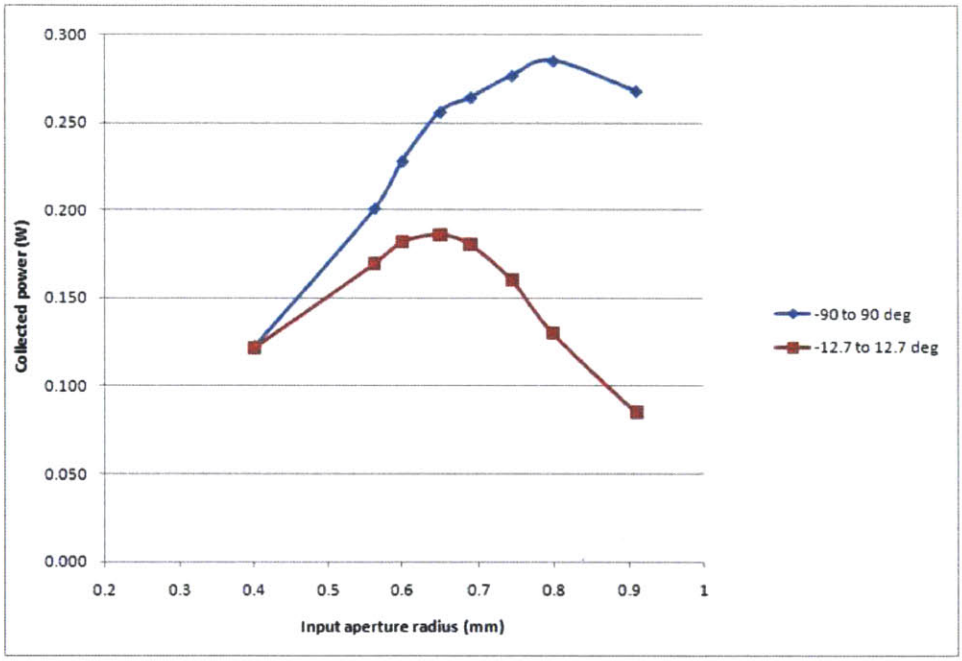

Figure 5-6: Optimization of CPC input aperture radius. Using Zemax ray-tracing simulations, the power of light collected within $\pm 90°$ and $\pm 12.7°$ were monitored while the input aperture radius r_{minor} was increased from 0.4 mm to 0.9 mm. At the same time, θ_{max} was also varied accordingly to maintain a constant output aperture radius of $r_{Major} = 1.8$ mm.

collimator to facilitate Raman scattered light collection from biological tissues by an optical fiber probe with a limited numerical aperture (0.29 NA), and demonstrated seven-fold enhancement in collection efficiency compared with the same optical fiber probe without the CPC [77]. However, many bulk tissue Raman spectroscopy systems call for an even higher degree of collimation than required by the numerical aperture of the collection optical fibers and spectrographs, as certain dielectric and holographic optical filters are effective only at a very limited range of incident angles. For example, both the optical density as well as the band center of the holographic notch filter varies significantly with the angle of the incident beam [82, 83]. While this property is very useful when filtering collimated beams, as it allows fine adjustment of the stopband wavelengths by angle tuning [82, 83], it could significantly reduce the filter performance when collecting photons that are multiply-scattered in a wide range of angles. This has important implications in bulk biological tissue Raman spectroscopy as most bulk tissue samples are highly scattering and Rayleigh scattered light needs to be filtered out efficiently in order to obtain a Raman spectrum of acceptable quality.

Although a CPC can be designed to achieve a very high degree of collimation to facilitate good filter performance, it would require very large physical dimensions relative to a given input aperture size. For a given input aperture r_{minor} and the maximum collimation half angle θ_{max}, the length of the CPC, L, is defined by eq. 5.7. When this equation is plotted, as shown in Fig. 5-7, the length of the CPC rapidly becomes very long and approaches infinity as the desired maximum collimation half angle gets closer to zero degrees. However, the required length of the nonimaging optical element can be significantly reduced by introducing the CHC (Fig. 5-8).

Unlike the CPC, whose reflector surface is defined by rotating the curve formed by two tilted and offset parabolae [77], the CHC is defined as a surface of revolution whose cross sectional profile is defined by two hyperbolae that are mirror images about the horizontal axis (Fig. 5-9(A)) [81]. In addition to the reflector itself, the CHC also requires a matching focusing lens with the focal length defined by the distance between the output aperture and the focus on the opposite side of the symmetric axis of the hyperbola (Fig. 5-9(A)). This combination effectively allows the CHC to

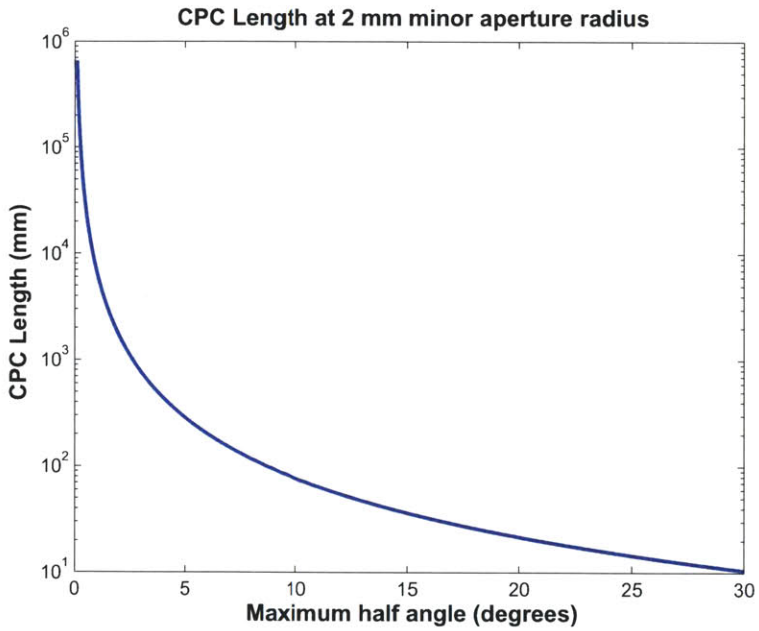

Figure 5-7: CPC lengths with respect to maximum collimation conic half angles for input aperture radius of 2 mm. Maximum half angle of zero degrees corresponds to perfect collimation.

function as a CPC with much larger dimensions (Fig. 5-8(B)). In Fig. 5-8(A), both the CPC and the CHC have an input aperture diameter of 4 mm, and are capable of converting the input light directions from half angles as wide as $\pm 90°$ to $\pm 3.9°$ or less. However, the CPC length is 460 mm while the CHC length is only 115 mm. The CHC can achieve the same effect as a very long CPC while also maintaining much smaller physical dimensions by using a lens that has its focus point at the opposite hyperbolic focus (Fig. 5-9(A)). As shown in Fig. 5-8(B), due to the hyperbolic shape of the reflector, the light is redirected in a manner such that light emanating from point I at the input aperture of the CHC acts as if it were coming from point II, which lies on the lens' focal plane.

5.4.2 Designing the CHC

The input aperture radius R_i of the CHC was defined by the distance between the horizontal axis and the focus f_{1B} (or f_{1A}) of the hyperbola (Fig. 5-9). As mentioned

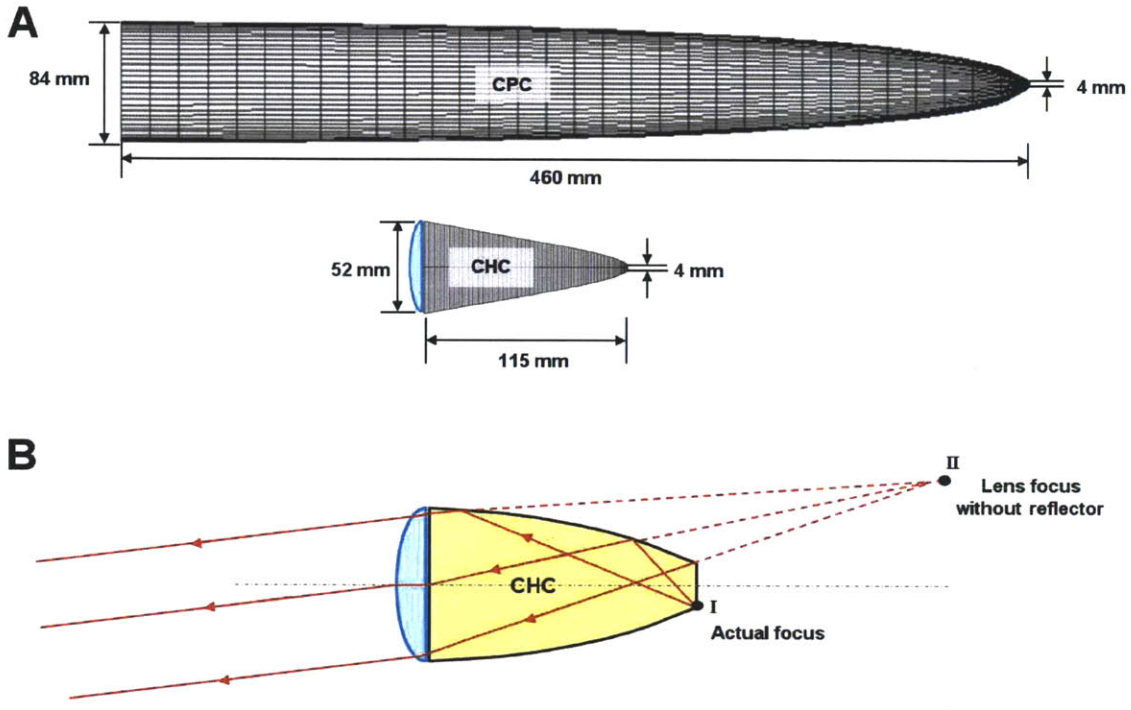

Figure 5-8: (A) Comparison of CPC and CHC with the same input aperture size and degree of collimation. Both CPC and CHC have input aperture radius of 2 mm and maximum collimation half angle of 3.9°. (B) The CHC functions as a CPC of much greater length with the help of a matching focusing lens. Due to the hyperbolic shape of the reflector, light emanating from point I (the actual focus of the lens) are collimated by the lens as if it were coming from point II.

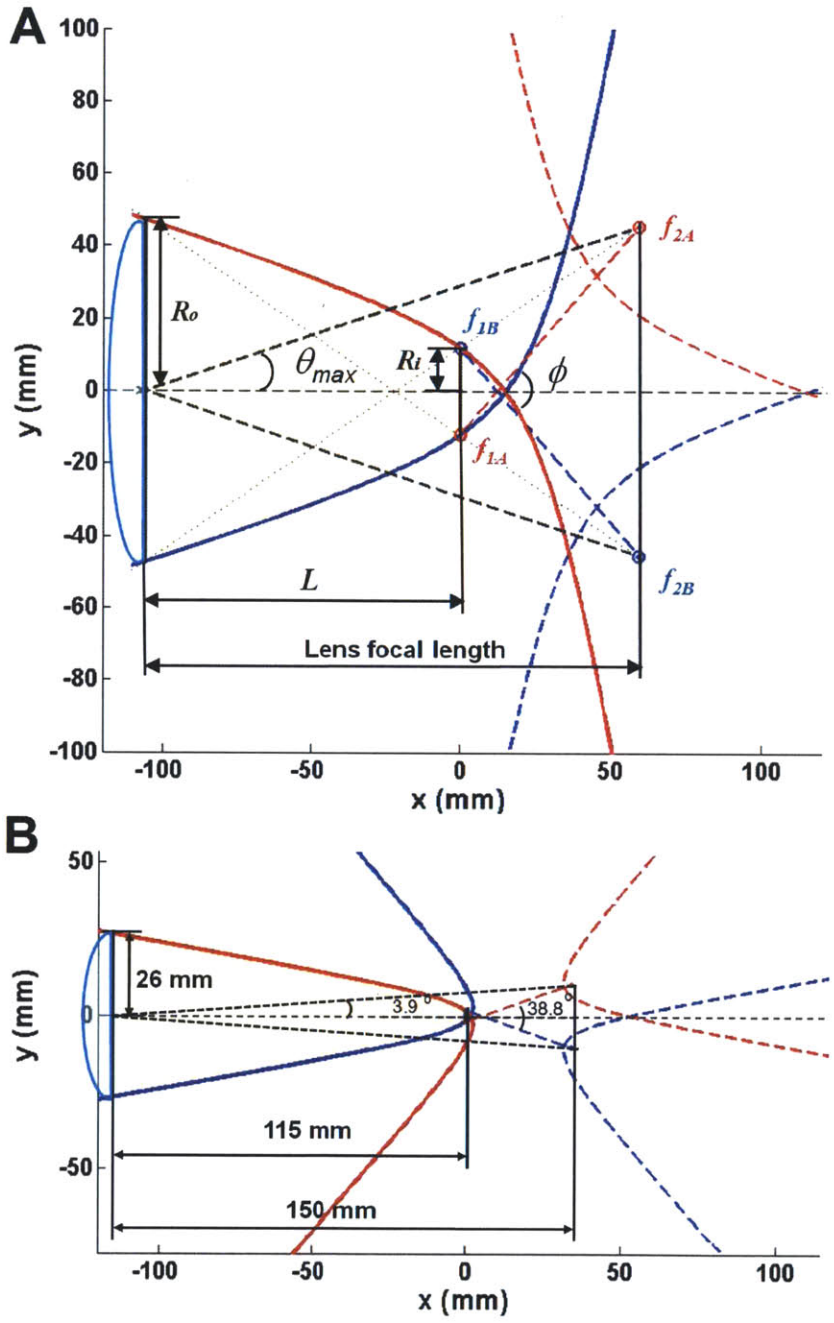

Figure 5-9: (A) CHC formed by two hyperbolae and its associated design parameters. R_i: input aperture radius, R_o: output aperture radius, L: CHC length, θ_{max}: maximum collimation conic half angle, ϕ: angle between the two hyperbolae, f_{1A}, f_{2A}, f_{1B}, f_{2B}: foci of hyperbolae. The diameter and focal length of the matching plano-convex focusing lens are clearly defined by R_o and the distance between the output aperture and the hyperbolic foci (f_{2A} and f_{2B}). (B) CHC design optimized for the clinical Raman instrument.

previously, for transdermal glucose detection, it is desirable to have a large input aperture radius in order to accept as many Raman scattered photons as possible (unlike imaging applications that require high spatial resolution). The major (output) aperture radius R_o was defined by the distance between the horizontal axis and the intersection of the hyperbola and the line connecting the foci f_{1A} and f_{2B} (or, f_{1B} and f_{2A}). This dimension was constrained by the largest available lens with a focal length equal to the distance between the output aperture and the line connecting the foci f_{2A} and f_{2B}. Finally, the maximum half angle θ_{max} of collimated light was defined by the angle between the horizontal axis and the line connecting the center of the output aperture to the focus f_{2A} (or f_{2B}). Since the CHC was to be placed in front of a holographic notch filter designed to accept a collimated beam, θ_{max} was minimized for optimization.

With these constraints, the adjustable parameters included the angle ϕ between the transverse axes of the two hyperbolae (Fig. 5-9), and the shape of the hyperbolae as defined by A and B of the hyperbolic equation:

$$\frac{x^2}{A^2} - \frac{y^2}{B^2} = 1 \tag{5.9}$$

The final result of the optimization was a CHC with 2 mm input radius, 26 mm output radius, length of 115 mm, and θ_{max} of 3.9° (Fig. 5-9(B)).

5.5 Manufacturing the CPC and CHC

Identical procedures were used for manufacturing the CPC and the CHC. The optimized design was first verified for performance by using ray-tracing simulations (Fig. 5-10, ZEMAX Development Corporation) and transferred to a computer-aided manufacturing program (Mastercam, CNC Software, Inc.). Using a computer numerical control (CNC) lathe machine (HAAS Automation, Inc.), an aluminum mandrel of the CHC was manufactured to high accuracy (error less than 5 μm) and polished to optical grade fineness (0.1 μm) (Fig. 5-11).

The mandrel was then deposited with a layer of nickel by using a nickel sulfamate

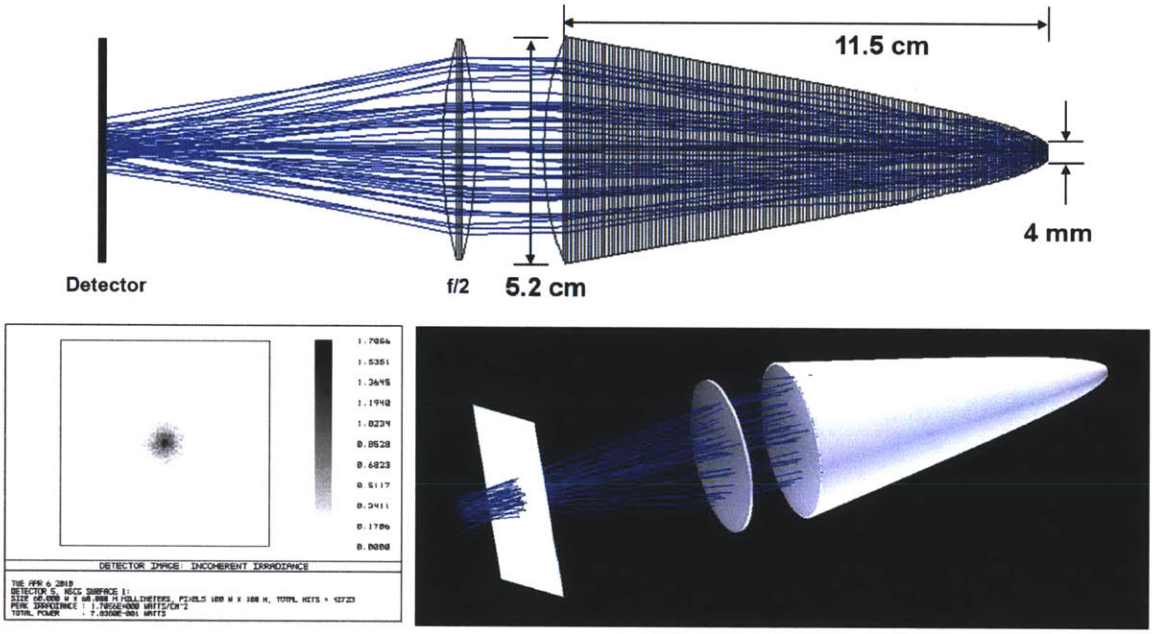

Figure 5-10: ZEMAX ray-tracing simulation for design verification. The optimized CHC design of Fig. 5-9B was imported into ZEMAX, and coupled with a matching plano-convex focusing lens of 150 mm focal length. Another focusing lens of f/2 was placed in front of the CHC output aperture, and a detector was placed near its focus. In order to simulate the limited numerical aperture (f/2) of the collection fiber bundle (Fig. 5-13), the detector only accepted light coming in at conic half angles of $\pm 14°$ or less. With an isotropic light source (conic half angle $\pm 90°$ or less) at the CHC input aperture, the detector received 78% of the original light intensity.

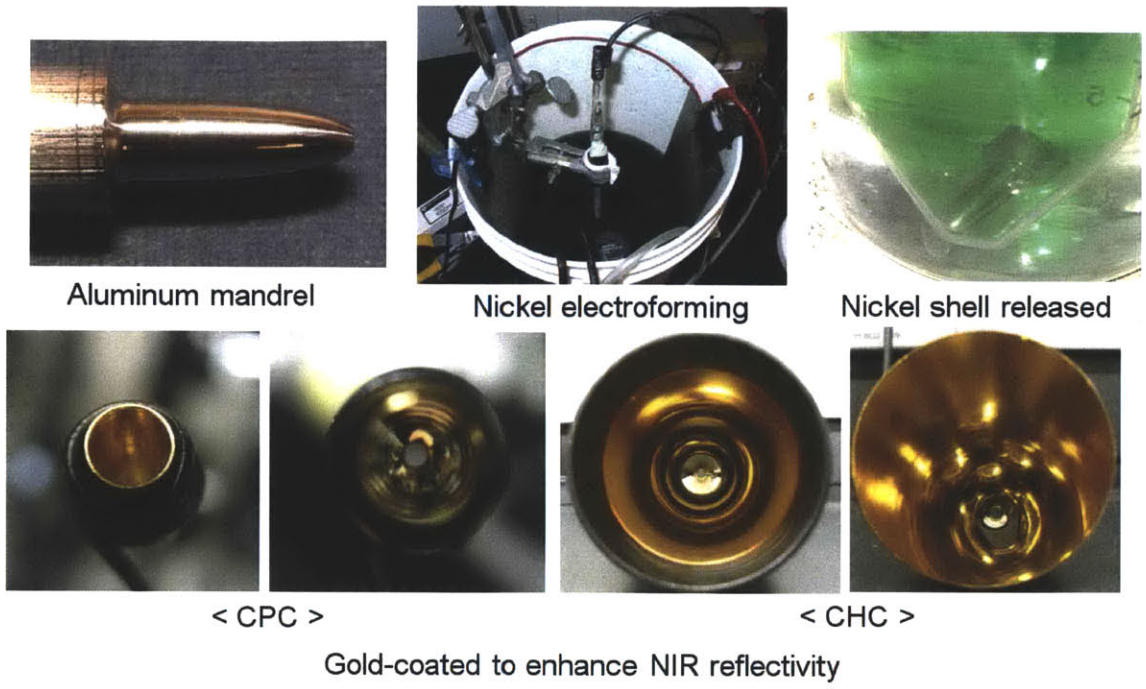

Figure 5-11: Manufacturing the CPC and CHC.

electroforming process (Caswell, Inc.). The mandrel was then released by dissolving the aluminum in a warm (40°C) sodium hydroxide solution while leaving the nickel intact to create the hollow nickel CPC and CHC shells. After an electroless bright nickel electroplating process [84] for enhanced reflectivity and secondary polishing to optical grade fineness (0.1 μm), the CPC and CHC were electroplated with a uniform layer of pure gold (99.9%) in order to improve NIR reflectivity (>98% at 830 nm) (Figs. 5-11).

Figure 5-12 describes a test for the performance of the manufactured CPC. An 830 nm laser light was illuminated on the quartz cuvette holding a powder sample of acetaminophen. On the other side of the sample, a CPC-equipped optical fiber probe was placed to collect the Raman spectrum. Then another Raman spectrum was collected with the same optical fiber probe and aperture, but without the CPC. Tanaka et al. derived the CPC enhancement factor (ρ) by forming the radiance intensity ratios [77]:

$$\rho = \frac{\int_{\varphi=0}^{2\pi} \int_{\theta=0}^{\pi/2} L(\theta,\varphi) \sin\theta \mathrm{d}\theta \mathrm{d}\varphi}{\int_{\varphi=0}^{2\pi} \int_{\theta=0}^{\theta_{max}} L(\theta,\varphi) \sin\theta \mathrm{d}\theta \mathrm{d}\varphi} \tag{5.10}$$

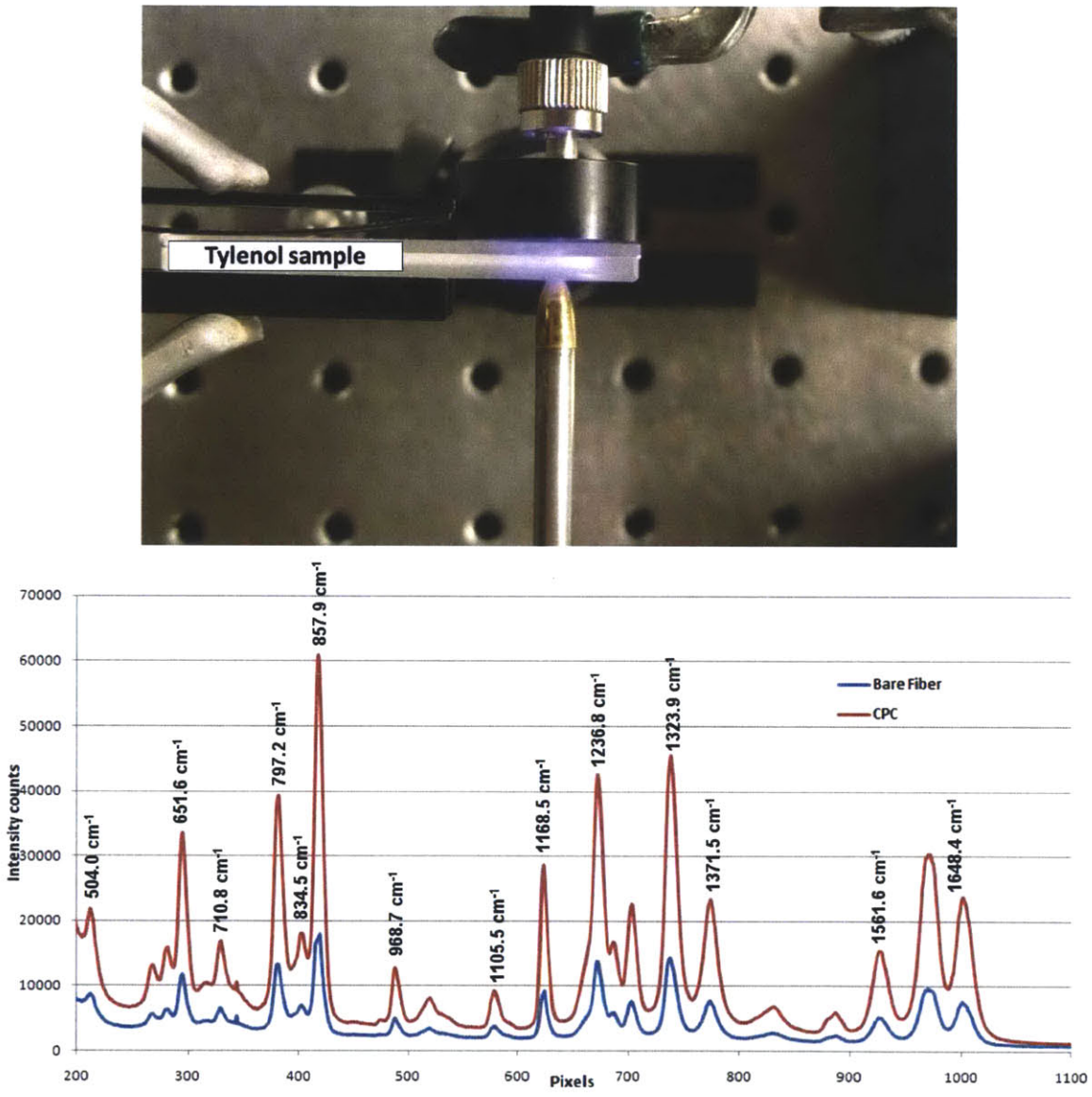

Figure 5-12: Testing the performance of CPC. Top: An 830 nm laser light was illuminated from the top, onto the quartz cuvette holding a powder sample of acetaminophen ("Tylenol"). On the other side of cuvette, a CPC-based optical fiber probe was placed to collect the Raman spectrum of the sample. Bottom: Raman spectra collected by the optical fiber probe with the CPC (red) and without the CPC through an equally sized aperture (blue).

where numerator describes the radiance at the minor aperture and the denominator describes that of the major aperture. For highly turbid media such as biological tissues, the Raman scattered light distribution is Lambertian, with $L(\theta, \varphi) = L_o \cos\theta$. This makes the enhancement factor to be

$$\rho = \frac{2}{(1 - \cos 2\theta_{max})} = \frac{2}{(1 - \cos 25.4^o)} = 20.7 \tag{5.11}$$

However, this formulation ignores the étendue conservation. As shown in section 5.3, the étendue of the CPC is not conserved when the minor aperture is used as input (although this effect is pronounced only at very small maximum half angles (θ_{max})). By incorporating the étendue factor of eq. 5.5, the enhancement ratio then becomes

$$\rho = \frac{2}{(1 - \cos 2\theta_{max})} \frac{\sin(\theta_{max}/2)}{0.707 \sin(\theta_{max})} = \frac{2}{(1 - \cos 25.4^o)} \frac{\sin(6.35^o)}{0.707 \sin(12.7^o)} = 14.7 \tag{5.12}$$

As shown in Fig. 5-12, the CPC enhanced the Raman spectral peak intensities by about four times, in contrast to the theoretically possible enhancement of 14.7 times. This may be due to two possible reasons:

1. Shape deviation due to errors in machining.

2. Imperfections in mirror polishing (0.1 μm).

Ray-tracing simulations performed by Tanaka et al. showed less than 20% reduction in throughput for 1% shape deviation [77]. As the CNC lathe machine has a very high accuracy (error less than 5 μm) relative to the dimensions of the CPC and CHC (errors are in the range of 0.1 to 0.01%), the major contributor to the performance degradation may be the reduced reflectivity due to imperfections in mirror polishing. To analyze the effect of surface roughness on reflectivity, the Rayleigh criterion can be expressed as

$$\Delta\phi = \frac{4\pi h \cos\gamma}{\lambda} \tag{5.13}$$

where h is the height of the imperfections on the mirror surface γ is the incident angle of the light beam and λ is the light wavelength. Since $\Delta\phi = \pi$ gives destructive

interference, an approximate condition for optical gloss can be set as

$$\Delta\phi < \frac{\pi}{2} \tag{5.14}$$

which translates to

$$h < \frac{\lambda}{8\cos\gamma} \tag{5.15}$$

At 830 nm, this sets the upper limit of h to 0.1 μm, which is barely matched by the grit size used in the mirror polishing. Therefore, further improvements in the throughput could be achieved by employing better polishing techniques with even smaller grit size lapping compounds.

5.6 The clinical Raman spectroscopy system

The clinical Raman instrument was designed to collect Raman and diffuse reflectance (DRS) spectra in transmission mode from thin tissues (Fig. 5-13). It used an 830 nm diode laser (Process Instruments) for Raman excitation, and a broadband source (AvaLight-HAL-S, Avantes) for DRS measurements (DRS provides useful information for tissue turbidity correction in tissue Raman spectroscopy [35, 34, 33]). These sources were delivered to the tissue via separate optical fibers (400 μm core, 440μm cladding, 0.26 NA, Fiberguide Industries). In particular, the Raman excitation fiber had a shortpass fused silica filter rod (0.62 mm diameter, Barr Associates) at the distal tip, in order to suppress the Raman scattered photons generated by the excitation fiber itself.

After the Raman excitation light was scattered and transmitted through a thin tissue (e.g., the thenar fold of an adult human hand, ~3 mm thick), the Raman scattered light was collected from the opposite side of the tissue by the CHC (Fig. 5-13). The CHC, coupled with a 50 mm diameter focusing lens of focal length 150 mm, redirected any scattered photons (half angles within $\pm 90°$) transmitted through its input aperture to be within a narrow range of angles (half angles within $\pm 3.9°$), collimating the scattered light to 0.068 NA. The collimated light was then filtered

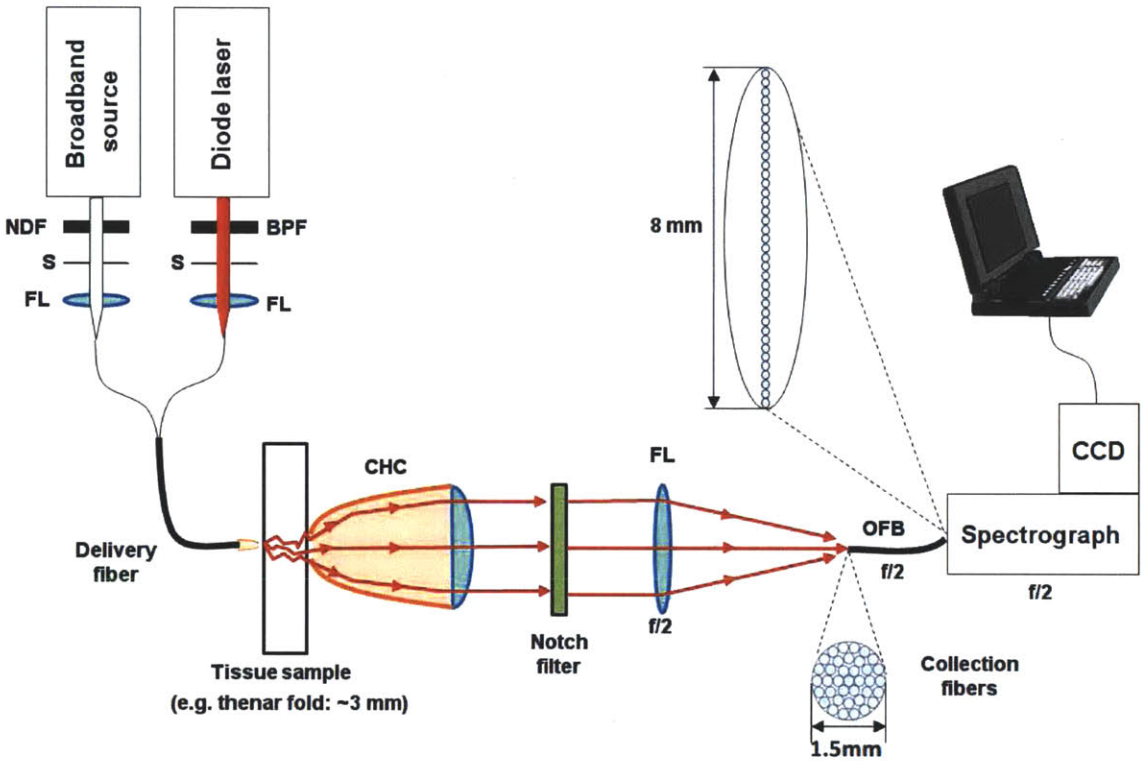

Figure 5-13: Transmission mode clinical Raman spectroscopy setup with CHC. (NDF: Neutral density filter, BPF: Bandpass filter, S: Shutter, FL : Focusing Lens, OFB: Optical fiber bundle.) With the Raman excitation light illuminated on one side of the thin tissue sample (such as the thenar skin fold), the Raman scattered light emerges from the other end of the tissue. The CHC collects Raman scattered light at all conic half angles ($\pm 90°$) and collimates to within $\pm 3.9°$. The collimated light is then filtered through a holographic Rayleigh rejection notch filter and focused onto the collection fiber bundle. On the other end, the collection fiber bundle is arranged to form a column of light with its height matched to the size of the CCD detector.

through a 50 mm diameter 830 nm holographic notch filter (Kaiser Optical Systems, Inc.), which efficiently rejected the Rayleigh scattered light while transmitting Raman scattered light. Without collimation by the CHC, the light would have reached the filter at a wide range of angles and the filter performance would have been degraded as its stopband wavelength and optical density varied with the angle of the incident light [82, 83]. The filtered light was then focused onto an optical fiber bundle (1.5 mm diameter, Romack, Inc.) composed of 37 closely packed (76% packing fraction) jacket-stripped collection fibers (200 μm silica core, 220 μm silica cladding, 0.26 NA, Fiberguide Industries) (Figs. 5-13, 5-14). The proximal end of the transmission mode collection fiber bundle (facing the spectrograph input) formed a single 8 mm column of optical fibers to match the height of the CCD detector. The fiber bundle length was limited to 50 cm in order to minimize the generation of undesirable background Raman spectra from the collection fibers, arising from any stray Rayleigh scattered photons that might have leaked through the notch filer. The collected Raman scattered light was then dispersed by the spectrograph (f/2, 6.23 nm/mm dispersion, 4.8 cm^{-1} spectral resolution, LS 785, Princeton Instruments) and detected by a back-illuminated deep-depletion CCD with 1340×400 array of pixels (each pixel 20×20 μm), thermoelectrically cooled to -70°C (Spec-10:400BR, 75% quantum efficiency at 850-960 nm), Princeton Instruments). The entire setup fitted inside a wheeled cart (37×18×42 in.) to facilitate portability during its use in the clinical setting.

For convenient access to remote and obscure areas of the human body, the instrument could also use an optical fiber probe (3.5 mm diameter) to collect Raman spectra in back-scattered mode (Fig. 5-15). The optical fiber probe was composed of a CPC, a Raman excitation fiber, a DRS excitation fiber, 17 collection fibers (400 μm core, 440μm cladding, 0.26 NA, Fiberguide Industries), a custom manufactured fused silica notch filter tube (0.97 mm inner diameter, 3.47 mm outer diameter, Barr Associates) and a shortpass filter rod (0.62 mm diameter, Barr Associates)[75, 85] (Fig. 5-15). Although a CPC of length 9 mm was sufficient for accommodating the 0.26 NA of the optical fibers, a CHC of a similar size coupled with a matching focusing lens would provide a much higher degree of collimation required for better

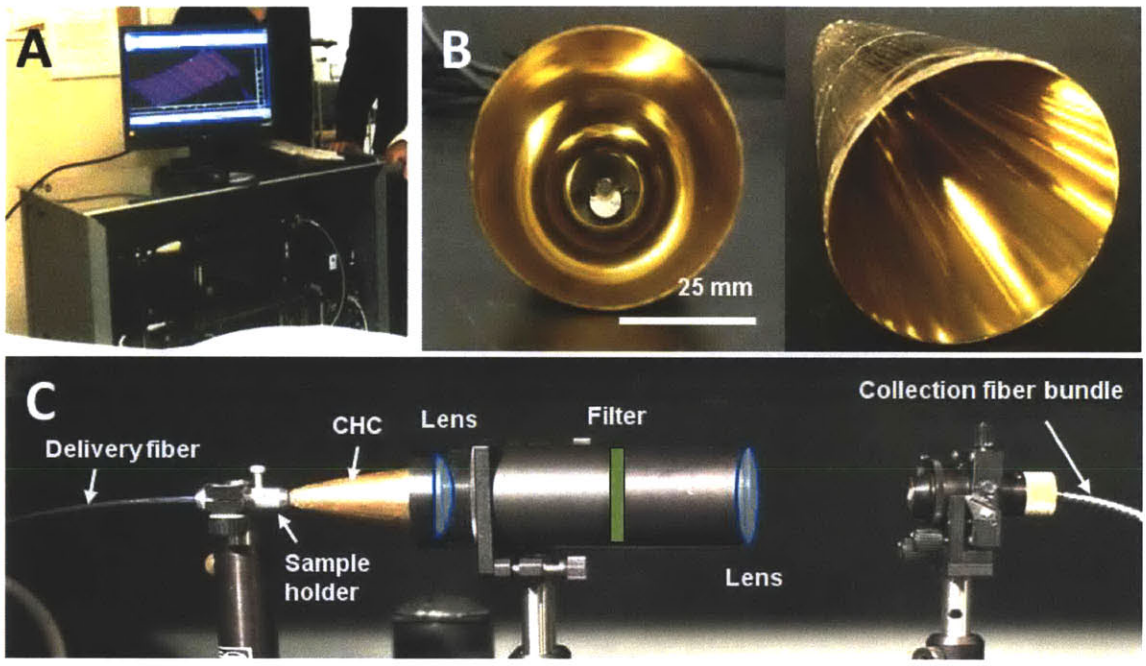

Figure 5-14: CHC-based clinical Raman spectroscopy instrument used for human subject studies. (A) The entire instrument fits inside a wheeled cart to facilitate portability during clinical studies. (B) The manufactured CHC seen from the output aperture. The interior surface was evenly coated with pure gold and polished to optical grade fineness. (C) Side view of the transmission mode Raman spectroscopy setup.

Table 5.1: Comparison of system throughputs of bench-top system and the portable clinical system in back-scattered mode (CPC-based) and transmission mode (CHC-based).

Throughput Factors	Bench-top[87] (Back-scattered)	Portable, CPC (Back-scattered)	Portable, CHC (Transmission)
Collection efficiency	21%	41%	59%
Packing fraction	62%	25%	76%
AR coatings	64%	90%	90%
CCD detector	60%	75%	75%
Total	5%	7%	30%

notch filter performance. In addition, depending on the requirements for the specific tissue targets, other back-scattered mode probe configurations such as oblique angle illumination [74, 86] and dichroic mirrors [77] could be employed.

5.7 System performance

5.7.1 Throughput

In Table 5.1, the throughput and efficiency of a bench-top Raman spectroscopy system [87] was compared with those of the portable system in the two available modes. The bench-top system operated in back-scattered mode, with a half paraboloidal mirror as the primary collecting optic, and an optical fiber bundle for coupling the collection optics with the spectrograph. The portable system could be operated in back-scattered mode with a compact CPC-based optical fiber probe. The collection efficiency of the CPC (41%) was much higher than that of the half paraboloidal mirror (21%) used in the bench-top system. However, the optical fiber packing fraction was much lower in the portable system (25%, as opposed to 62% of the bench-top system). This was due to the complexity in the compact optical fiber probe design, which sacrificed much of the collection area to the central excitation fiber and custom manufactured optical filters (Fig. 5-15). On the other hand, the portable system used more recent AR coating and CCD technologies, which provided a slight increase in throughput (Table 5.1). The overall throughputs of the two systems were very

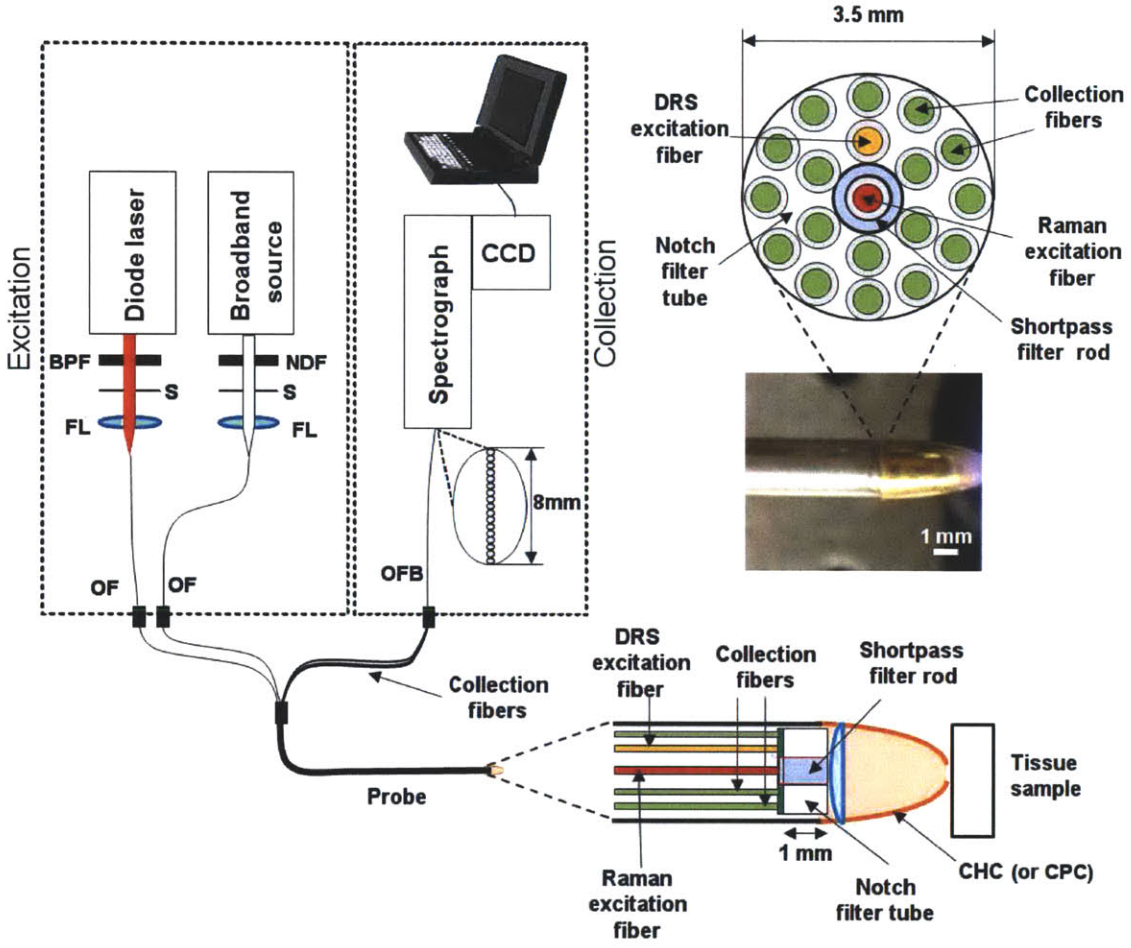

Figure 5-15: Back-scattered mode Raman spectroscopy system with a CPC-based optical fiber probe. Although the CPC of length 9 mm was sufficient for accommodating the 0.26 NA of the optical fibers, a CHC of a similar size coupled with a matching focusing lens would provide a much higher degree of collimation required for better notch filter performance. (NDF: Neutral density filter, BPF: Bandpass filter, S: Shutter, FL : Focusing Lens, OF: Optical fiber, OFB: Optical fiber bundle.)

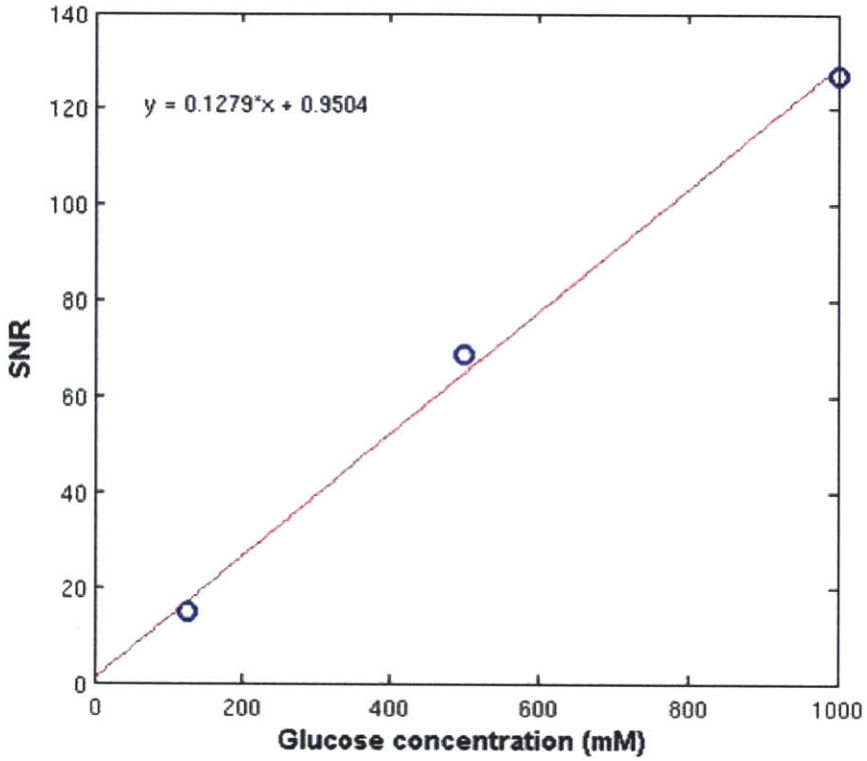

Figure 5-16: Estimation of minimum detectable glucose concentration. SNR of the Raman spectra collected from aqueous glucose solutions at concentrations of 125 mM, 500 mM and 1 M. Extrapolation to SNR=1 gave 0.39 mM, which corresponded to the minimum detectable glucose concentration of 1.2 mM (or 22 mg/dl).

similar: 5% for the bench-top system and 7% for the portable CPC-based system.

The throughput of the portable clinical Raman spectroscopy system increased significantly when converted into CHC-based transmission mode. Both the collection efficiency (59%) and the optical fiber packing fraction (76%) were superior to the bench-top system, with an overall throughput of 30% (Table 5.1). Even when the AR coating and CCD efficiency values were matched with the bench-top system, the overall throughput was 17%, which is still significantly higher than the 5% throughput of the bench-top system.

5.7.2 Minimum detectable glucose concentration

In order to estimate the minimum detectable glucose concentration, Raman spectra were collected from aqueous glucose solutions of concentrations 125 mM, 500 mM and 1 M. Although normal physiological glucose concentrations rarely rise above 20 mM, these concentrations were used to facilitate accurate estimation of the signal-to-noise ratio of the spectra. At each concentration, the SNR of the collected Raman spectra were plotted against the corresponding concentrations (Fig. 5-16). By extrapolating these points with a line towards lower SNR values, and the glucose concentration corresponding to SNR=1 was noted to be 0.39 mM. This is estimated to the noise equivalent glucose concentration, as define previously by eq. 3.10. The minimum detectable glucose concentration can then be estimated by multiplying this value with the spectral overlap (non-orthogonality) factor, which was roughly estimated to be 3 [56]. Hence, the minimum detectable glucose concentration of the clinical Raman spectroscopy system was estimated to be 1.2 mM or, equivalently, 22 mg/dl.

5.7.3 Clinical data collection

Many biomedical Raman spectroscopy applications such as cancer [88, 89, 90] and atherosclerosis detection [91, 92, 93] look for changes in the bulk tissue composition and morphology reflecting the pathology, which are well represented in the tissue Raman spectra. However, in the application of Raman spectroscopy for transdermal glucose level measurement, Raman signatures of aqueous glucose contribute only a very small fraction of the total tissue Raman spectra [94, 25]. As such, the performance of non-invasive glucose detection depends even more heavily on the quality of the Raman spectrum.

As described in Chapter 6, the CHC-based clinical Raman instrument was used successfully in a study that aimed to determine the clinical feasibility of using Raman spectroscopy for non-invasive glucose measurement. In that study, Raman spectra were collected from the thenar skin fold of the hands of human volunteers in transmission mode during oral glucose tolerance tests (OGTT), where the subjects ingested

a glucose-rich beverage to induce changes in blood glucose levels. At the same time, reference blood glucose levels were measured by using conventional finger-prick glucometers (SureStep Flexx, Johnson and Johnson). This protocol produced a set of skin Raman spectra (each composed of 1340 CCD intensity values) with corresponding reference blood glucose values. A calibration algorithm relating the Raman spectra to the corresponding glucose concentrations can be developed by using various chemometric techniques [50], such as partial least squares [95, 96], principal component regression [96] and support vector regression [97, 58, 39]. Support vector regression was performed on the data obtained with the clinical Raman instrument to create a calibration model for non-invasive glucose detection. Performing leave-one-out cross-validation of this model on the dataset showed good correlation between the concentrations predicted by Raman spectroscopy and the conventional finger-stick glucometer readings. This was achieved while using an 8 mm-height CCD detector with 1340×400 array of pixels (Princeton Instruments), 100 mW Raman excitation laser power and 1 minute acquisition time for each data point. Previous OGTT studies using a laboratory-based back-scattered mode instrument including a paraboloidal mirror and a 25.4 mm-height CCD detector with 1340×1300 array of pixels (Roper Scientific) required 200~300 mW Raman excitation laser power and 3 minute acquisition time for each data point, in order to achieve similar level of performance [57, 34].

5.8 Conclusion

A portable clinical Raman instrument has been developed using a CHC and a matching focusing lens. The CHC and lens combination achieved a very high degree of collimation for enhanced tissue Raman scattered light collection and efficient notch filter performance, while maintaining much smaller physical dimensions than a CPC designed to achieve the same. The instrument has been used successfully for collecting skin Raman spectra from human volunteers during OGTT, while using lower Raman excitation laser power and shorter acquisition times compared with laboratory-based

systems with similar performance. Besides collection of Raman spectra from skin tissues, the proposed CHC design could have many other uses in spectroscopy systems requiring efficient collimation of nearly isotropically scattered light from biological tissues.

Chapter 6

Human clinical study

6.1 Introduction

While artificial tissue phantoms can be studied in the laboratory settings to provide an insight into the clinical feasibility of Raman spectroscopy for transdermal glucose detection, these studies cannot completely replicate the real-life clinical conditions. Similarly, animal models, while tremendously useful, have limitations due to differences in the skin physiology and glucose metabolism compared with those of humans. Therefore, collecting and analyzing the skin Raman spectra from human subjects provide a unique opportunity to gain direct insight into the requirements for clinical translation of Raman spectroscopy for glucose measurement. In this study, the portable clinical Raman spectroscopy instrument described in Chapter 5 was used at the MIT Clinical Research Center (MIT CRC, Co-directors: John Gabrieli, Ph.D. and Ravi Thadhani, M.D., M.P.H.) to collect skin Raman spectra from human subjects undergoing an oral glucose tolerance test (OGTT). The measured Raman spectra and reference blood glucose concentration values were used to develop a calibration model, which was then tested for accuracy.

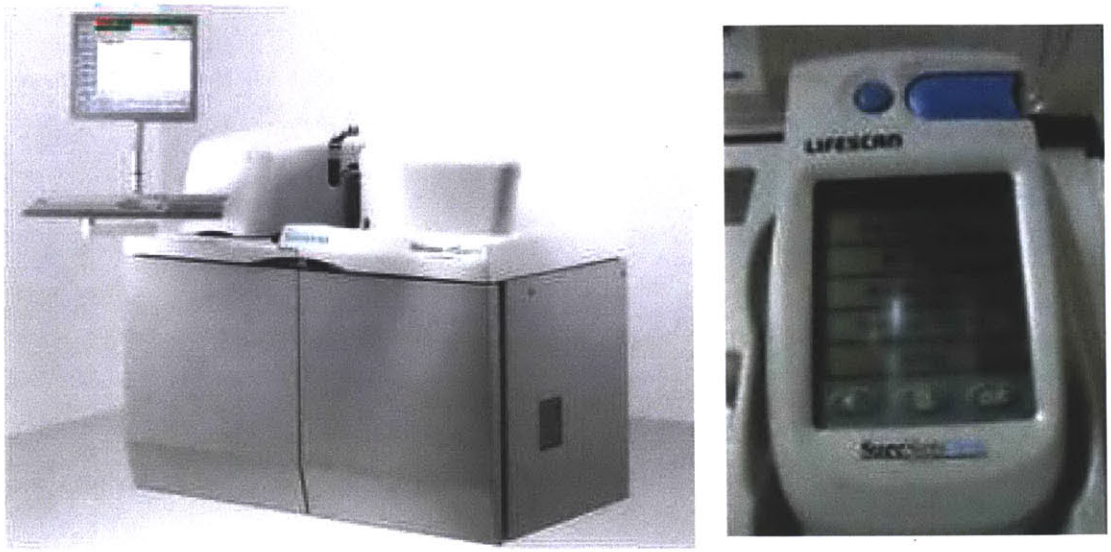

Figure 6-1: Glucose analyzers used for reference blood glucose measurements. Left: Siemens, Dimension Xpand, Right: Johnson and Johnson, Life Scan, SureStep Flexx.

6.2 Materials and methods

6.2.1 Reference blood glucose measurements

The accuracy of glucose concentration estimated by Raman spectroscopy and its calibration model cannot exceed the accuracy of the reference blood glucose measurements. For this reason, it is crucial to have a very accurate method of measuring glucose concentration to serve as the "gold standard" reference. The MIT CRC is equipped with a set of two clinical blood glucose meters (Johnson and Johnson, Life Scan, SureStep Flexx) (Fig. 6-1, right). Every month, these glucometers are calibrated against a more sophisticated and accurate chemical analyzer (Siemens, Dimension Xpand) (Fig. 6-1, left) by the MIT Medical Laboratory Department, to maintain an average precision of 3 to 4 mg/dl. Figure 6-2 shows typical calibration curves for both MIT CRC meters generated by the MIT Medical Laboratory Department, which both have an R^2 value of 0.99 or higher.

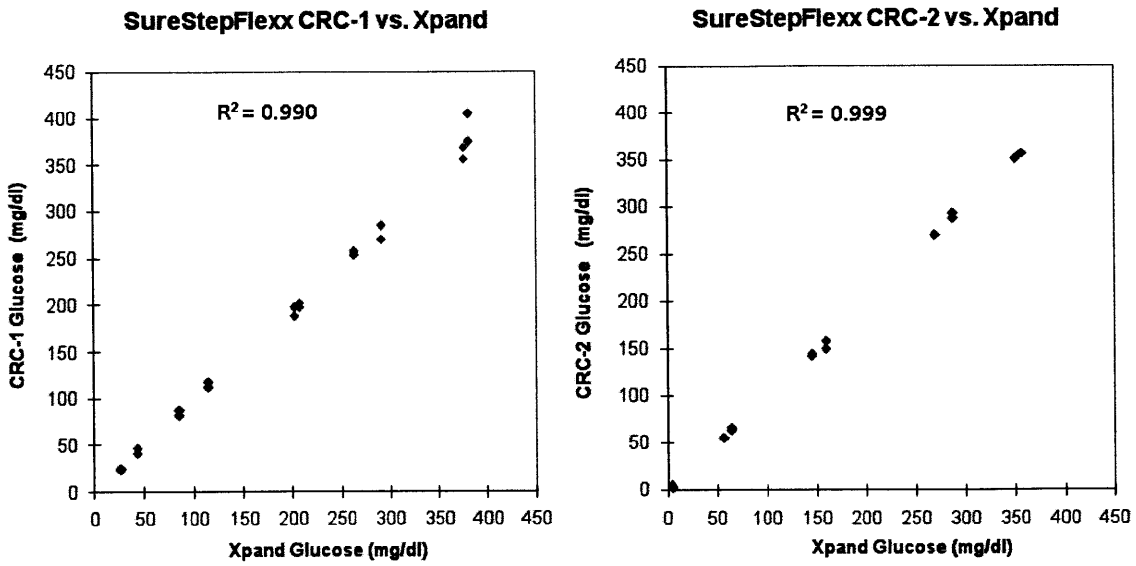

Figure 6-2: Calibration results for MIT CRC SureStep Flexx glucometers.

6.2.2 Arrangement of instruments and the human subject

The portable clinical instrument described in Chapter 5 was placed next to a hospital bed (Fig. 6-3), while the glucometers, lancets and other clinical supplies were placed on the other side of the bed. This was to facilitate simultaneous recording of skin Raman spectra and blood glucose concentrations from either side of the bed while the human subject sat on the bed. More importantly, for the safety of the human subjects, it is essential to perform the study with the subject resting on a bed, as frequent finger-pricks could trigger a vasovagal syncope in at least 10% of U.S. population due to needle phobia [3]. Vasovagal syncope is a nerve reflex response due to noxious stimuli (such as needle sticks) which induces fainting in the individual by sudden drop in blood pressure and reduced blood perfusion in the brain. When this happens, it is essential that the patient be placed in a "Trendelenburg position" (which is a supine position with the patient's legs raised above the head level [98]) in order to promote blood perfusion to the brain and help the patient return to consciousness. Although this is normally not a life-threatening event, there are documented cases of seizure and fatality due to vasovagal syncope [3, 99]. Such adverse effects of invasive blood glucose monitoring methods further motivate the need for a non-invasive glucose monitoring

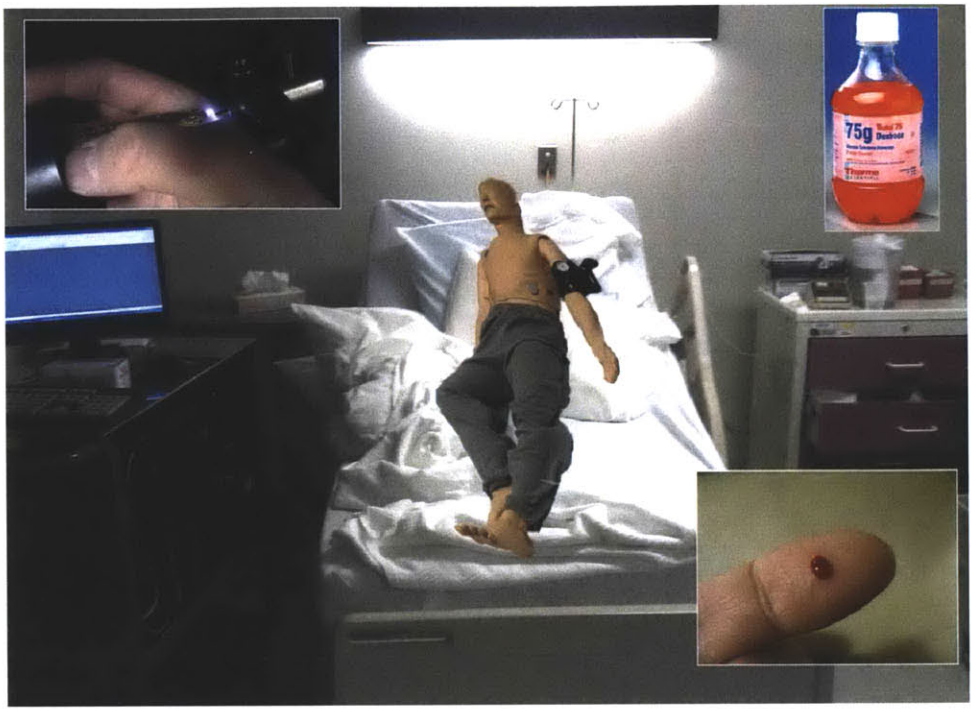

Figure 6-3: The clinical Raman spectroscopy instrument located next to a hospital bed at the MIT CRC. After 8 to 12 hours of fasting, the human subject (shown here as a mannequin to protect confidentiality) sits on the hospital bed and drinks the 75 g glucose beverage (top right). For the next 2 to 3 hours, Raman spectra were collected from the subject's right hand using the clinical Raman instrument while conventional finger-stick blood glucose measurements were made simultaneously from the left hand.

device. In order to minimize the possibility of vasovagal syncope, human subjects were screened before the study based on prior history of needle phobia or fainting. Despite these precautions, three vasovagal episodes occurred during this study with no adverse consequences to the human subjects.

6.2.3 Data acquisition and OGTT protocol

Prior to the beginning of the study, the human subject was required to fast for at least 8 to 12 hours, to ensure that the study was started at the fasting glucose level. If the fasting glucose level was above 125 mg/dl, the study was interrupted and the subject was discharged (as this indicates abnormality in the subject's glucose regulation ability and it may also prevent the collection of spectral and blood glucose

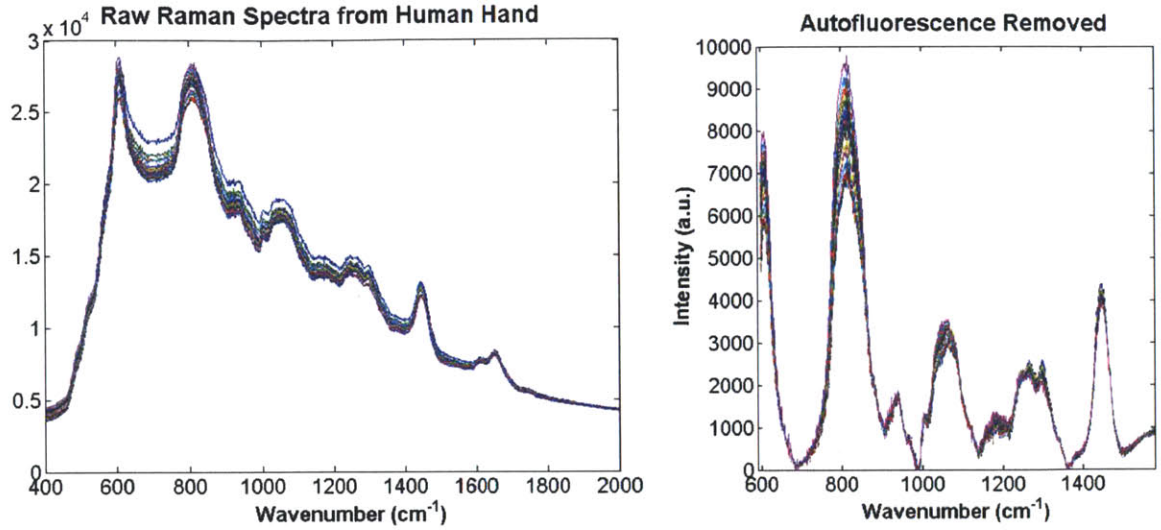

Figure 6-4: Thenar skin fold Raman spectra collected from one human subject during OGTT. Left: Raw, unprocessed Raman spectra. Right: Raman spectra processed to remove tissue autofluorescence background.

data over a wide enough range of glucose levels). Then the subject was given a standard glucose solution drink widely used in the clinics for OGTT (75 g glucose, Trutol, Thermo Scientific). Over the course of 2 to 3 hours, Raman spectra were collected every 5 minutes from the thenar skin fold in transmission mode (830 nm laser at 100 mW, 1 minute acquisition). Concurrently, blood glucose measurements were taken by finger-sticks every 10 minutes. All clinical study protocols involving human subjects were conducted after receiving approval by the MIT Committee On the Use of Humans and Experimental Subjects (COUHES).

6.3 Results and discussion

6.3.1 Tissue autofluorescence removal

A typical set of Raman spectra collected from the human subjects is shown in Fig. 6-4. In this figure, it can be seen that the raw Raman spectra shown on the left panel have a slowly varying background arising from tissue autofluorescence. This tissue autofluorescence interferes with glucose detection in two ways:

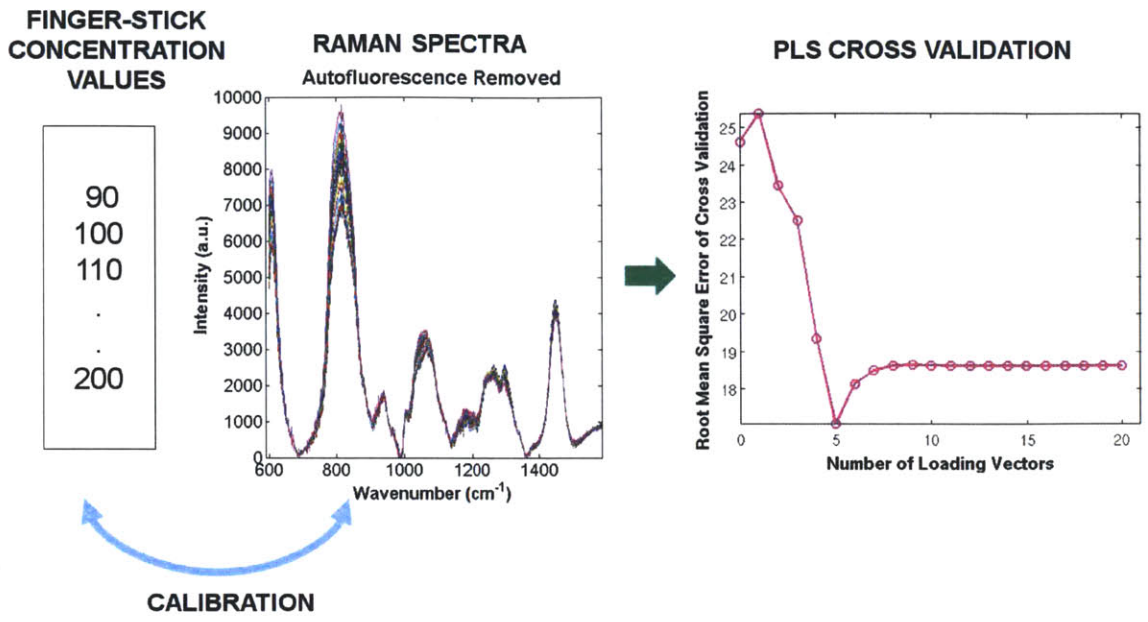

Figure 6-5: PLS calibration performed on clinical Raman spectroscopy and blood glucose concentration data. Leave-one-out cross-validation was performed by developing a calibration model on all but one pair of Raman spectrum and corresponding reference blood glucose concentration. The developed model was then tested on the remaining data pair. This procedure was repeated until all combinations were exhausted.

1. The tissue autofluorescence raises the overall intensity of the spectra, thereby increasing the CCD shot noise.

2. The tissue autofluorescence undergoes time-dependent fluorescence photobleaching, which may falsely correlate with time-dependent changes in glucose levels.

These detrimental effects of tissue autofluorescence photobleaching on blood analyte detection had been studied previously by Barman, Kong and co-workers [36]. In order to remove the autofluorescence background, the Raman spectra were processed with a modified low-order polynomial curve-fitting technique developed by Lieber et al. [38]. The result of this "Lieber-fitting" step is shown on the right panel of Fig. 6-4.

6.3.2 Calibration model development

The calibration model was developed using partial least squares (PLS) technique. As mentioned previously, PLS is a linear regression technique that obtains a regression vector which relates the Raman spectrum to the corresponding reference glucose concentration with the maximum amount of sensitivity (Fig. 6-5).

In addition, a non-linear regression technique based on support vector machine (SVM) was used as suggested by a recent study which demonstrated improvements in blood analyte detection accuracy over conventional PLS regression [39]. These improvements may be due to non-linear and non-glucose specific variations in the Raman spectra such as those arising from tissue turbidity variations, which could adversely affect conventional linear regression techniques [39]. In brief, unlike PLS and other least squares regression techniques that use a quadratic loss function to assign penalty to data points lying farther away from the regression points, SVR uses an even more sensitive non-quadratic loss function in order to enhance robustness in regression against spurious outliers [100]. In order to implement SVM-based regression (SVR), a computer code library developed by Chang and Lin [101] was used to perform calibration and prediction on the clinical Raman spectra and blood glucose concentrations.

Finally, for each spectroscopic calibration method, the dynamic concentration correction (DCC) scheme described in Chapter 3 was used to see if calibration accuracy can be improved by correcting for the lag between blood and interstitial fluid glucose concentrations. In the following sections, the calibration and prediction algorithm performance was tested by applying increasingly rigorous tests.

6.3.3 Verification of calibration

Raman spectra of the thenar skin fold and the corresponding finger-stick blood glucose measurements were obtained from 18 human subjects during 28 separate OGTT sessions (730 data points). As described later, some human subjects underwent multiple OGTT sessions on different days in order to test for prospective prediction perfor-

mance. The relationship between the clinical Raman spectroscopy and blood glucose concentration data were extracted by applying four different calibration methods:

1. PLS regression on raw Raman spectra
2. PLS regression on Raman spectra with autofluorescence removed
3. SVR on raw Raman spectra
4. SVR on Raman spectra with autofluorescence removed

In addition, these calibration methods were repeated with DCC implementation. In order to observe the calibration and prediction performance, the results were plotted on a Clarke error grid (Fig. 6-6), which is an analysis tool widely used in the diabetic research community to characterize the performance of a glucose sensing device [102]. The regions labeled in the Clarke error grid have the following clinically significant implications:

- Region A: Estimated values within 20% of the reference value. Ideally, all data points should lie in this region.
- Region B: Estimated values outside of 20% but would not lead to inappropriate treatment.
- Region C: Data points in this region may lead to unnecessary treatment.
- Region D: Data points indicating dangerous failure to detect hypoglycemia or hyperglycemia.
- Region E: Data points leading to wrong diagnosis and leading to inappropriate treatment of hypoglycemia or hyperglycemia that can worsen the condition.

The U.S. Food and Drug Administration (FDA) specifies a minimum requirement for all glucose sensing devices that greater than 95% of the data points should lie in the A or B regions in order for them to be permitted for clinical use. However, for practical clinical applications, the FDA also specifies a desirable performance guideline of a

maximum error of 15% error for glucose levels less than 75 mg/dl and a maximum of 20% error for levels greater than 75 mg/dl. Similarly, the International Organization for Standardization (ISO) requires a maximum error of 15 mg/dl error for glucose levels less than 75 mg/dl and a maximum of 20% error for levels greater than 75 mg/dl.[§] In Fig. 6-6, these guidelines corresponded to the region delimited by the dotted lines for glucose levels less than 75 mg/dl, and the "A" region for glucose levels greater than 75 mg/dl.

More recently, Parkes et al. suggested an alternative to the existing Clarke error grid. Named "Consensus Error Grid", or sometimes alternatively called "Parkes Error Grid", this new error grid was based on the consensus of 100 endocrinologists in a survey conducted to grade the clinical risk and importance of the regions of the estimated vs. reference glucose concentration plot [104]. In contrast, the Clarke error grid was developed by much smaller number of clinicians, and it has been criticized by some researchers for the discontinuities in the clinical risk boundaries [105, 106]. More glucose sensor manufacturers have recently started to use this new error grid over the conventional Clarke error grid, and it remains to be seen whether the new error grid will officially replace the conventional Clarke error grid.

For each calibration method, an initial verification was done by performing calibration using all the data points within the OGTT data set, and predicting on each data point within the same data set ("leave-none-out" cross validation, Fig. 6-6). Since the calibrated algorithm is predicting on its own calibration data, the leave-none-out cross validation is essentially a self-fit. In Figs. 6-6 and 6-7, the corresponding data points on the Clarke error grid lie very close to the 45 degree line (with R^2 close to one) for all calibration methods, indicating a good calibration based on these data sets. However, these results reveal little about the prediction performance, as the calibrated algorithms should by definition reflect the features of the calibration data set.

[§]As of 2010, these guidelines are being reviewed by the FDA for a more stringent requirement of 10 or 15% maximum error [103].

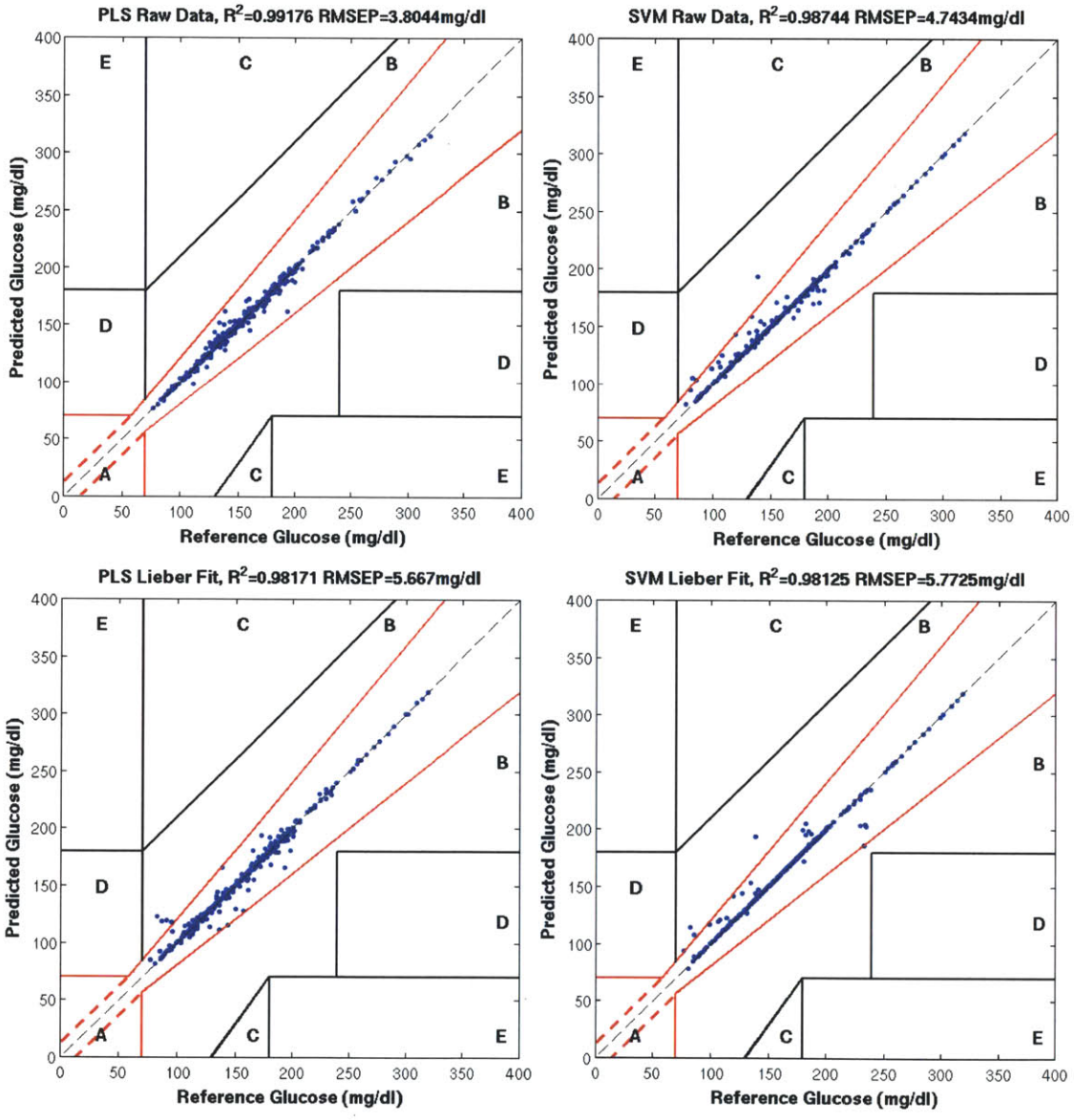

Figure 6-6: Leave-none-out cross validation. Verification of calibration by self-predicting on the calibration data (18 human subjects, 28 OGTTs, 730 data points).

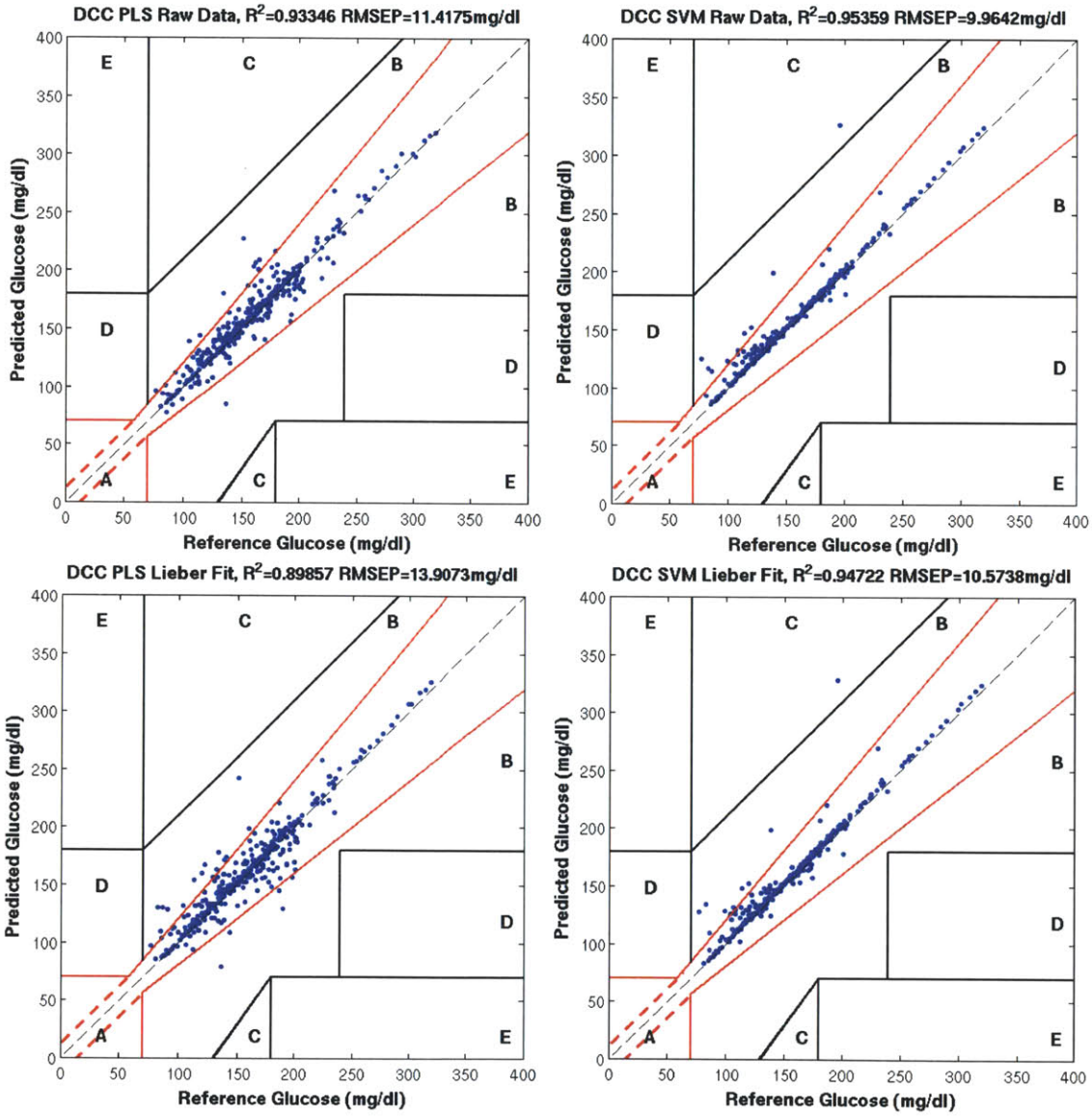

Figure 6-7: Leave-none-out cross validation, with DCC. Verification of calibration with DCC by self-predicting on the calibration data (18 human subjects, 28 OGTTs, 730 data points).

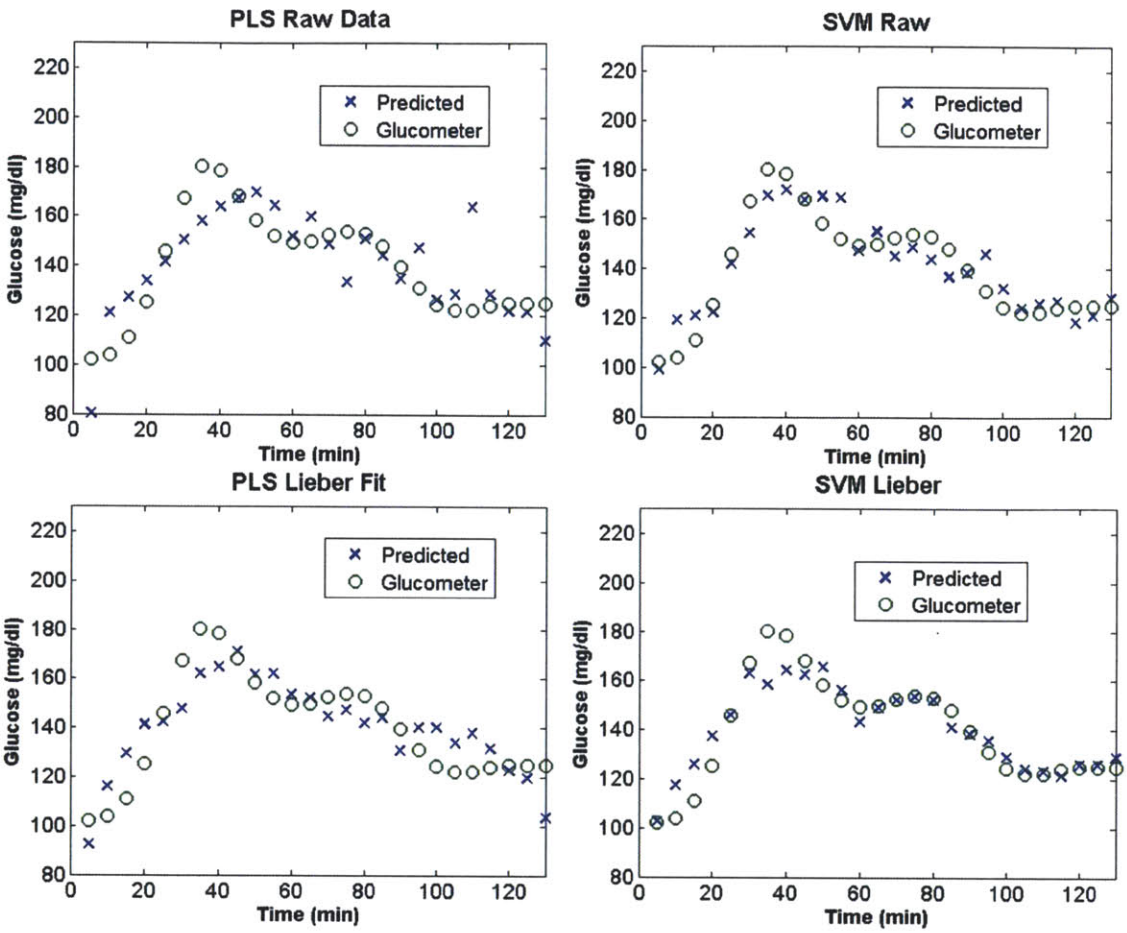

Figure 6-8: Time course of glucose concentrations measured during an oral glucose tolerance test, as measured by conventional finger-prick glucometer ($\circ$) and Raman spectroscopy via leave-one-out cross validation ($\times$).

6.3.4 Leave-one-out cross validation

For a more rigorous verification of calibration, leave-one-out cross-validation was performed on the data set for each calibration method. In this procedure, all but one set of Raman spectrum and corresponding reference blood glucose concentration were used to perform the calibration. The regression vector produced as a result of this calibration step was then tested by predicting on the remaining Raman spectrum and blood glucose concentration data pair. This procedure was repeated by selecting another data pair to be left out, until all combinations were exhausted. While the data sets involved are all from the same OGTT session, such leave-one-out cross-validation

procedure is prospective in nature, as the data set used for prediction is not included in the calibration data set.

Figure 6-8 shows the time course of glucose concentrations measured during an oral glucose tolerance test for one human subject, as measured by conventional finger-prick glucometer (o) and Raman spectroscopy via leave-one-out cross validation (×). In this figure, it can bee seen that conventional PLS regression on the raw Raman spectra performed the worst, while better performance was observed with SVR, where the glucose concentrations measured by the glucometer matched closely with those estimated by Raman spectroscopy. This data set, however, was from only one human subject.

A more complete view of the performance comparisons can be seen in the Clarke error grid of Fig. 6-9, which summarizes the results of leave-one-out cross-validation performed on 18 human subjects, during 28 OGTT sessions (730 data points). In this figure, it can be seen that SVR tends to improve cross validation accuracy compared with the corresponding PLS regression methods. An initial assessment on 11 human subjects seemed to indicate an apparent improvement in calibration accuracy by autofluorescence removal. However, upon completion of the analysis of all 18 human subject data, applying autofluorescence removal by Lieber-fitting did not improve the calibration accuracy for either PLS or SVR. In fact, it slightly increased the cross validation errors, making the PLS calibration with Lieber-fitting to have the worst cross validation performance. This suggests that subtracting the low order polynomial to remove autofluorescence may have actually had negative effects on the calibration accuracy by introducing undesirable spectral distortions. It also suggests that there is little or no spurious correlation between autofluorescence photobleaching and glucose concentrations during these OGTT protocols, which all exhibited non-monotonic rise and fall in glucose levels in contrast to the autofluorescence intensity variation by photobleaching which is typically a monotonic exponential decay. However, the effect of autofluorescence background removal may become more significant when the calibration algorithm is used prospectively on different OGTT data sets, which may have a much higher or lower autofluorescence intensities.

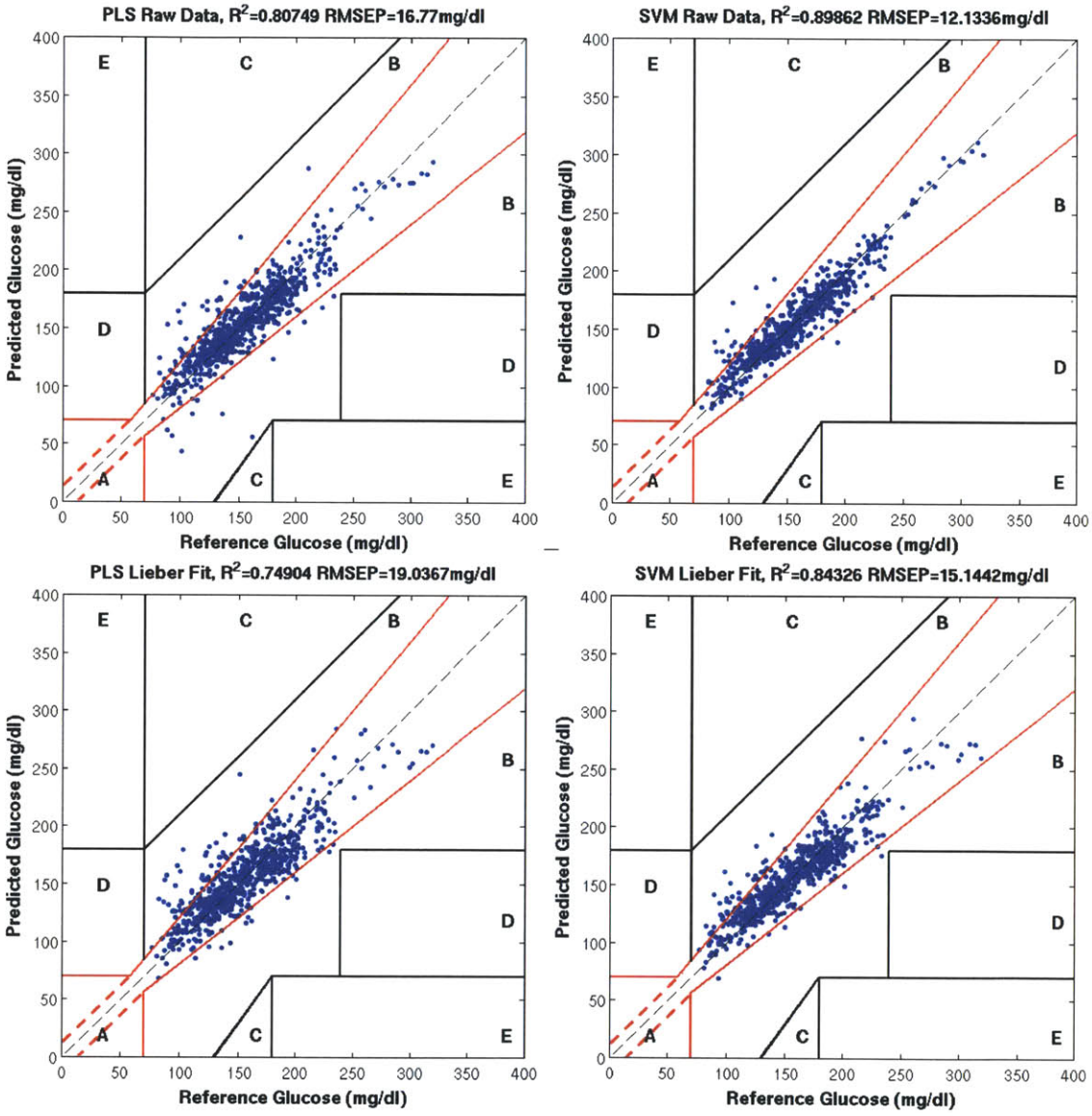

Figure 6-9: Leave-one-out cross-validation performed on clinical Raman spectra and blood glucose concentrations collected from 18 human subjects (28 OGTTs, 730 data points).

For all four calibration methods, 100% of the data points were in the "A" or "B" region, more than satisfying the minimum FDA requirement for clinical application. In addition, for all four calibration methods, over 90% of the data points were in the "A" region and satisfied the target guidelines of both FDA and ISO. In particular, for the case of SVR calibration on raw Raman spectra, 97% of the data points were in the "A" region (with RMSEP of 12.13 mg/dl) and satisfied the target guidelines of both FDA and ISO.

Finally, the same calibration methods were repeated with DCC implementation (Fig. 6-10). In this figure, the order of performance of the four calibration methods were the same as that of Fig. 6-10, with little change in cross-validation errors. This may be due to the fact that, unlike the forearm or the abdominal skin, the palmar thenar skin is relatively well-vascularized by a mesh of capillary vessels [107]. In fact, for these 18 subjects, the optimal lag time constant α as estimated by the DCC PLS calibration process had a mean value of 1.9 min (standard deviation of 0.16 min) which is much shorter than that observed in the forearm and abdominal skin (around 10 minutes). This suggests that implementation of DCC could have different results depending on the degree of vascularization of the specific anatomical site. Furthermore, Thennadil et al. suggested that the observed lag time cited in the literature involving electrochemical sensors may be partly due to the lag contributed by the sensor itself, as they have observed much shorter lag in glucose concentrations when measured by direct interstitial fluid aspiration from the forearm and dorsal hand skin [108]. As such, the cited lag time of about 10 minutes as measured by electrochemical interstitial fluid sensors may require further verification by using an interstitial fluid aspiration study as described by Thennadil et al [108].

6.3.5 Prospective prediction on different days

For practical non-invasive glucose monitoring, the device should require only a one-time or infrequent calibration sessions for successful glucose predictions in subsequent measurements. The leave-one-out cross validations performed in the previous section only demonstrate glucose measurement ability within the same OGTT calibration

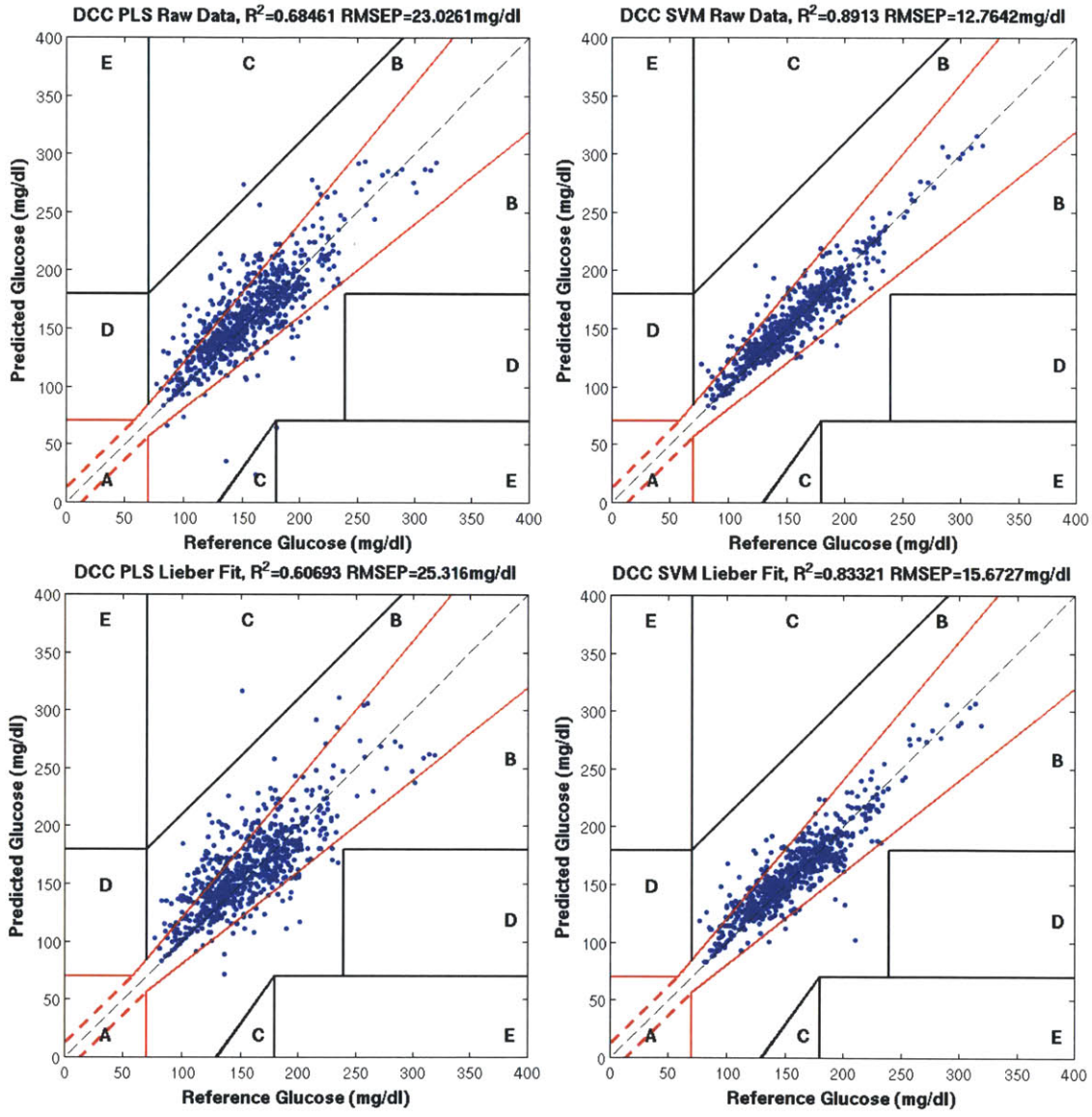

Figure 6-10: Leave-one-out cross-validation with DCC performed on clinical Raman spectra and blood glucose concentrations collected from 18 human subjects (28 OGTTs, 730 data points).

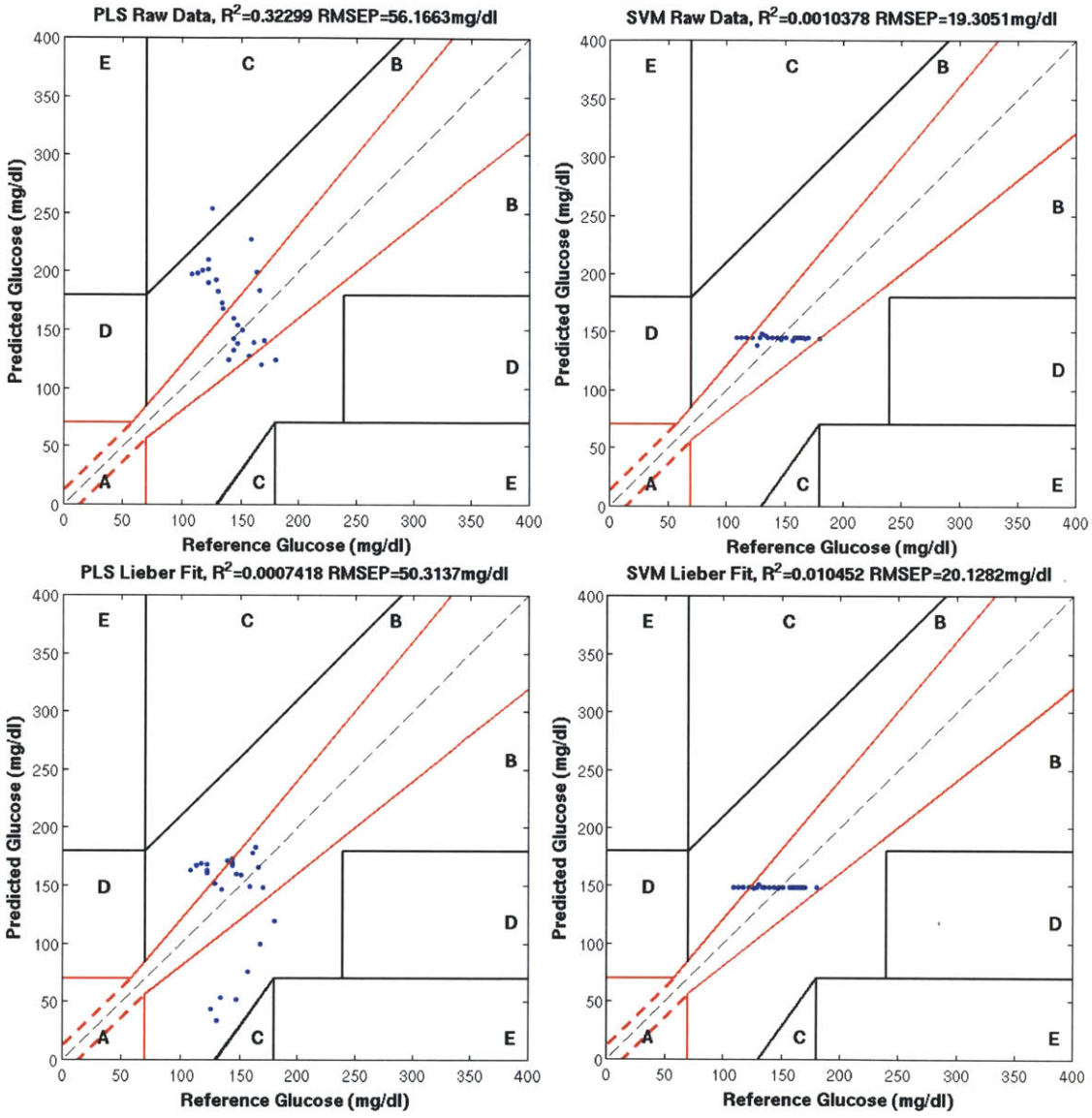

Figure 6-11: Prospective prediction performed on one human subject. Calibration performed on one set of OGTT data was used to predict on another set of OGTT data obtained from the same subject on a different day.

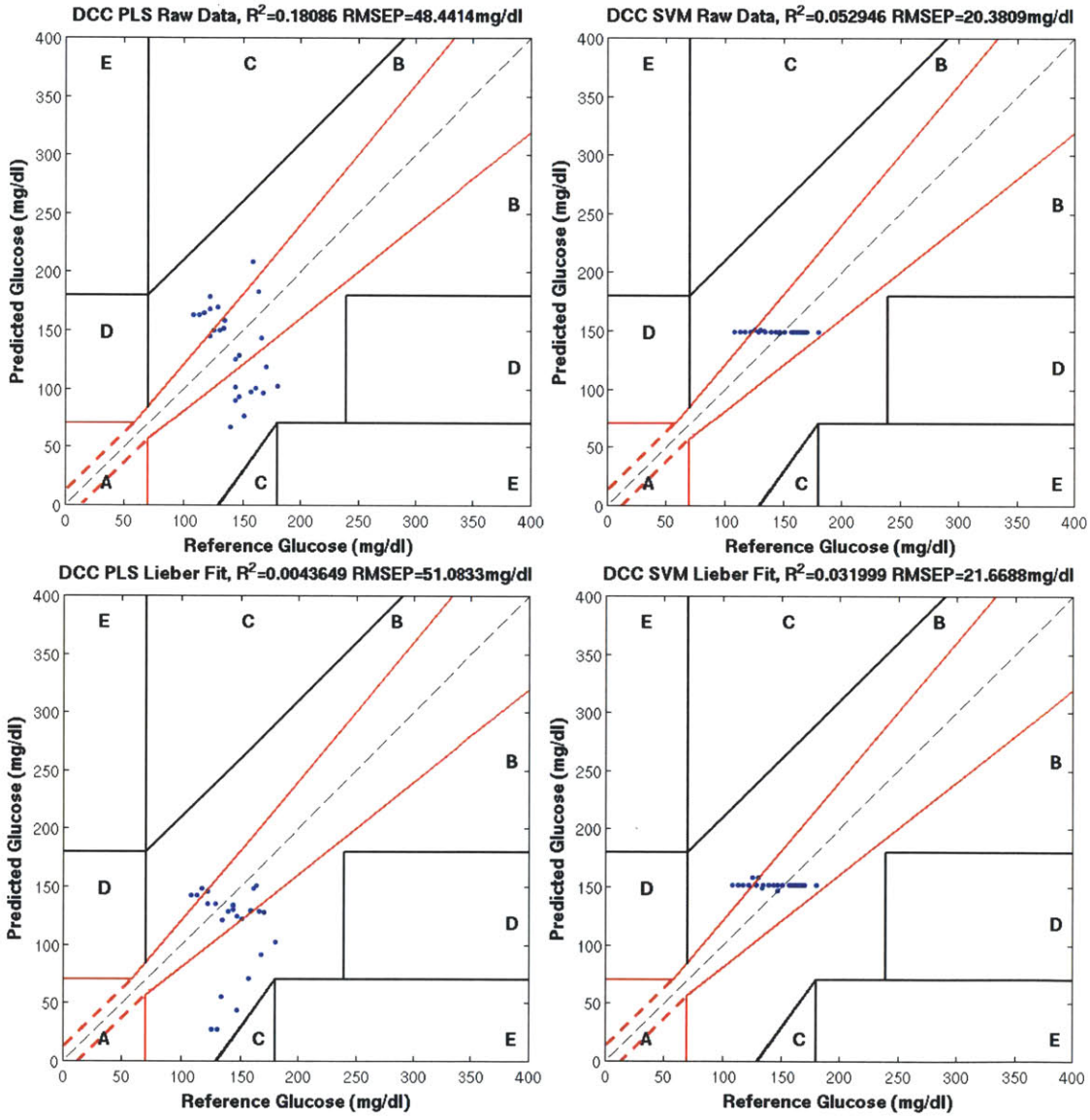

Figure 6-12: Prospective prediction performed with DCC on one human subject. Calibration performed with DCC on one set of OGTT data was used to predict on another set of OGTT data obtained from the same subject on a different day. (The same data set as the previous figure.)

session, or in different OGTT sessions with exactly identical measurement conditions. While these conditions are applicable for a miniaturized and wearable device which consistently measures Raman spectra from exactly the same location, the size of present prototype require reattachment of the device to the skin fold for each separate OGTT session, which presented difficulties in prospective predictions. In this section, the skin Raman spectra and blood glucose concentration data from the same human subjects are analyzed over multiple OGTT sessions in order to test for the prospective prediction performance of the calibration methods. Out of the 18 human subjects, 5 subjects were asked to participate in more than one OGTT sessions. The results of prospective prediction on one such subject is shown in Figs. 6-11 and 6-12. In Fig. 6-11, one data point in the case of PLS regression on raw Raman spectra was in the "C" region, while the rest of the data points as well as those of the other calibration methods were in the clinically acceptable "A" or "B" regions. While these satisfied the minimum FDA requirement for clinical use, the data points for the SVM based regression formed a flat horizontal line, which clearly indicated the failure to show sensitivity to glucose variations. This suggests that although SVM based regression showed superior cross-validation results within the same OGTT session, it was not flexible enough to be carried over to another OGTT session. Specifically, the calibration by SVM based regression was done on a hyperplane at which the prospective Raman spectra did not have any significant glucose-specific variations. This could also be interpreted as a form of "overfitting". On the other hand, the PLS regression based methods were able to transfer some of their glucose sensitivity to another OGTT session (Fig. 6-11), albeit with significant degradation in performance compared with leave-one-out cross validation. In Fig. 6-12, implementation of DCC slightly reduced the prediction error for the case of PLS regression on raw spectra while leaving other cases largely unaffected.

Similar prospective prediction was performed on the remaining four human subjects to produce Fig. 6-13, where a total of five human subjects underwent multiple OGTT sessions on 2 to 5 different days. In these subjects, prospective prediction by SVM based calibration methods again produced series of flat horizontal lines indicat-

ing lack of glucose sensitivity. On the other hand, the PLS based calibration methods showed better glucose sensitivity which somewhat improved with DCC implementation (Fig. 6-14), although many data points were in clinically undesirable "C" and "E" regions. This shows that a higher accuracy in leave-one-out cross validation within the same OGTT session does not necessarily translates to a better prospective prediction performance. In particular, while SVM based calibration provides smaller cross validation error by capturing the subtle non-linearities ignored by conventional PLS regression methods, it becomes less robust against non-glucose specific variations in prospective validations.

The difficulty in prospective prediction across multiple days is thought to arise mainly from the inability to reproduce exactly the same measurement conditions. Although spectral measurements can be made from approximately the same skin location, the multi-layered and heterogeneous nature of the skin tissue causes differences in the acquired Raman spectra unless collected at exactly the same angle and pressure. For this reason, even during the same OGTT session, a brief disruption due to the human subject's request to remove his or her hand from the device (e.g. to stretch or to use the rest room) was enough to significantly alter the spectral features and reduce the calibration accuracy. This suggests that a glucose monitoring device that uses Raman spectroscopy would perform the best when developed in a miniaturized and wearable form (e.g. like a watch or a ring) so that the device can be fixed on the skin surface and maintain its position relative to the skin tissue once a calibration session has been performed.

6.4 Conclusion

This study has used a portable clinical Raman spectroscopy instrument to collect Raman spectra from human subjects undergoing OGTT. The Raman spectra were collected from the thenar skin folds in transmission mode, using a non-imaging optic (CHC) for enhanced throughput. The study has also demonstrated that, within the same OGTT session with the CHC fixed on the same location on the skin, the

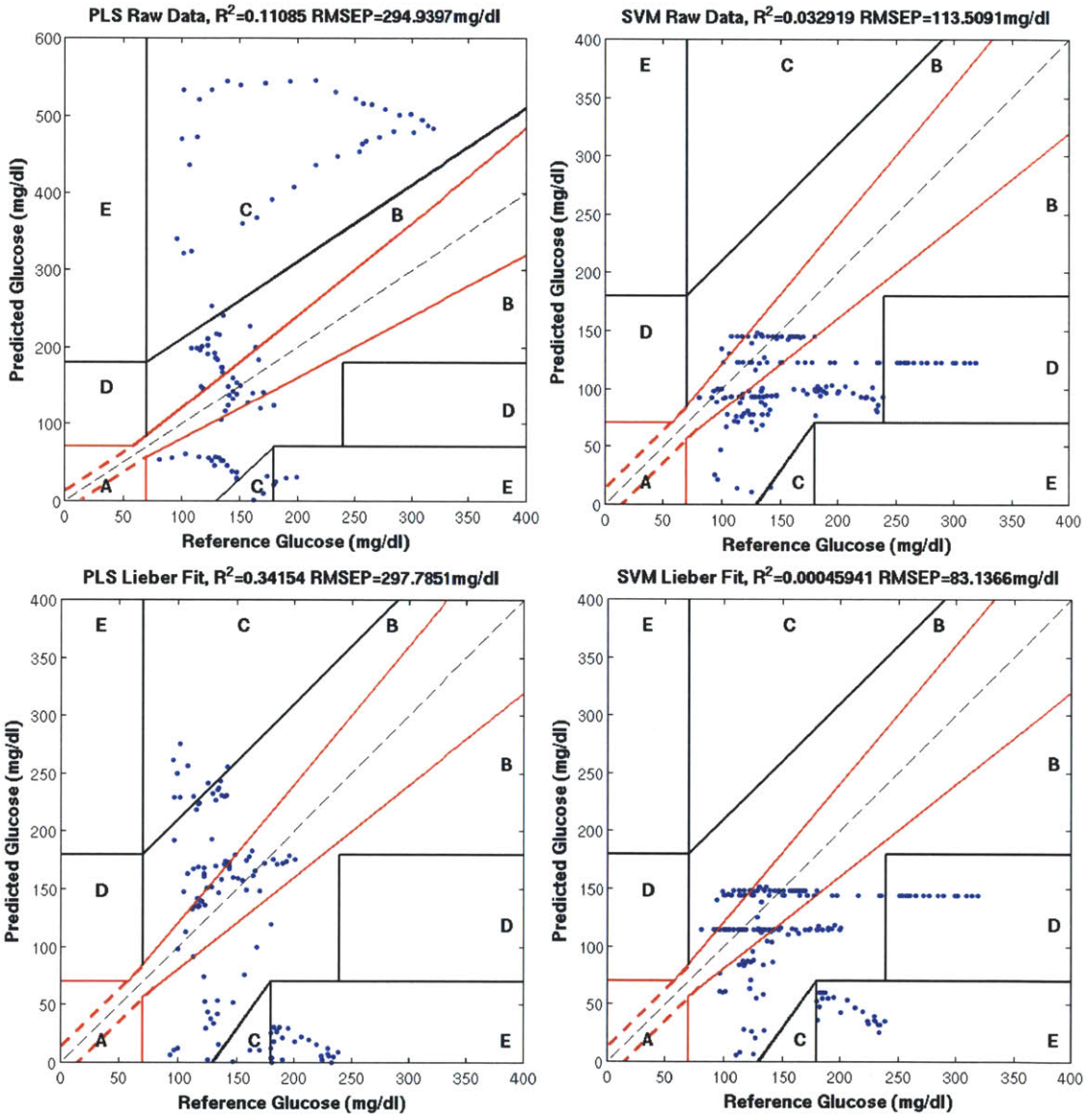

Figure 6-13: Prospective prediction performed on 5 human subjects. For each human subject, calibration performed on one set of OGTT data was used to predict on other sets of OGTT data obtained from the same subject on 2 to 5 different days.

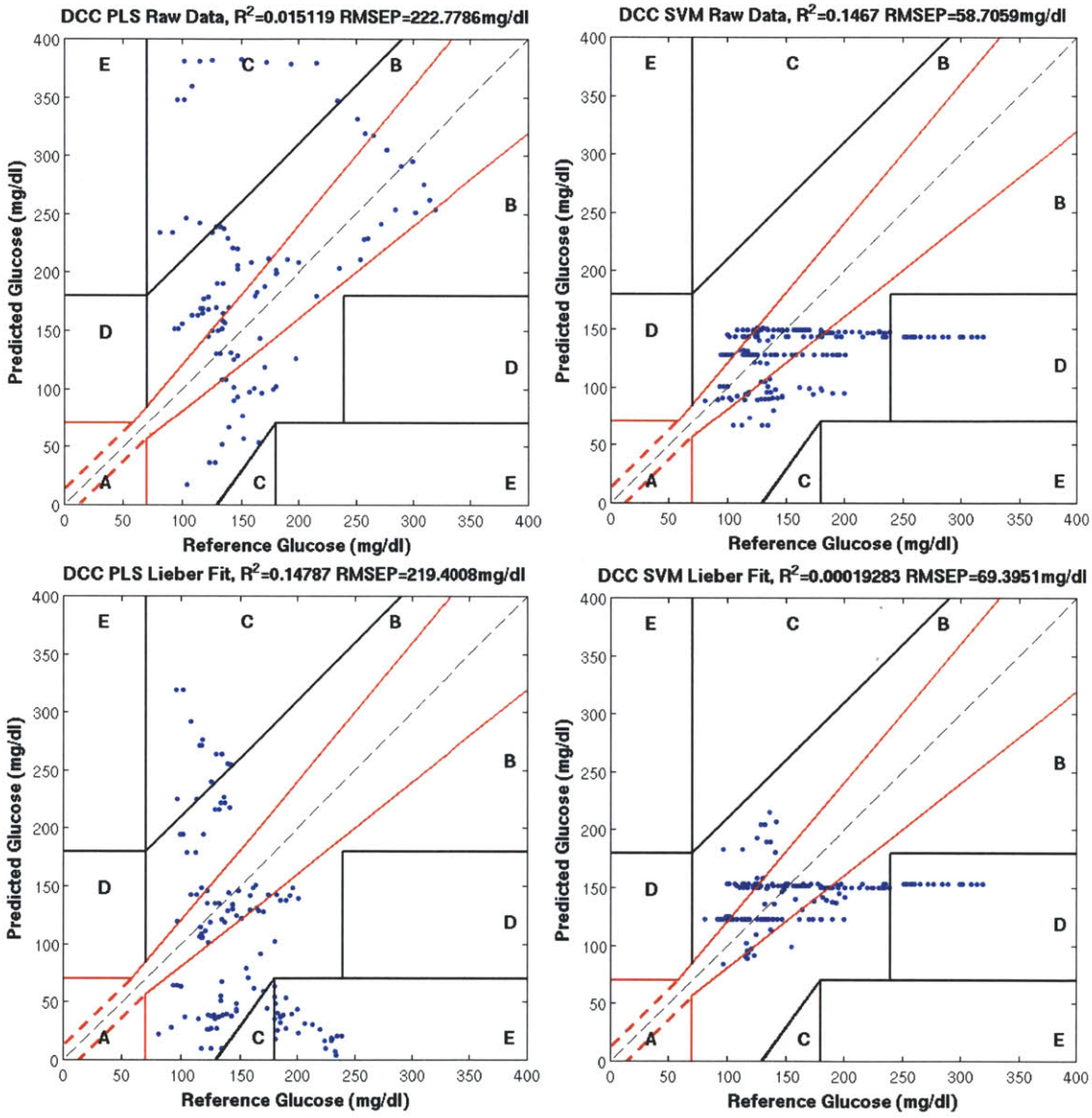

Figure 6-14: Prospective prediction performed with DCC on 5 human subjects. For each human subject, calibration performed on one set of OGTT data was used to predict on other sets of OGTT data obtained from the same subject on 2 to 5 different days. (The same data set as the previous figure.)

Raman spectroscopy instrument can measure glucose levels in a non-invasive manner while also satisfying the requirements and guidelines specified by the FDA and ISO. Finally, the study has revealed potential difficulty in prospective prediction on the same individual due to significant changes in the measurement site and conditions on different days. It has also shown that advanced non-linear regression techniques such as SVR should be approached with caution, as a calibration algorithm highly tailored to a particular calibration data set may become more vulnerable to non-glucose specific variations in prospective Raman spectra collected under different conditions. This problem may be alleviated by a precise control of skin measurement site and conditions by using a micro-manipulator and a pressure transducer, or by developing a miniaturized and wearable Raman glucose monitoring device which can be fixed on the same skin location with little change in measurement conditions.

THIS PAGE INTENTIONALLY LEFT BLANK

Chapter 7

Conclusion and future directions

7.1 Review of objectives and accomplishments

7.1.1 Address the issue of lag between blood and ISF glucose concentrations

In Chapter 3, the lag between blood and ISF glucose concentrations has been studied in detail. It has been noted that this lag between the two compartments during rapid changes in glucose levels could lead to calibration errors, arising from the inconsistencies between the Raman spectra (which probe the ISF glucose) and the reference blood glucose concentration. In addition, a solution to this problem has been presented by introducing the DCC algorithm, where the ISF and blood glucose concentrations were inter-converted using a first order diffusion model, based on the estimation of the direction and rate of change in glucose levels observed in two separate measurements. The validity of this model was confirmed by performing numerical simulations based on real blood and ISF glucose values measured during glucose clamping procedures. Finally, the uncertainty in the predicted glucose concentration was derived and quantified for both conventional and DCC-based calibration algorithms.

7.1.2 Design and construct a high-throughput and portable clinical Raman spectroscopy system

While the objectives of achieving high throughput and maintaining compact physical dimensions initially seemed conflicting, both goals were achieved by introducing the CHC for collecting Raman spectra in transmission mode. By converting back-scattered collection geometry to transmission mode, the excitation source was no longer on the same side as the collection fibers and significant improvement in optical fiber packing fraction (and thereby throughput) could be achieved. In addition, the CHC and its matching lens were designed to achieve the same performance as a very long CPC while maintaining much smaller physical dimensions.

7.1.3 Demonstrate clinical feasibility through human subject studies

The clinical instrument described in Chapter 5 was used successfully for collecting Raman spectra from human subjects undergoing OGTT. In Chapter 6, the Raman spectra and the blood glucose concentrations were used to develop a calibration model by both conventional PLS regression as well as nonlinear support vector regression techniques, which were both in turn performed on raw Raman spectra and autofluorescence-removed Raman spectra. Analyzing the calibration and leave-one-out cross-validation results showed that all four combinations performed better than the minimum requirements of FDA, while the best cross-validation performance was observed for the case of support vector regression (SVR) performed on raw spectra. However, prospective prediction on the same individual on a separate OGTT session conducted on a different day was less successful. It also revealed that while SVR had the lowest cross-validation errors, it was less robust against changes in measurement conditions compared with conventional PLS regression. Advanced non-linear regression techniques such as SVR should be approached with caution, as a calibration algorithm highly tailored to a particular calibration data set may become more vulnerable to non-glucose specific variations in prospective Raman spectra collected

under different conditions. This problem may be alleviated by a precise control of skin measurement site and conditions by using a micro-manipulator and a pressure transducer.

7.2 Future directions

Although this study has successfully demonstrated transdermal glucose measurement by Raman spectroscopy using calibration models developed from the same individual during the same OGTT session, prospective prediction on a different day was less successful. Moreover, transferring the calibration model across different individuals is even more difficult, due to person-to-person variations in skin tissue composition. However, the ability to non-invasively detect glucose concentration on the same individual after an invasive calibration session still provides tremendous benefits, as it can significantly reduce the total number of required figure-sticks. The current alternative would always require finger pricking or a subcutaneous glucose sensor implant. A future study could repeat the protocol outlined in this thesis with a much more rigorous control over measurement conditions, by employing micrometers and pressure transducers. A significant improvement in prospective prediction with the help of more rigorous control of measurement conditions would provide further confidence in the ability to measure glucose concentrations non-invasively from the same individual.

While a significant reduction in physical size has been achieved compared to the laboratory-based setup by developing a portable clinical Raman spectroscopy system, it is still far from being a hand-held device, which would be ideal for continuous glucose monitoring. Despite the invasive nature of implanting a needle-shaped sensor under the skin, the Medtronic Minimed and Abott Lab's FreeStyle Navigator could still be commercialized due to their small size. Therefore, the next goal would be to further reduce the size and complexity of the Raman spectroscopy instrument to bring the technology closer to practical use in the clinic. This would allow for the development of a miniaturized and wearable Raman glucose monitoring device,

which can be fixed on the same skin location with little change in measurement conditions to provide better prospective predictions. Studies are currently under way to identify the specific spectral wavenumbers that are most crucial for glucose detection. Successful identification of a small subset of spectral wavenumbers would enable the replacement of the bulky spectrograph and CCD with smaller and simpler optical filters and photodetectors.

Appendix A

List of abbreviations

Table A.1: List of abbreviations I

Abbreviation	Meaning
α	Effective glucose lag time constant
ANSI	American national standards institute
AR	Anti-reflection
$\mathbf{b}$	Regression vector
c_{BG}	Blood glucose concentration
c_{ISF}	ISF glucose concentration
CCD	Charge-coupled device
CHC	Compound hyperbolic concentrator
CNC	Computer numerical control
COUHES	Committee on the use of humans as test subjects
CPC	Compound parabolic concentrator
CR	Constrained regularization
CRC	Clinical research center
d_b	Distance to next boundary in multi-layer tissue simulation
DCC	Dynamic concentration correction
Δc_s	Uncertainty in concentration due to spectral overlap and noise
η	Spectral overlap (non-orthogonality) factor
FDA	US food and drug administration
$\texttt{Flag}_{Raman}$	Boolean value indicating if Raman scattering event has ocurred
g	Anisotropy factor
HLA	Hybrid linear analysis
ISO	International organization for standardization
ISF	Interstitial fluid
k_M	Glucose mass transfer coefficient (cm/s)
k_U	Rate of glucose uptake by cells (s^{-1})
μ_a	Absorption coefficient (cm^{-1})
μ_{Raman}	Raman scattering coefficient (cm^{-1})
μ_s	Scattering coefficient (cm^{-1})

Continued on the next page...

Table A.2: List of abbreviations II

Abbreviation	Meaning
MIR	Mid-infrared
NA	Numerical aperture
NADH	Reduced nicotinamide adenine dinucleotide
NAD(P)H	Reduced nicotinamide adenine dinucleotide phosphate
NIH	National institutes of health
NIR	Near infrared
OGTT	Oral glucose tolerance test
PCDCC	Pre-calibration dynamic concentration correction
PLS	Partial least squares
PPDCC	Post-prediction dynamic concentration correction
RMSECV	Root mean squared error of cross validation
RMSEP	Root mean squared error of prediction
$\mathbf{S}$	Matrix of Raman spectra
σ	Magnitude of noise in the Raman spectrum
SNR	Signal to noise ratio
SORS	Spatially offset Raman spectroscopy
SVM	Support vector machine
SVR	Support vector regression
θ_{max}	Maximum collimation half angle
ξ	Random number uniformly distributed from 0 to 1

THIS PAGE INTENTIONALLY LEFT BLANK

Appendix B

Optical fiber bundle for CHC-based transmission mode Raman spectroscopy setup

Customer: M.I.T

Part Number: 093293Customer

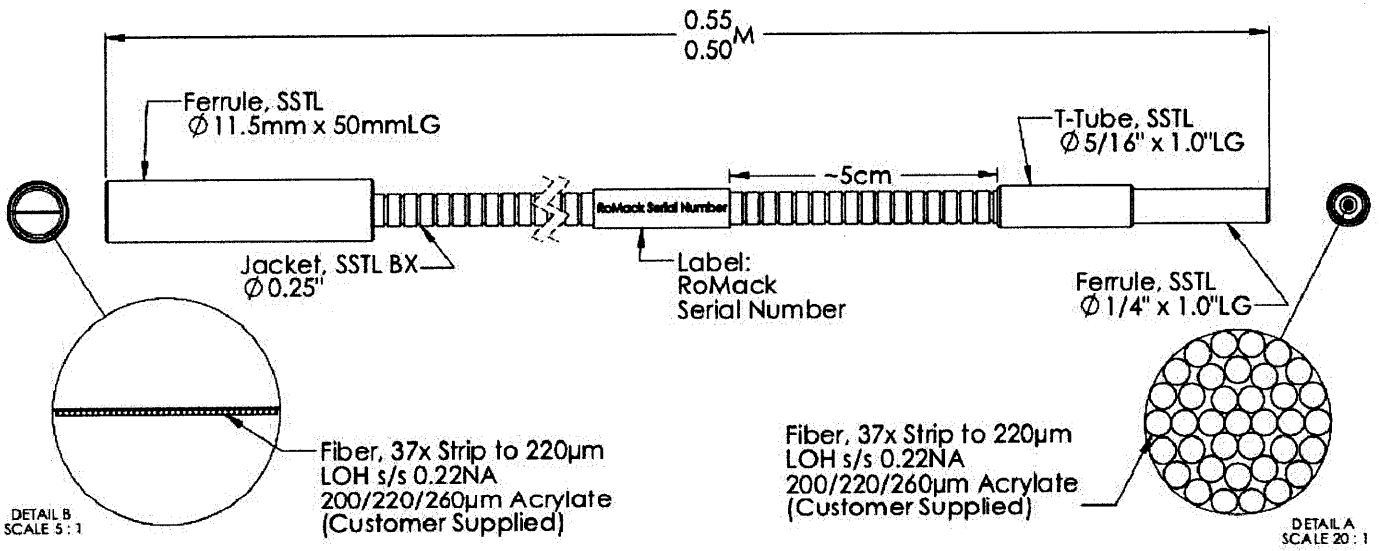

Notes:
- Fiber faces will be polished to a scratch-free finish at 40x Magnification.
- Non-Displaced and Non-Occluding cracks do not constitute a broken fiber.
- Maximum operating temperature of this assembly is +85°C.
- Minimum bend radius is 400x the individual fiber diameter for mutli- fiber assemblies.
- Entire Assembly built with Customer Supplied Loctite M-31CL Epoxy.

Stewart Barnett

Derick Scherberger

Signing this document signifies that it has been carefully reviewed in all aspects and can be used as a controlling document for the product depicted.

Customer: _____

RoMack Inc.
FIBEROPTICS FOR INDUSTRY AND RESEARCH
209 Bulifants Blvd., Williamsburg, VA 23188
PH: 757-258-4805 FAX: 757-258-4694
contact@romackfiberoptics.com

Appendix C

Selected relevant MATLAB codes used in the analysis

```
% Determine CPC length

function L = cpclength (acceptance_angle_degrees, input_radius)
L = input_radius.*(1+...
sind(acceptance_angle_degrees))./tand(acceptance_angle_degrees) ...
./sind(acceptance_angle_degrees);
end
```

```
% Draw CPC length vs angles

acceptance_angle_degrees = [0.1:0.01:30];
input_radius = 2;
L = cpclength (acceptance_angle_degrees, input_radius);
figure;
semilogy (acceptance_angle_degrees,L,'LineWidth',2)
xlabel ('\fontsize{12}\bf Maximum half angle (degrees)')
ylabel ('\fontsize{12}\bf CPC Length (mm)')
title (strcat(['\fontsize{12}\bf CPC Length at ', ...
    num2str(input_radius), ' mm minor aperture radius']))
 theta = 3.9
syms r;
index = find(eval(strcat(['round(acceptance_angle_degrees*100)/100 ...
    == ',num2str(theta)])));
z = L(index);
Max_Length = z
a = input_radius;
C = cosd (theta);
S = sind (theta);
P = 1+S;
Q = 1+P;
T = 1+Q;
cpc = C * r + 2 * ( C*S *z + a*P )*r + ( z^2 * S^2 - 2*a*C*Q*z - a^2 ...
    * P*T );
large_aperture_radius = eval(solve (cpc))
```

```
% CHC design tool

function [xa1,ya1,fxa1,fya1,xb1,yb1,fxb1,fyb1, ...
r_input_aperture,r_output_aperture,acceptance_angle] ...
= CHC(a,b,xmax,ymax,rotation_angle)
[xa1,ya1,fxa1,fya1,xa2,ya2,fxa2,fya2] = ...
    hyperbola(a,b,xmax,ymax,rotation_angle,0,0);
[xb1,yb1,fxb1,fyb1,xb2,yb2,fxb2,fyb2] = ...
    hyperbola(a,b,xmax,ymax,-180-rotation_angle,0,0);

%% shift in x-direction to align foci
[xa1,ya1] = turn(xa1,ya1,0,-fxa1,0);
[xa2,ya2] = turn(xa2,ya2,0,-fxa1,0);
[fxa2,fya2] = turn(fxa2,fya2,0,-fxa1,0);
[fxa1,fya1] = turn(fxa1,fya1,0,-fxa1,0);
[xb1,yb1] = turn(xb1,yb1,0,-fxb1,0);
[xb2,yb2] = turn(xb2,yb2,0,-fxb1,0);
[fxb2,fyb2] = turn(fxb2,fyb2,0,-fxb1,0);
[fxb1,fyb1] = turn(fxb1,fyb1,0,-fxb1,0);

%% determine how much to shift in y-direction to have foci aligned
[zero, origin_index] = min (abs(xa1));
ya1_offset = -(((ya1(origin_index)-fyb1)^2)^0.5)/2;
yb1_offset = -ya1_offset;

%% shift in y-direction to align foci
[xa1,ya1] = turn(xa1,ya1,0,-fxa1,ya1_offset);
[xa2,ya2] = turn(xa2,ya2,0,-fxa1,ya1_offset);
[fxa2,fya2] = turn(fxa2,fya2,0,-fxa1,ya1_offset);
[fxa1,fya1] = turn(fxa1,fya1,0,-fxa1,ya1_offset);
[xb1,yb1] = turn(xb1,yb1,0,-fxb1,yb1_offset);
[xb2,yb2] = turn(xb2,yb2,0,-fxb1,yb1_offset);
[fxb2,fyb2] = turn(fxb2,fyb2,0,-fxb1,yb1_offset);
[fxb1,fyb1] = turn(fxb1,fyb1,0,-fxb1,yb1_offset);

%% Measure CHC length
```

```
35 index_limit = max(find (xa1 < fxa2));
36 slope = (fyb2 - fya1) / (fxb2 - fxa1);
37 extreme_ray1 = slope.*xa1(1:index_limit) + fya1;
38 slope = (fyb1 - fya2) / (fxb1 - fxa2);
39 extreme_ray2 = slope.*xa1(1:index_limit) + fyb1;
40 [zero, length_index_a] = min(abs(extreme_ray1 - ya1(1:index_limit)));
41 [zero, length_index_b] = min(abs(extreme_ray2 - yb1(1:index_limit)));
42 edge_xa = xa1(length_index_a);
43 edge_ya = ya1(length_index_a);
44 edge_xb = edge_xa;
45 edge_yb = -edge_ya;
46 CHC_length = abs(edge_xa);
47
48 %% Measure aperture
49 r_input_aperture = fya1;
50 r_output_aperture = abs(edge_ya);
51
52 %% Determine acceptance angle
53 output_center = [edge_xa, 0];
54 slope = (fyb2 - output_center(2)) / (fxb2 - output_center(1));
55 acceptance_angle_line1 = slope.*xa1(1:index_limit) - ...
       slope*output_center(1);
56 slope = (fya2 - output_center(2)) / (fxa2 - output_center(1));
57 acceptance_angle_line2 = slope.*xa1(1:index_limit) - ...
       slope*output_center(1);
58 acceptance_angle = atand((fyb2 - output_center(2))/(fxa2 - ...
       output_center(1)));
59 f = abs(fxb2 - output_center(1));  % focal length of lens
60
61 %% Draw figure
62 figure;hold on;plot(xa1, ya1);plot(xa2, ya2, ':'); % hyperbola ...
       conjugate pair a1 and a2
63 plot([fxa1 fxa2],[fya1 fya2],'.');line([fxa1 fxa2],[fya1 ...
       fya2],'LineStyle',':')   % conjugate foci fa1 and fa2
64 plot(xb1, yb1, 'r');plot(xb2, yb2, ':r');  % hyperbola conjugate ...
       pair b1 and b2
```

```
65 plot([fxb1 fxb2],[fyb1 fyb2],'.r'); line([fxb1 fxb2],[fyb1 ...
       fyb2],'Color','r','LineStyle',':'); % conjugate foci fb1 and fb2
66 line([fxa1 fxb1],[fya1 fyb1],'Color','k')  % input aperture
67 plot(xa1(1:index_limit), extreme_ray1, ...
       ':k');plot(xa1(1:index_limit), extreme_ray2, ':k');
68 plot([edge_xa edge_xb],[edge_ya edge_yb],'.k'); % output aperture
69 line([edge_xa edge_xb],[edge_ya edge_yb],'Color','k')
70 plot(xa1(1:index_limit), acceptance_angle_line1, ...
       ':m');plot(xa1(1:index_limit), acceptance_angle_line2, ':m');
71 title({['Inputs: A=', num2str(a), ', B=', num2str(b), ', ...
       \theta_r_o_t=',num2str(rotation_angle),'deg :'];
72 ['R_i=',num2str(r_input_aperture),'mm', ', ...
       R_o=',num2str(r_output_aperture),'mm', ', ...
73 L=',num2str(CHC_length),'mm',', ...
       \theta_a_c_p_t=',num2str(acceptance_angle),'deg',', ...
       f=',num2str(f),'mm']})
74 axis([-xmax xmax -ymax ymax]) % specify axis limits
75 xlabel('x (mm)')
76 ylabel('y (mm)')
```

```
1  % Form hyperbola with set rotation angle and offset
2
3  function [x1out,y1out, fx1out,fy1out, x2out,y2out, fx2out,fy2out] = ...
       hyperbola(a,b,xmax, ymax, rotation_angle, xoffset,yoffset)
4
5  % Program to plot the hyperbola
6  % y^2/a^2 - x^2/b^2 = 1
7  x = linspace(-xmax,xmax,1001);
8  y=sqrt(((x.^2)./(b^2)+1).*a^2); % corresponding y values
9  x1 = x; y1 = y;
10 x2 = x; y2 = -y;
11
12 %% foci
13 fx1 = 0;
14 fy1 = sqrt(a.^2+b.^2);
```

```
fx2 = 0;
fy2 = -(sqrt(a.^2+b.^2));

%% Rotation
[x1out,y1out] = turn(x1,y1,rotation_angle,xoffset,yoffset);
[x2out,y2out] = turn(x2,y2,rotation_angle,xoffset,yoffset);
[fx1out,fy1out] = turn(fx1,fy1,rotation_angle,xoffset,yoffset);
[fx2out,fy2out] = turn(fx2,fy2,rotation_angle,xoffset,yoffset);
```

```
function [xout,yout] = turn(xin,yin,theta,x_offset,y_offset)

% Program to rotate and translate x,y values from x",y" to x,y space.
% theta value in degrees.

%  rotation matrix
xfm = [cosd(theta) sind(theta); ...
       -sind(theta) cosd(theta)];
% make x,y values into a column vector
r_in = [xin; yin];
% rotate
r_out = xfm*r_in;
x = r_out(1,:); y = r_out(2,:);
xout = x + x_offset;
yout = y + y_offset;
```

```
%% Perform OGTT data analysis
load_data_20110119
low_glucose = round(min(c) - 10);
high_glucose = round(max(c) + 10);

% PLS Raw Data
pred_title_pls = 'PLS Raw Data';

% Collapse: Take the mean of all frames
```

```
mean_spectra = [];
for q=1:datapoints
    if n(q)<10
       zerolabel = '_00';
    elseif (10≤n(q) && n(q)<100)
       zerolabel = '_0';
    else
       zerolabel = '_';
    end
  mean_spectra = [mean_spectra; eval((strcat('mean (',dataname, ...
      zerolabel, num2str(n(q)), ''')')))]; % Raw
  eval(strcat(['clear ', dataname], zerolabel, num2str(n(q))));
end
figure;plot(mean_spectra', 'LineWidth', 0.5);

%% Leave one out cross validation)
[raw_datapoints, raw_pixels] = size (mean_spectra);
mean_spectra_sub = mean_spectra - ...
    (min(mean_spectra'))'*(ones(raw_pixels,1))';
scale_factor = ones(raw_pixels,1)*max(mean_spectra_sub');
mean_spectra_scaled =  mean_spectra_sub ./ scale_factor' ; % scale : ...
    0 to 1
figure;plot(mean_spectra_scaled');
Preds = candp(mean_spectra_scaled,c,20,100,1340,1,[ ],[1:size(c,1)]);
figure;rp_raw=rplot(c,Preds);
% lv1 = input('# of loading vectors? : ');
lv1=5;
pred_pls = Preds(:,lv1+1);
[b, w, v, MeanA, MeanC] = ...
    plscalib_ck(mean_spectra_scaled(:,100:1340), c, lv1+1);      %%%%%
b_pls_raw = b;
w_pls_raw = w;
v_pls_raw = v;
MeanA_raw = MeanA;
pred_pls = nonneg(pred_pls);
R2_pls = (corr (c, pred_pls))^2
```

```
42 rmsep_pls=rmsep(pred_pls,c)
43 plot_prediction (c,pred_pls, R2_pls, rmsep_pls, pred_title_pls, ...
       time_step, datapoints, low_glucose, high_glucose)
44
45 %% PLS Lieber Fit
46 pred_title_lieber = 'PLS Lieber Fit';
47
48 % Truncated and Lieber-fit Background removed
49 mean_spectra_lieber = [];
50 for i=1:datapoints
51   mean_spectra_lieber = [mean_spectra_lieber; ...
         lieberfit(mean_spectra(i,180:840), 5, 500)];
52 end
53 [lieber_datapoints, lieber_pixels] = size (mean_spectra_lieber);
54 scale_factor = ones(lieber_pixels,1)*max(mean_spectra_lieber');
55 mean_spectra_lieber_scaled =  mean_spectra_lieber ./ scale_factor' ; ...
       % scale : 0 to 1
56 figure; plot(mean_spectra_lieber_scaled');
57 % PLS analysis (Leave one out cross validation)
58 Preds_lieber = candp(mean_spectra_lieber_scaled,c,20,1,661,1,[ ...
       ],[1:size(c,1)]);
59 figure;rp_raw_lieber=rplot(c,Preds_lieber);
60 %lv2 = input('# of loading vectors? : ');
61 lv2=5;
62 pred_lieber = Preds_lieber(:,lv2+1);
63 [b, w, v, MeanA, MeanC] = plscalib_ck(mean_spectra_lieber_scaled, c, ...
       lv2+1);    %%%%%
64 b_pls_lieber = b
65 w_pls_lieber = w;
66 v_pls_lieber = v;
67 MeanA_lieber = MeanA;
68 pred_lieber = nonneg(pred_lieber);
69 R2_lieber = (corr (c, pred_lieber))^2
70 rmsep_lieber = rmsep(pred_lieber,c)
71 plot_prediction (c,pred_lieber, R2_lieber, rmsep_lieber, ...
       pred_title_lieber, time_step, ...
```

```
72  datapoints, low_glucose, high_glucose)
73
74  %% SVM Raw
75  pred_title_svm_raw = 'SVM Raw'
76  libsvm_format (c, mean_spectra_scaled, 'svm_raw.txt')
77  [ty_raw, tx_raw] = libsvmread('svm_raw.txt');
78  % Leave one out cross validation
79  p_svm_raw = zeros(datapoints,1);
80  for i=1:datapoints
81      if i==1
82          LOO_spectra = tx_raw(2:datapoints,:);
83          LOO_c = c(2:datapoints);
84      else
85          LOO_spectra = [tx_raw(1:i-1,:);tx_raw(i+1:datapoints,:)];
86          LOO_c = [c(1:i-1); c(i+1:datapoints)];
87      end
88      m_raw = svmtrain(LOO_c, LOO_spectra, '-s 3 -c 1048576.0 -g ...
            0.00238106 -p 0.000195312');
89      p_svm_raw(i) = svmpredict(c(i), tx_raw(i,:), m_raw);
90  end
91  rmsep_svm_raw = ((p_svm_raw-c)'*(p_svm_raw-c)/datapoints)^0.5
92  R2_svm_raw = (corr (c, p_svm_raw))^2
93  rmsep_svm_raw = rmsep(p_svm_raw,c)
94  plot_prediction (c,p_svm_raw, R2_svm_raw, rmsep_svm_raw, ...
       pred_title_svm_raw, time_step, ...
95   datapoints, low_glucose, high_glucose)
96
97  %% SVM Lieber
98  pred_title_svm_lieber = 'SVM Lieber';
99  libsvm_format (c, mean_spectra_lieber_scaled, 'svm_lieber.txt')
100 [ty, tx] = libsvmread('svm_lieber.txt');
101 % Leave one out cross validation
102 p_svm_lieber = zeros(datapoints,1);
103 for i=1:datapoints
104     if i==1
105         LOO_spectra = tx(2:datapoints,:);
```

```
106         LOO_c = c(2:datapoints);
107     else
108         LOO_spectra = [tx(1:i-1,:);tx(i+1:datapoints,:)];
109         LOO_c = [c(1:i-1); c(i+1:datapoints)];
110     end
111     m_lieber = svmtrain(LOO_c, LOO_spectra, '-s 3 -c 1048576.0 -g ...
            0.0012 -p 0.0717936');
112     p_svm_lieber(i) = svmpredict(c(i), tx(i,:), m_lieber);
113 end
114 rmsep_svm_lieber = ((p_svm_lieber-c)'*(p_svm_lieber-c)/datapoints)^0.5
115 R2_svm_lieber = (corr (c, p_svm_lieber))^2
116 rmsep_svm_lieber = rmsep(p_svm_lieber,c)
117 plot_prediction (c,p_svm_lieber, R2_svm_lieber, rmsep_svm_lieber, ...
       pred_title_svm_lieber, time_step, ...
118  datapoints, low_glucose, high_glucose)
119
120 %% DCC PLS Raw
121 [alpha_opt_raw, LV_model_opt, b_model_opt, c_ISF_calib_trans_opt] = ...
       dcc_pls_calib(mean_spectra_scaled,...
122  100, 1340, t, c, 0.1);
123 b_dcc_pls_raw = b_model_opt;
124 pred_title_dcc_pls = 'DCC PLS Raw';
125 p_dcc_pls = zeros(datapoints,1);
126 for i=1:datapoints
127     if i==1
128         LOO_spectra = mean_spectra_scaled(2:datapoints,:);
129         LOO_c = c(2:datapoints);
130         LOO_t = t(2:datapoints);
131     else
132         LOO_spectra = ...
                [mean_spectra_scaled(1:i-1,:);mean_spectra_scaled(i+1:datapoints,:)];
133         LOO_c = [c(1:i-1); c(i+1:datapoints)];
134         LOO_t = [t(1:i-1); t(i+1:datapoints)];
135     end
136     [alpha_opt_raw_LOO, LV_model_opt_LOO, b_model_opt_LOO, ...
           c_ISF_calib_trans_opt_LOO] = ...
```

```
137 dcc_pls_calib(LOO_spectra, 100, 1340, LOO_t, LOO_c, 0.2);
138     if i==1
139         p_dcc_pls(i) = c(1);
140     else
141     p_dcc_pls(i) = dcc_pls_predict(mean_spectra_scaled(i-1:i,:), ...
           100, 1340, LOO_spectra, ...
142 b_model_opt_LOO, alpha_opt_raw_LOO, c_ISF_calib_trans_opt_LOO, ...
       t(i-1:i));
143     end
144 end
145 rmsep_dcc_pls = ((p_dcc_pls-c)'*(p_dcc_pls-c)/datapoints)^0.5;
146 R2_dcc_pls = (corr (c, p_dcc_pls))^2
147 plot_prediction (c,p_dcc_pls, R2_dcc_pls, rmsep_dcc_pls, ...
       pred_title_dcc_pls, time_step, ...
148 datapoints, low_glucose, high_glucose)
149
150 %% DCC PLS Lieber Fit
151 [z,l] = size(mean_spectra_lieber_scaled);
152 [alpha_opt_lieber, LV_model_opt_lieber, b_model_opt_lieber, ...
       c_ISF_calib_trans_opt_lieber] = ...
153 dcc_pls_calib(mean_spectra_lieber_scaled, 1, l, t, c, 0.1);
154 b_dcc_pls_lieber = b_model_opt_lieber;      %%%%%
155 pred_title_dcc_pls_lieber = 'DCC PLS Lieber Fit';
156 p_dcc_pls_lieber = zeros(datapoints,1);
157 for i=1:datapoints
158     if i==1
159         LOO_spectra = mean_spectra_lieber_scaled(2:datapoints,:);
160         LOO_c = c(2:datapoints);
161         LOO_t = t(2:datapoints);
162     else
163         LOO_spectra = [mean_spectra_lieber_scaled(1:i-1,:);
164         mean_spectra_lieber_scaled(i+1:datapoints,:)];
165         LOO_c = [c(1:i-1); c(i+1:datapoints)];
166         LOO_t = [t(1:i-1); t(i+1:datapoints)];
167     end
168     [alpha_opt_lieber_LOO, LV_model_opt_LOO, b_model_opt_LOO, ...
```

```
        c_ISF_calib_trans_opt_lieber_LOO] = ...
dcc_pls_calib(LOO_spectra, 1, 661, LOO_t, LOO_c, 0.2);
    if i==1
        p_dcc_pls_lieber(i) = c(1);
    else
    p_dcc_pls_lieber(i) = ...
        dcc_pls_predict(mean_spectra_lieber_scaled(i-1:i,:), 1, 661, ...
        LOO_spectra, ...
b_model_opt_LOO, alpha_opt_lieber_LOO, ...
    c_ISF_calib_trans_opt_lieber_LOO, t(i-1:i));
    end
end
rmsep_dcc_pls_lieber = ...
    ((p_dcc_pls_lieber-c)'*(p_dcc_pls_lieber-c)/datapoints)^0.5;
R2_dcc_pls_lieber = (corr (c, p_dcc_pls_lieber))^2
plot_prediction (c,p_dcc_pls_lieber, R2_dcc_pls_lieber, ...
    rmsep_dcc_pls_lieber, pred_title_dcc_pls_lieber, ...
 time_step, datapoints, low_glucose, high_glucose)

%% DCC SVM Raw
pred_title_dcc_svm_raw = 'DCC SVM Raw'
libsvm_format (c_ISF_calib_trans_opt, mean_spectra_scaled, ...
    'svm_dcc_raw.txt')
[ty_dcc_raw, tx_dcc_raw] = libsvmread('svm_dcc_raw.txt');

%% Leave one out cross validation
p_isf_dcc_svm_raw = zeros(datapoints,1);
for i=1:datapoints
    if i==1
        LOO_spectra = tx_dcc_raw(2:datapoints,:);
        LOO_c = c_ISF_calib_trans_opt(2:datapoints);
    else
        LOO_spectra = ...
            [tx_dcc_raw(1:i-1,:);tx_dcc_raw(i+1:datapoints,:)];
        LOO_c = [c_ISF_calib_trans_opt(1:i-1); ...
            c_ISF_calib_trans_opt(i+1:datapoints)];
```

```
196     end
197     m_dcc_raw = svmtrain(LOO_c, LOO_spectra, '-s 3 -c 1048576 -g ...
            10.73213196615 -p 0.0018223300616');
198     p_isf_dcc_svm_raw(i) = svmpredict(c_ISF_calib_trans_opt(i), ...
            tx_dcc_raw(i,:), m_dcc_raw);
199 end
200 % 1048576.0, g=7.46426393229, p=0.0018223300616
201 p_dcc_svm_raw = p_isf_dcc_svm_raw(2:end) + ...
        alpha_opt_raw*diff(p_isf_dcc_svm_raw)./diff(t);
202 p_dcc_svm_raw = [c(1);p_dcc_svm_raw];
203 rmsep_dcc_svm_raw = ...
        ((p_dcc_svm_raw-c)'*(p_dcc_svm_raw-c)/datapoints)^0.5
204 R2_dcc_svm_raw = (corr (c, p_dcc_svm_raw))^2
205 plot_prediction (c,p_dcc_svm_raw, R2_dcc_svm_raw, rmsep_dcc_svm_raw, ...
        pred_title_dcc_svm_raw, time_step, ...
206 datapoints, low_glucose, high_glucose)
207
208 %% DCC SVM Lieber
209 pred_title_dcc_svm_lieber = 'DCC SVM Lieber'
210 libsvm_format (c_ISF_calib_trans_opt, mean_spectra_lieber_scaled, ...
        'svm_dcc_lieber.txt')
211 [ty_dcc_liber, tx_dcc_lieber] = libsvmread('svm_dcc_lieber.txt');
212
213 %% Leave one out cross validation
214 p_isf_dcc_svm_lieber = zeros(datapoints,1);
215 for i=1:datapoints
216     if i==1
217         LOO_spectra = tx_dcc_lieber(2:datapoints,:);
218         LOO_c = c_ISF_calib_trans_opt(2:datapoints);
219     else
220         LOO_spectra = ...
                [tx_dcc_lieber(1:i-1,:);tx_dcc_lieber(i+1:datapoints,:)];
221         LOO_c = [c_ISF_calib_trans_opt(1:i-1); ...
                c_ISF_calib_trans_opt(i+1:datapoints)];
222     end
223     m_dcc_lieber = svmtrain(LOO_c, LOO_spectra, '-s 3 -c 1048576.0 ...
```

```
        -g 42.8 -p 0.00023683');
224     p_isf_dcc_svm_lieber(i) = svmpredict(c_ISF_calib_trans_opt(i), ...
            tx_dcc_lieber(i,:), m_dcc_lieber);
225 end
226 p_dcc_svm_lieber = p_isf_dcc_svm_lieber(2:end) + ...
        alpha_opt_lieber*diff(p_isf_dcc_svm_lieber)./diff(t);
227 p_dcc_svm_lieber = [c(1);p_dcc_svm_lieber];
228 rmsep_dcc_svm_lieber = ...
        ((p_dcc_svm_lieber-c)'*(p_dcc_svm_lieber-c)/datapoints)^0.5
229 R2_dcc_svm_lieber = (corr (c, p_dcc_svm_lieber))^2
230 plot_prediction (c,p_dcc_svm_lieber, R2_dcc_svm_lieber, ...
        rmsep_dcc_svm_lieber, pred_title_dcc_svm_lieber, ...
231  time_step, datapoints, low_glucose, high_glucose)
```

```
1  function[b, w, v, MeanA, MeanC] = PLSCALIB_CK(Spectra, Concs, LoadNum)
2
3  % Modified by Chae-Ryon Kong from PLSCALIB
4  % Spectra is the matrix of spectral values as they are to be used
5  %  by the routine.  Each spectrum occupies one ROW (horizontal ...
       direction).
6  % Concs are the concentrations of the prediction analyte in each sample.
7  % LoadNum is the number of loading vectors to use.
8  %
9  % Output:
10 %      w is the matrix of weight vectors, with each COLUMN one vector.
11 %      b is the matrix of loading vectors,  "    "   "   "   ".
12 %      v is a column vector of score coefficients.
13 %      MeanA is the average spectrum.
14 %      MeanC is the average concentration.
15
16 w=[]; b=[]; v=[]; MeanA=[]; MeanC=[]; tt=[];
17
18 %STEP 1: PREPROCESSING
19 MeanA=mean(Spectra);
20 A = Spectra- ones(size(Spectra,1), 1)*MeanA;
```

```
MeanC=mean(Concs);
c = Concs-MeanC;
h=1;

%LOOP
while (h≤LoadNum)
 %STEP 2: FORM WEIGHT VECTOR AND NORMALIZE IT
  x=(A'*c)/(c'*c);
  w=[w,x/sqrt(x'*x)];
 %STEP 3: FORM LATENT SCORE VECTOR
    t=A*w(:,h);
    %compute sum of squares here, since it's used twice later
     tt=t'*t;
  %STEP 4: RELATE SCORE VECTOR TO CONCENTRATIONS
  v=[v;(t'*c)/tt];
  %STEP 5: FORM B, THE PLS LOADING VECTOR
  b=[b,((A'*t)/tt)];
  %STEP 6: CALCULATE RESIDUALS
  A=A-t*b(:,h)';
  c=c-v(h)*t;
  %STEP 7: INCREMENT AND LOOP BACK
  h=h+1;
end;
```

```
function c=PLSPRED_CK(Spectra, LoadNum, w, b, v, MeanA, MeanC)
% Modified by Chae-Ryon Kong from PLSPRED
% Spectra is a matrix of prediction spectra, with each spectrum
% occupying one ROW.
% LoadNum is the maximum number of loading vectors to use.

%Output:
%     c : concentration predictions.
%         The nth column is the predictions achieved using n-1 ...
    loading vectors
%          (the first column is the average concentration of the ...
```

```
    calibration set).

%STEP 1: PREPROCESSING
NumofSpectra=size(Spectra,1);
A = Spectra- ones(NumofSpectra, 1)*MeanA;
c = ones(NumofSpectra,1)*MeanC;
h=1;

%LOOP
while (h<=LoadNum)

  %STEP 2: CALCULATE SCORE VECTOR
  t=A*w(:,h);

  %STEP 3: UPDATE CONCENTRATION PREDICTIONS
  % add to the previous column
  c=[c, c(:,h) + t*v(h)];

  %STEP 4: CREATE RESIDUAL
  A=A-t*(b(:,h))';

  %STEP 5: LOOP BACK
  h=h+1;
end;
```

```
%% Load OGTT data for 01-19-2011
concs = load ('concs_20110119.txt');
filename = 'Thenar_1sec_60fr';
dataname = 'Thenar_20110119';
time_step = 5;
frames = 60;
remove_datapoint = 0; % ***  Remove one data point for missing ...
    spectrum. 0 for none.
t_r = concs(:,1);
c_r = concs(:,2);
```

```
10 t = interp(t_r,2);
11 % c = interp(c_r,2);
12 c = interp1 (t_r, c_r, t, 'linear', 'extrap');
13 c = c(1:end-1);
14 t = t(1:end-1);
15 datapoints = size(c,1);
16 n=0:time_step:(datapoints-1)*time_step; % starting from 0
17 n=n(:);
18 % n=time_step:time_step:datapoints*time_step % not starting from 0
19 if (remove_datapoint == 1)
20     t = [t(2:datapoints)];
21     c = [c(2:datapoints)];
22     n = [n(2:datapoints)];
23 elseif (remove_datapoint > 1)
24     t = [t(1:remove_datapoint-1);t(remove_datapoint+1:datapoints)];
25     c = [c(1:remove_datapoint-1);c(remove_datapoint+1:datapoints)];
26     n = [n(1:remove_datapoint-1);n(remove_datapoint+1:datapoints)];
27 end
28 datapoints = size(c,1);
29 figure; plot (t,c, 'o');
30 set(gca, 'fontsize', 14) ;
31 set(findobj('Type', 'line'), 'LineWidth', 2)
32 axis([0 time_step*datapoints 80 230])
33 xlabel ('Time (min)', 'fontsize', 14, 'fontweight', 'bold')
34 ylabel ('Glucose (mg/dl)', 'fontsize', 14, 'fontweight', 'bold')
35 title ('Glucometer Readings','fontsize', 16, 'fontweight', 'bold')
36
37 %% cosmic ray removal and extracting frames
38 for q=1:datapoints
39    if n(q)<10
40       zerolabel = '_00';
41    elseif (10≤n(q) && n(q)<100)
42       zerolabel = '_0';
43    else
44       zerolabel = '_';
45    end
```

```
46      eval(strcat(['load ', filename], zerolabel, num2str(n(q)), '.txt;'))
47      eval(strcat(dataname, zerolabel, num2str(n(q)), ' = [];'));
48      for k=1:frames
49          eval(strcat(dataname, zerolabel, num2str(n(q)), ' = [', ...
                dataname, zerolabel, num2str(n(q)), ', cosmic_remove(', ...
                filename,zerolabel, num2str(n(q)), ...
                '(',num2str(1+1340*(k-1)), ':', num2str(1340*k), ',4))];'));
50      end
51      eval(strcat(['clear ', filename], zerolabel, num2str(n(q))))
52  end
```

```
1  % Remove cosmic rays and hot pixel artifacts
2  function[output] = cosmic_remove(raw_spectrum, varargin)
3  % function[output] = cosmic_remove(raw_spectrum, thresh)
4  % output = output spectrum with cosmic rays removed
5  % thresh (Optional) = minimum spike height to be treated as cosmic ray
6  %       (default: thresh = 1000)
7  raw_spectrum = raw_spectrum (:);
8  output = raw_spectrum;
9  L_s = length (raw_spectrum);
10 filtered = medfilt1(raw_spectrum,15);
11 spikes = raw_spectrum - filtered;
12 if (length (varargin) == 1)
13     threshold = varargin{1};
14 else
15     threshold = 1500;
16 end
17 ind = [];
18 ind = find(abs(spikes)>threshold);
19 L = length(ind);
20 if (L==0)
21     return
22 else
23     for i=1:L
24         output (ind(i)) = filtered (ind(i));
```

```
25          if (ind(i)>3)
26              output (ind(i)-3) = filtered (ind(i)-3);
27              output (ind(i)-2) = filtered (ind(i)-2);
28              output (ind(i)-1) = filtered (ind(i)-1);
29          end
30          if (ind(i)>2)
31              output (ind(i)-2) = filtered (ind(i)-2);
32              output (ind(i)-1) = filtered (ind(i)-1);
33          end
34          if (ind(i)==2)
35              output (ind(i)-1) = filtered (ind(i)-1);
36          end
37          if (ind(i)<(L_s-2))
38              output (ind(i)+1) = filtered (ind(i)+1);
39              output (ind(i)+2) = filtered (ind(i)+2);
40              output (ind(i)+2) = filtered (ind(i)+2);
41          end
42          if (ind(i)<(L_s-1))
43              output (ind(i)+1) = filtered (ind(i)+1);
44              output (ind(i)+2) = filtered (ind(i)+2);
45          end
46          if (ind(i)<L_s)
47              output (ind(i)+1) = filtered (ind(i)+1);
48          end
49      end
50  end
```

```
1  function [vector] = nonneg(vector)
2
3  L = length (vector)
4  for k=1:L
5      if (vector(k)<0)
6          vector(k) = 0;
7      end
8  end
```

```
function [] = plot_prediction (c,pred_val, R2, rmsep_val, ...
    pred_title, time_step, datapoints, low, high)
% [] = plot_prediction (c,pred_val, R2, rmsep_val, pred_title)
figure;h=plot([time_step:time_step:time_step*datapoints], pred_val, ...
    'X', [time_step:time_step:time_step*datapoints], c, 'o', ...
    'MarkerSize', 10, 'linewidth', 2);
legend('Predicted', 'Glucometer');
set(gca, 'fontsize', 14) ;
axis([0 time_step*datapoints low high])
xlabel ('Time (min)', 'fontsize', 14, 'fontweight', 'bold')
ylabel ('Glucose (mg/dl)', 'fontsize', 14, 'fontweight', 'bold')
title (pred_title,'fontsize', 16, 'fontweight', 'bold')
figure; [A, B] =ega_mgdl(c, pred_val);title ([pred_title,', R^2=', ...
    num2str(R2), ' RMSEP=', num2str(rmsep_val),'mg/dl'], 'fontsize', ...
    14, 'fontweight', 'bold')
```

```
function [total, percentage] = ega_mgdl(y,yp)
% Plot Clarke Error Grid and perform analysis
% [total, percentage] = ega_mgdl(y,yp)
%
% Inputs:
% y = reference values (mg/dl)
% yp = predicted/estimtated values (mg/dl)
%
% Outputs:
% total = total points per zone:
% total(1) = zone A,
% total(2) = zone B, and so on
% percentage = percentage of data which fell in certain region:
% percentage(1) = zone A,
% percentage(2) = zone B, and so on.
%
% Modified by Chae-Ryon Kong from original code by
% Edgar Guevara Codina
% codina@REMOVETHIScactus.iico.uaslp.mx
```

```
% ...
    ------------------------------------------------------------------------

% Error checking
if nargin==0
 error('clarke:Inputs','There are no inputs.')
end
if length(yp) ~= length(y)
    error('clarke:Inputs','Vectors y and yp must be the same length.')
end
% if (max(y) > 400) || (max(yp) > 400) || (min(y) < 0) || (min(yp) < 0)
%     error('clarke:Inputs','Vectors y and yp are not in the ...
    physiological range of glucose (<400mg/dl).')
% end
% ---------------------- Determine Screen Size ...
    ---------------------------------

scrsz = get(0,'ScreenSize')-[0 -5 0 72];
% ---------------------- Determine data length ...
    ---------------------------------

n = length(y);
% ---------------------- Plot Clarke's Error Grid ...
    ---------------------------------

h = ...
    plot(y,yp,'ko','MarkerSize',4,'MarkerFaceColor','b','MarkerEdgeColor','b');
xlabel('Reference Glucose (mg/dl)','fontsize', 14, 'fontweight', ...
    'bold');
ylabel('Predicted Glucose (mg/dl)','fontsize', 14, 'fontweight', ...
    'bold');
title('Clarke Error Grid','fontsize', 14, 'fontweight', 'bold');
set(gca,'XLim',[0 400],'fontsize', 14);
set(gca,'YLim',[0 400],'fontsize', 14);
axis square
hold on
plot([0 400],[0 400],'k--')                    % Theoretical 45 degree ...
    regression line
plot([0 70/1.2],[70 70],'r-', 'linewidth',2)
plot([70/1.2 400/1.2],[70 400],'r-', 'linewidth',2)
```

```
plot([70 70],[70*1.2 400],'k-', 'linewidth',2)
plot([0 70],[180 180],'k-', 'linewidth',2)
plot([70 290],[180 400],'k-', 'linewidth',2)                % ...
    Corrected upper B-C boundary
plot([70 70],[0 70*0.8],'r-', 'linewidth',2)
plot([70 400],[70*0.8 320],'r-', 'linewidth',2)
plot([180 180],[0 70],'k-', 'linewidth',2)
plot([180 400],[70 70],'k-', 'linewidth',2)
plot([240 240],[70 180],'k-', 'linewidth',2)
plot([240 400],[180 180],'k-', 'linewidth',2)
plot([130 180],[0 70],'k-', 'linewidth',2)                  % Lower ...
    B-C boundary slope OK
text(30,20,'A','fontsize',14,'fontweight', 'bold');
text(30,150,'D','fontsize',14,'fontweight', 'bold');
text(30,380,'E','fontsize',14,'fontweight', 'bold');
text(150,380,'C','fontsize',14,'fontweight', 'bold');
text(160,20,'C','fontsize',14,'fontweight', 'bold');
text(380,20,'E','fontsize',14,'fontweight', 'bold');
text(380,120,'D','fontsize',14,'fontweight', 'bold');
text(380,260,'B','fontsize',14,'fontweight', 'bold');
text(280,380,'B','fontsize',14,'fontweight', 'bold');
set(gcf, 'color', 'white');                 % sets the color to white
total = zeros(5,1);                         % Initializes output
percentage = zeros(5,1);                    % Initializes output
for i=1:n,
    if (yp(i) ≤ 70 && y(i) ≤ 70) || (yp(i) ≤ 1.2*y(i) && yp(i) ≥ ...
       0.8*y(i))
        total(1) = total(1) + 1;            % Zone A
    else
        if ( (y(i) ≥ 180) && (yp(i) ≤ 70) ) || ( (y(i) ≤ 70) && ...
           yp(i) ≥ 180 )
            total(5) = total(5) + 1;        % Zone E
        else
            if ((y(i) ≥ 70 && y(i) ≤ 290) && (yp(i) > y(i) + 110) ) ...
               || ((y(i) > 130 && y(i) ≤ 180)&& (yp(i) < (7/5)*y(i) ...
               - 182))
```

```
77                  total(3) = total(3) + 1;     % Zone C
78              else
79                  if ((y(i) > 240) && ((yp(i) ≥ 70) && (yp(i) < 180))) ...
                        || (y(i) < 70/1.2 && (yp(i) ≤ 180) && (yp(i) > ...
                        70)) || ((y(i) ≥ 70/1.2 && y(i) < 70) && (yp(i) ...
                        > 1.2*y(i)))
80                      total(4) = total(4) + 1;% Zone D
81                  else
82                      total(2) = total(2) + 1;% Zone B
83                  end                          % End of 4th if
84              end                              % End of 3rd if
85          end                                  % End of 2nd if
86      end                                      % End of 1st if
87  end                                          % End of for loop
88  percentage = (total./n)*100;
89  % ...
```

```
1  function [] = libsvm_format (Y, spectral_matrix, out_filename)
2  % Convert data into format compatible with LIBSVM and write to file
3  % libsvm_format (Y, spectral_matrix, out_filename)
4  % Output File Format:
5  % Y index_1: x_1 index_2: x_2 ...   \n
6
7  [num_datapoints, num_pixels] = size(spectral_matrix);
8  fid = fopen(out_filename, 'w');
9  for a = 1:num_datapoints
10    fprintf(fid, '%6.2f ', Y(a));
11    for b = 1:num_pixels
12       fprintf(fid, '%u:%-8.2f ', b, full(spectral_matrix(a,b)));
13    end
14    fprintf(fid, '\n');
15 end
16 fclose(fid);
```

```
1  % dcc_pls_calib
2  % CALIBRATION step using BG and spectroscopic data
3  %
4  % Inputs:
5  %   Raman_calib : Calibration Raman spectra (rows, pixels)
6  %   minpix, maxpix : pixel range
7  %   t : time (min)
8  %   c_BG_calib : Calibration Blood glucose vector
9  %   step : time step for iteration (min)
10 %
11 % Outputs:
12 %   alpha_opt : optimized time constant (min)
13 %   LV_model_opt : optimized number of PLS loading vectors for DCC
14 %   b_model_opt : optimized PLS regression b vector for DCC
15 %   c_ISF_calib_trans_opt : ISF glucose converted from blood glucose
16
17 function [alpha_opt, LV_model_opt, b_model_opt, ...
       c_ISF_calib_trans_opt] = dcc_pls_calib(Raman_calib, ...
18  minpix, maxpix, t, c_BG_calib, step)
19 rmsecv_default = 10^5;
20 rmsecv_min = rmsecv_default;
21 alpha_opt = 0; % assign initial value
22 LV_no_model_opt = 0; % assign initial value
23 LV_model_opt = 0; % assign initial value
24 b_no_model_opt = [];
25 b_model_opt = [];
26 LV_max = 10; % maximum number of loading vectors over which to iterate
27 count_alpha = 0;
28 calib_size = size(c_BG_calib, 1);
29 c_ISF_calib_trans = c_BG_calib(1)*ones(calib_size,1);   % ...
       initializing the c_ISF_calib_trans variable
30 c_ISF_calib_trans_opt = c_ISF_calib_trans; % initializing the ...
       c_ISF_calib_trans_opt variable
31 c_BG_cv_trans = c_BG_calib(1)*ones(calib_size,1);
32
33 for alpha = 1:step:10
```

```
34      count_alpha = count_alpha+1;
35      % Performing the BG to ISF transform so that the regression ...
           model is fully based on ISF glucose
36      for i = 1:1:calib_size-1
37          c_BG_avg = 1/2*(c_BG_calib(i) + c_BG_calib(i+1));
38  % assumption is that the value of the BG at the middle of the time ...
       interval is the average of the values at the end-points
39          c_ISF_calib_trans(i+1) = ...
                c_ISF_calib_trans(i)*exp(-(1/alpha)*(t(i+1)-t(i))) + ...
                1/(6*alpha)*(t(i+1)-t(i))*(c_BG_calib(i)*exp(-1/alpha*(t(i+1)-t(i))) ...
                + c_BG_calib(i+1) + ...
                4*c_BG_avg*exp(-1/(2*alpha)*(t(i+1)-t(i))));
40      end
41      % Performing PLS leave-one-out cross-validation on ...
           (c_ISF_calib_trans, Raman_calib) to obtain the RMSECV ...
           corresponding to different sets of (alpha, LV)
42      R_raw=candp(Raman_calib,c_ISF_calib_trans,LV_max,minpix,maxpix,1,[ ...
           ],[1:size(c_ISF_calib_trans,1)]);
43
44      for i = 1:LV_max+1;
45          c_BG_cv_trans(2:end) = R_raw(2:end,i) + ...
                alpha*diff(R_raw(:,i))./diff(t);  % convert R_raw_ISF ...
                back to BG before comparing rmsecv
46          rmsecv_temp(i) = rmsep(c_BG_cv_trans, c_BG_calib); %  ...
                convert R_raw_ISF back to BG before comparing rmsecv
47          rmsecv_plot(count_alpha, i) = rmsecv_temp(i);
48      end
49      [rmsecv_dyn, LV] = min(rmsecv_temp);
50      if (LV<3)
51          LV=3;
52      end
53      % Determing the optimal alpha and LV
54      if(rmsecv_dyn-rmsecv_min<0)
55          rmsecv_min = rmsecv_dyn ;
56          alpha_opt = alpha;
57          LV_model_opt = LV;
```

```
58          c_ISF_calib_trans_opt = c_ISF_calib_trans;
59      end
60  end
61
62  plscalib(Raman_calib(:,minpix:maxpix), c_ISF_calib_trans_opt, LV_max);
63  b_model_opt = bvector(LV_model_opt-1);
```

```
1  % dcc_pls_predict
2  % PREDICTION step using b-vectors and prediction Raman spectra
3  %
4  % Inputs:
5  %    Raman_pred : Prediction Raman spectra (rows, pixels)
6  %    b_model_opt : optimized PLS regression b vector for DCC
7  %    alpha_opt : optimized time constant (min)
8  %    c_ISF_calib_trans_opt : ISF glucose converted from blood glucose
9  %    dt : data time step (e.g. 2.485 min)
10 % Outputs:
11 %    c_BG_model_pred: blood glucose concentration predicted with DCC
12
13 function [c_BG_model_pred] = dcc_pls_predict(Raman_pred, minpix, ...
       maxpix, ...
14 Raman_calib, b_model_opt, alpha_opt, c_ISF_calib_trans_opt, t)
15
16 % DYNAMIC MODEL PREDICTION: INPUTS OF b_model_opt AND PREDICTION ...
       RAMAN SPECTRA
17 c_ISF_model_pred = ...
       (Raman_pred(:,minpix:maxpix)-ones(size(Raman_pred,1),1)* ...
18 mean(Raman_calib(:,minpix:maxpix)))*b_model_opt+mean(c_ISF_calib_trans_opt);
19 % c_ISF_model_pred = ...
       (Raman_pred(:,minpix:maxpix)-ones(size(Raman_pred,1),1)* ...
20 mean(Raman_pred(:,minpix:maxpix)))*b_model_opt+mean(c_ISF_calib_trans_opt);
21 c_BG_model_pred_temp = c_ISF_model_pred(2:end) + ...
       alpha_opt*diff(c_ISF_model_pred)./diff(t);...
22   % Predicting c_BG based on alpha_opt from calibration
23 c_BG_model_pred = c_BG_model_pred_temp;
```

Bibliography

[1] Diabetes atlas, 4th edition. Technical report, International Diabetes Federation, 2009.

[2] S. E. Kahn, R. L. Hull, and K. M. Utzschneider. Mechanisms linking obesity to insulin resistance and type 2 diabetes. *Nature*, 444:840–846, 2006.

[3] J. G. Hamilton. Needle phobia: a neglected diagnosis. *The Journal of Family Practice*, 41:169–175, 1995.

[4] A. Zambanini and M. D. Feher. Needle phobia in type 1 diabetes mellitus. *Diabetic Medicine*, 14(4):321–323, 1997.

[5] A. Sieg, R. H. Guy, and M. B. Delgado-Charro1. Noninvasive glucose monitoring by reverse iontophoresis in vivo: Application of the internal standard concept. *Clinical Chemistry*, 50:1383–1390, 2004.

[6] Valerie V. Tuchin, editor. *Handbook of optical sensing of glucose in biological fluids and tissues.* CRC Press, 2009.

[7] R. O Esenaliev, K. V. Larin, I. V. Larina, and M. Motamedi. Noninvasive monitoring of glucose concentration with optical coherence tomography. *Optics Letters*, 26(13):992–994, 2001.

[8] R. C. Weast, editor. *CRC Handbook of Chemistry and Physics.* CRC Press, Cleveland, Ohio, 70 edition, 1989.

[9] F. A. Duck. *Physical Properties of Tissue.* Academic Press, London, 1990.

[10] M. Kohl and M. Cope. Influence of glucose concentration on light scattering in tissue-simulating phantoms. *Optics Letters*, 19:2170, 1994.

[11] S. Fantini M. A. Frances-chini J. S. Maier, S. A. Walker and 2062 (1994). E. Gratton, Opt. Lett. 19. Possible correlation between blood glucose concentration and the reduced scattering coefficient of tissues in the near infrared. *Optics Letters*, 19:2062, 1994.

[12] T. W. King, G. L. Cote, R. J. McNichols, and M. J. Goetz, Jr. Multispectral polarimetric glucose detection using a single Pockels cell. *Optical Engineering*, 33:2746–2753, 1994.

[13] K. M. Quan, G. B. Christison, H. A. MacKenzie, and P. Hodgson. Glucose determination by a pulsed photoacoustic technique: an experimental study using a gelatin-based tissue phantom. *Physics in Medicine and Biology*, 38:1911–1922, 1993.

[14] A. Shusterman I. Raz Ram Weiss, Y. Yegorchikov. Noninvasive continuous glucose monitoring using photoacoustic technologyresults from the first 62 subjects. *Diabetes Technology and Therapeutics*, 9(1):68–74, 2007.

[15] Ryou Shinohara Naoki Wadamori and Yasutoshi Ishihara. Photoacoustic depth profiling of a skin model for non-invasive glucose measurement. *30th Annual International IEEE EMBS Conference*, pages 5644–5647, 2008.

[16] N. D. Evans, L. Gnudi, O. J. Rolinski, D. J. S. Birch, and J. C. Pickup. Noninvasive glucose monitoring by NAD(P)H autouorescence spectroscopy in broblasts and adipocytes: a model for skin glucose sensing. *Diabetes Technology and Therapeutics*, 5:807–816, 2003.

[17] H. M. Heise and R. Marbach. Human oral mucosa studies with varying blood glucose concentration by non-invasive ATR-FT-IR-spectroscopy. *Cellular and Molecular Biology*, 44(6):899–912, 1998.

[18] J. J. Burmeister, M. A. Arnold, and G. W. Small. Noninvasive blood glucose measurements by near-infrared transmission spectroscopy across human tongues. *Diabetes Technology and Therapeutics*, 2:5–16, 2000.

[19] R. Marbach, T. Koschinsky, F. A. Gries, and H. M. Heise. Noninvasive blood glucose assay by near-infrared diffuse reflectance spectroscopy of the human inner lip. *Applied Spectroscopy*, 47:875–881, 1993.

[20] K. Maruo, T. Oota, M. Tsurugi, T. Nakagawa, H Arimoto, M. Tamura, Y. OzakiI, and Y. Yamada. New methodology to obtain a calibration model for noninvasive near-infrared blood glucose monitoring. *Applied Spectroscopy*, 60(4):441–449, 2006.

[21] K. Maruo, M. Tsurugi, M. Tamura, and Y. Ozaki. In vivo noninvasive measurement of blood glucose by near-infrared diffuse-reflectance spectroscopy. *Applied Spectroscopy*, 57:1236–1244, 2003.

[22] M. R. Robinson, R. P. Eaton, D. M. Haaland, G. W. Koepp, E. V. Thomas, B. R. Stallard, and P. L. Robinson. Noninvasive glucose monitoring in diabetic-patients - a preliminary evaluation. *Clinical Chemistry*, 38(9):1618–1622, 1992.

[23] A. Samann, C. Fischbacher, K.U. Jagemann, K. Danzer, J. Schuler, L. Papenkordt, and U.A. Muller. Non-invasive blood glucose monitoring by means of near infrared spectroscopy: investigation of long-term accuracy and stability. *Experimental and Clinical Endocrinology & Diabetes*, 108(6):406–413, 2000.

[24] S. Söderholm, Y. H. Roos, N. Meinander, and M. Hotokka. Raman spectra of fructose and glucose in the amorphous and crystalline states. *Journal of Raman Spectroscopy*, 30(11):1009–1018, 1999.

[25] R. L. McCreery. *Raman spectroscopy for chemical analysis*, volume 157 of *Chemical Analysis*. Wiley-Interscience, 2000.

[26] O. Lyandres, J. M. Yuen, N. C. Shah, R. P. VanDuyne, J. T. Walsh, Jr., and M. R. Glucksberg. Progress toward an in vivo surface-enhanced Raman spectroscopy glucose sensor. *Diabetes Technology and Therapeutics*, 10(4):257–265, 2008.

[27] A. J. Berger, T. W. Koo, I. Itzkan, G. Horowitz, and M. S. Feld. Multicomponent blood analysis by near-infrared raman spectroscopy. *Applied Optics*, 38(13):2916–2926, 1999.

[28] A. M. K. Enejder, T. W. Koo, J. Oh, M. Hunter, S. Sasic, M. S. Feld, and G. L. Horowitz. Blood analysis by raman spectroscopy. *Optics Letters*, 27(22):2004–2006, 2002.

[29] A. J. Berger, T. W. Koo, I. Itzkan, and M. S. Feld. An enhanced algorithm for linear multivariate calibration. *Analytical Chemistry*, 70(3):623–627, 1998.

[30] W. C. Shih, K.L. Bechtel, and M. S. Feld. Constrained regularization: A hybrid method for multivariate calibration. *Analytical Chemistry*, 79(1):234–239, 2007.

[31] A. N. Tikhonov and V. Y. Arsenin. *Solutions of ill-posed problems; Winston:, 1977*. Winston, Washington DC, 1977.

[32] J. Chaiken, W. Finney, P. E. Knudson, R. S. Weinstock, M. Khan, R. J. Bussjager, D. Hagrman, P. Hagrman, Y. W. Zhao, C. M. Peterson, and K. Peterson. Effect of hemoglobin concentration variation on the accuracy and precision of glucose analysis using tissue modulated, noninvasive, in vivo raman spectroscopy of human blood: a small clinical study. *Journal of Biomedical Optics*, 10(3):031111, 2005.

[33] W. C. Shih, K. L. Bechtel, and M. S. Feld. Intrinsic Raman spectroscopy for quantitative biological spectroscopy part i: theory and simulations. *Optics Express*, 16(17):12726–36, 2008.

[34] K. L. Bechtel, W. C. Shih, and M. S. Feld. Intrinsic Raman spectroscopy for quantitative biological spectroscopy part ii: experimental applications. *Optics Express*, 16(17):12737–45, 2008.

[35] I. Barman, G. P. Singh, R. R. Dasari, and M. S. Feld. Turbidity-corrected Raman spectroscopy for blood analyte detection. *Analytical Chemistry*, 81(11):4233–4240, 2009.

[36] I. Barman, C. R. Kong, G. P. Singh, and R. R. Dasari. Effect of photobleaching on calibration model development in biological Raman spectroscopy. *Journal of Biomedical Optics*, 16(1):011004, 2011.

[37] I. Osticioli, A. Zoppi, and E. M. Castellucci. Shift-excitation raman difference spectroscopy difference deconvolution method for the luminescence background rejection from raman spectra of solid samples. *Applied Spectroscopy*, 61:839–844, 2007.

[38] C. A. Lieber and A. Mahadevan-Jansen. Automated method for subtraction of fluorescence from biological Raman spectra. *Applied Spectroscopy*, 57(11):1363–1367, 2003.

[39] I. Barman, C. R. Kong, N. C. Dingari, R. R. Dasari, and M. S. Feld. Development of robust calibration models using support vector machines for spectroscopic monitoring of blood glucose. *Analytical Chemistry*, 82(23):9719–9726, 2010.

[40] J. A. McGrath, R. A. Eady, and F. M. Pope. *Rook's Textbook of Dermatology.* Blackwell Publishing, 2004.

[41] J. N. Roe and B. R. Smoller. Bloodless glucose measurements. *Critical Reviews in Therapeutic Drug Carrier Systems*, 15(3):199–241, 1998.

[42] E Cengiz and W. V. Tamborlane. A tale of two compartments: interstitial versus blood glucose monitoring. *Diabetes Technology and Therapeutics*, 11(S1):S–11–16, 2009.

[43] J. Bolinder, U. Ungerstedt, and P. Arner. Microdialysis measurement of the absolute glucose concentration in subcutaneous adipose tissue allowing glucose monitoring in diabetic patients. *Diabetologia*, 35:1177–1180, 1992.

[44] G. Reach and G. S. Wilson. Can continuous glucose monitoring be used for the treatment of diabetes? *Analytical Chemistry*, 64(6):381A–386A, 1992.

[45] P. Lonnroth, P. A. Jansson, and U. Smith. A microdialysis method allowing characterization of intercellular water space in humans. *American Journal of Physiology*, 253:E228–E231, 1987.

[46] R. A. DeFronzo, J. D. Tobin, and R. Andres. Glucose clamp technique: a method for quantifying insulin secretion and resistance. *American Journal of Physiology Gastrointestinal and Liver Physiology*, 237(3):G214–G233, 1979.

[47] D. W. Schmidtke, A. C. Freeland, A. Heller, and R. T. Bonnecaze. Measurement and modeling of the transient difference between blood and subcutaneous glucose concentrations in the rat after injection of insulin. *Proceedings of National Academy of Sciences*, 95:294–299, 1998.

[48] A. C. Freeland and R. T. Bonnecaze. Inference of blood glucose concentrations from subcutaneous glucose concentrations: applications to glucose biosensors. *Annals of Biomedical Engineering*, 27:525537, 1999.

[49] I. Barman, C. R. Kong, G. P. Singh, R. R. Dasari, and M. S. Feld. Accurate spectroscopic calibration for noninvasive glucose monitoring by modeling the physiological glucose dynamics. *Analytical Chemistry*, 82(14):6104–6114, 2010.

[50] R. G. Brereton. *Applied Chemometrics for Scientists.* John Wiley & Sons Ltd., Chichester, West Sussex, England, 2007.

[51] K. Zierler. Whole body glucose metabolism. *American Journal of Physiology*, 276:E409E426, 1999.

[52] G. M. Steil, K. Rebrin, F. Hariri, S. Jinagonda, S. Tadros, C. Darwin, and M. F. Saad. Interstitial fluid glucose dynamics during insulin-induced hypoglycaemia. *Diabetologia*, 48:18331840, 2005.

[53] K. Rebrin, G. M. Steil, W. P. van Antwerp, and J. J. Mastrototaro. Subcutaneous glucose predicts plasma glucose independent of insulin: implications for continuous monitoring. *American Journal of Physiology*, 277:E561E571, 1999.

[54] M. S. Boyne, D. M. Silver, J. Kaplan, and C. D. Saudek. Timing of changes in interstitial and venous blood glucose measured with a continuous subcutaneous glucose sensor. *Diabetes*, 52(11):2790–2794, 2003.

[55] A. Lorber and B. Kowalski. Estimation of prediction error for multivariate calibration. *Journal of Chemometrics*, 2:93–109, 1988.

[56] O. R. Šćepanović, K. L. Bechtel, A. S. Haka, W. C. Shih, T. W. Koo, A. J. Berger, and M. S. Feld. Determination of uncertainty in parameters extracted from single spectroscopic measurements. *Journal of Biomedical Optics*, 12(6):064012, 2007.

[57] A. M. K. Enejder, T. G. Scecina, J. Oh, M. Hunter, W. C. Shih, S. Sasic, G. Horowitz, and M. S. Feld. Raman spectroscopy for non-invasive glucose measurements. *Journal of Biomedical Optics*, 10(3):031114, 2005.

[58] U. Thissen, B. Ustun, W. J. Melssen, and L. M. C. Buydens. Multivariate calibration with least-squares support vector machines. *Analytical Chemistry*, 76:3099–3105, 2004.

[59] B. Aussedat, V. Thomè-Duret, G. Reach, F. Lemmonier, J. C. Klein, Y. Hu, and G. S. Wilson. A user-friendly method for calibrating a subcutaneous glucose sensor-based hypoglycaemic alarm. *Biosensors & Bioelectronics*, 12:1061–1071, 1997.

[60] E. Sternberg, C. Meyerhoff, F. J. Mennel, H. Mayer, E. Bischof, and E. E. Pfeiffer. Does fall in tissue glucose precede fall in blood glucose? *Diabetologia*, 39:609–612, 1996.

[61] V. Thomè-Duret, G. Reach, M. N. Gangnerau, F. Lemonnier, J. C. Klein, Y. Zhang, Y. Hu, and G. S. Wilson. Use of a subcutaneous glucose sensor to detect decreases in glucose concentration prior to observation in blood. *Analytical Chemistry*, 68:38223826, 1996.

[62] J. E. B. Reusch. Diabetes, microvascular complications, and cardiovascular complications: what is it about glucose? *Journal of Clinical Investigation*, 112(7):986–988, 2003.

[63] L. V. Wang and H.-I. Wu. *Biomedical Optics: Principles and Imaging.* Wiley Interscience, New Jersey, 2007.

[64] S. Stolik, J. A. Delgado, A. Perez, and L. Anasagasti. Measurement of the penetration depths of red and near infrared light in human ex vivo tissues. *Journal of Photochemistry and Photobiology B: Biology*, 57:90–93, 2000.

[65] M. J. C. van Gemert, S. L. Jacques, H. J. C. M. Sterenborg, and W. M. Star. Skin optics. *IEEE Transactions on Biomedical Engineering*, 36(12):1146–1154, 1989.

[66] P. Matousek, I. P. Clark, E. R. Draper, M. D. Morris, A. E. Goodship, N. Everall, M. Towrie, W. F. Finney, and A. W. Parker. Subsurface probing in diffusely scattering media using spatially offset raman spectroscopy. *Applied Spectroscopy*, 59(4):393–400, 2005.

[67] Berger A. J. Maher, J. R. Determination of ideal offset for spatially offset Raman spectroscopy. *Applied Spectroscopy*, 64(1):61–65, 2010.

[68] P. Matousek and N. Stone. Prospects for the diagnosis of breast cancer by noninvasive probing of calcifications using transmission Raman spectroscopy. *Journal of Biomedical Optics*, 12:024008, 2007.

[69] N. Stone and P. Matousek. Advanced transmission Raman spectroscopy: a promising tool for breast disease diagnosis. *Cancer Research*, 68(11):4424–4430, 2008.

[70] J. J. Burmeister and M. A. Arnold. Evaluation of measurement sites for non-invasive blood glucose sensing with near-infrared transmission spectroscopy. *Clinical Chemistry*, 45(9):1621–1627, 1999.

[71] L. Wang, S. L. Jacques, and L. Zheng. MCML-Monte Carlo modeling of light transport in multi-layered tissues. *Computer Methods and Programs in Biomedicine*, 47:131–146, 1995.

[72] W. C. Shih. *Quantitative biological Raman spectroscopy for non-invasive blood analysis.* PhD thesis, Massachusetts Institute of Technology, Cambridge, MA, 2007.

[73] P. Matousek. Raman signal enhancement in deep spectroscopy of turbid media. *Applied Spectroscopy*, 61(8):845–854, 2007.

[74] A. Mahadevan-Jansen, M. F. Mitchell, N. Ramanujam, U. Utzinger, and R. Richards-Kortum. Development of a fiber optic probe to measure NIR Raman spectra of cervical tissue in vivo. *Photochemistry and Photobiology*, 68(3):427–431, 1998.

[75] J. T. Motz, M. Hunter, L. H. Galindo, J. A. Gardecki, J. R. Kramer, R. R. Dasari, and M. S. Feld. Optical fiber probe for biomedical Raman spectroscopy. *Applied Optics*, 43(3):542–554, 2004.

[76] U. Utzinger and R. R. Richards-Kortum. Fiber optic probes for biomedical optical spectroscopy. *Journal of Biomedical Optics*, 8(1):121–147, 2003.

[77] K. Tanaka, M. T. T. Pacheco, J. F. Brennan III, I. Itzkan, A. J. Berger, R. R. Dasari, and M. S. Feld. Compound parabolic concentrator probe for efficient light collection in spectroscopy of biological tissue. *Applied Optics*, 35(4):758–763, 1996.

[78] R. Winston. Nonimaging Optics. *Solar Today*, 6:2629, 1992.

[79] T. J. Brukilacchio. LED illuminator with retro reflector, March U.S. Patent 0053184A1, 2007.

[80] W. T. Welford and R. Winston. *High Collection Nonimaging Optics.* Academic Press, New York, NY, 1989.

[81] R. Winston, J. C. Minano, and P. Benitez. *Nonimaging Optics.* Elsevier Academic Press, Burlington, MA, 2005.

[82] B. Yang, M. D. Morris, and H. Owen. Holographic notch filter for low-wavenumber Stokes and anti-Stokes Raman spectroscopy. *Applied Spectroscopy*, 45(9):1533–36, 1991.

[83] J. M. Tedesco, H. Owen, D. M. Pallister, and M. D. Morris. Principles and spectroscopic applications of volume holographic optics. *Analytical Chemistry*, 65(9):441A–449A, 1993.

[84] Narcus. Bright electroless plating process producing two-layer nickel coatings on dielectric subtrates, July U.S. Patent 4160049, 1979.

[85] O. R. Šćepanović, Z. Volynskaya, C. R. Kong, L. Galindo, R. R. Dasari, and M. S. Feld. A multimodal spectroscopy system for real-time disease diagnosis. *Review of Scientific Instruments*, 80:043103, 2009.

[86] M. L. Myrick and S. M. Angel. Elimination of background in fiber-optic Raman measurements. *Applied Spectroscopy*, 44(4):565–570, 1990.

[87] Tae-Woong Koo. *Measurement of blood analytes in turbid biological tissue using near-infrared Raman spectroscopy.* PhD thesis, Massachusetts Institute of Technology, 2001.

[88] A. Haka, K. E. Shafer-Peltier, M. Fitzmaurice, J. Crowe, R. R. Dasari, and M. S. Feld. Diagnosing breast cancer by using Raman spectroscopy. *Proceedings of the National Academy of Sciences of the United States of America*, 102(35):12371–12376, 2005.

[89] N. Stone, M. Consuelo, H. Prieto, P. Crow, J. Uff, and A. W. Ritchie. The use of Raman spectroscopy to provide an estimation of the gross biochemistry associated with urological pathologies. *Analytical and Bioanalytical Chemistry*, 387(5):1657–1668, 2006.

[90] S. K. Teh, W. Zheng, K. Y. Ho, M. Teh, K. G. Yeoh, and Z. Huang. Diagnostic potential of near-infrared Raman spectroscopy in the stomach: differentiating dysplasia from normal tissue. *British Journal of Cancer*, 98:457–465, 2008.

[91] J. T. Motz, M. Fitzmaurice, A. Miller, S. J. Gandhi, A. S. Haka, L. H. Galindo, R. R. Dasari, J. R. Kramer, and M. S. Feld. In vivo Raman spectral pathology of human atherosclerosis and vulnerable plaque. *Journal of Biomedical Optics*, 11(2):021003, 2006.

[92] O. R. Šćepanović, M. Fitzmaurice, J. A. Gardecki, G. O. Angheloiu, S. Awasthi, J. T. Motz, J. R. Kramer, R. R. Dasari, and M. S. Feld. Detection of morphological markers of vulnerable atherosclerotic plaque using multimodal spectroscopy. *Journal of Biomedical Optics*, 11(2):021007, 2006.

[93] H. P. Buschman, J. T. Motz, G. Deinum, T. J. Romer, M. Fitzmaurice, J. R. Kramer, A. van der Laarse, A. V. Bruschke, and M. S. Feld. Diagnosis of human coronary atherosclerosis by morphology-based Raman spectroscopy. *Cardiovascular Pathology*, 10:59–68, 2001.

[94] A. J. Berger, I. Itzkan, and M. S. Feld. Feasibility of measuring blood glucose concentration by near-infrared Raman spectroscopy. *Spectrochimica Acta Part A-Molecular and Biomolecular Spectroscopy*, 53(2):287–292, 1997.

[95] H. Wold. *Multivariate Analysis*, new York Estimation of principal components and related models by iterative least squares, pages 391–420. Academic Press, 1966.

[96] W. P. Carey, K. R. Beebe, E. Sanchez, P. Geladi, and B. Kowalski. Chemometric analysis of multisensor arrays. *Sensors and Actuators*, 9(3):223–234, 1986.

[97] H. Drucker, C. J. C. Burges, L. Kaufman, A. Smola, and V. Vapnik. Support vector regression machines. In *Advances in Neural Information Processing Systems 9*, pages 155–161. MIT Press, 1997.

[98] Jarquin-Valdivia A. A. Bridges, N. Use of the Trendelenburg position as the resuscitation position: To T or not to T? *American Journal of Critical Care*, 14:364–368, 2005.

[99] J. T. Y. Lin, D. K. Ziegler, Lai C. W., and W. Bayer. Convulsive syncope in blood donors. *Annals of Neurology*, 11:525–528, 1982.

[100] V. Vapnik, S. Golowich, and A. Smola. *Advances in Neural Information Processing Systems 9*, chapter Support vector method for function approximation, regression estimation, and signal processing, pages 281–287. MIT Press, 1997.

[101] Chih-Chung Chang and Chih-Jen Lin. *LIBSVM: a library for support vector machines*, 2001. Software available at `http://www.csie.ntu.edu.tw/~cjlin/libsvm`.

[102] W. L. Clarke, D. Cox, L. A. Gonder-Frederick, W. Carter, and S. L. Pohl. Evaluating clinical accuracy of systems for self-monitoring of blood glucose. *Diabetes Care*, 10:622–628, 1987.

[103] Susan Heavey. Reuters: "FDA eyes improvements for diabetics' glucose devices", March 2010.

[104] J. Parkes, S. L. Slatin, S. Pardo, and B. H. Ginsberg. A new consensus error grid to evaluate the clinical significance of inaccuracies in the measurement of blood glucose. *Diabetes Care*, 23(8):1143–1148, 2000.

[105] D. A. Gough and E. L. Botvinick. Reservations on the use of error grid analysis for the validation of blood glucose assays. *Diabetes Care*, 20:1034–1036, 1997.

[106] D. J. Cox, L. Gonder-Frederick, B. P. Kovachev, D. M. Julian, and W. L. Clarke. Understanding error grid analysis. *Diabetes Care*, 20:911–912, 1997.

[107] Hans-Martin Schmidt and Ulrich Lanz. *Surgical anatomy of the hand.* Georg Thieme Verlag, 2004.

[108] S. N. Thennadil, J. L Rennert, B. J. Wenzel, K. H. Hazen, T. L. Ruchti, and M. B. Block. Comparison of glucose concentration in interstitial fluid, and capillary and venous blood during rapid changes in blood glucose levels. *Diabetes Technology and Therapeutics*, 3(3):357–65, 2001.